ornl

OAK
RIDGE
NATIONAL
LABORATORY

UNION
CARBIDE

NUREG/CR-2141/V1
ORNL/TM-7822

RECEIVED
JUL 21 1981
U.S. NUCLEAR REGULATORY COMMISSION

# Heavy-Section Steel Technology Program Quarterly Progress Report for January–March 1981

G. D. Whitman R. H. Bryan

Prepared for the U.S. Nuclear Regulatory Commission
Office of Nuclear Regulatory Research
Under Interagency Agreements DOE 40-551-75 and 40-552-75

OPERATED BY
UNION CARBIDE CORPORATION
FOR THE UNITED STATES
DEPARTMENT OF ENERGY

Printed in the United States of America. Available from
National Technical Information Service
U.S. Department of Commerce
5285 Port Royal Road, Springfield, Virginia 22161

Available from
GPO Sales Program
Division of Technical Information and Document Control
U.S. Nuclear Regulatory Commission
Washington, D.C. 20555

NUREG/CR-2141/V1
ORNL/TM-7822
Dist. Category RF

Contract No. W-7405-eng-26

Engineering Technology Division

# HEAVY-SECTION STEEL TECHNOLOGY PROGRAM QUARTERLY PROGRESS REPORT FOR JANUARY—MARCH 1981

G. D. Whitman   R. H. Bryan

Manuscript Completed — June 1, 1981
Date Published — June 1981

**NOTICE** This document contains information of a preliminary nature. It is subject to revision or correction and therefore does not represent a final report.

Prepared for the
U.S. Nuclear Regulatory Commission
Office of Nuclear Regulatory Research
Under Interagency Agreements DOE 40-551-75 and 40-552-75

NRC FIN No. B0119

Prepared by the
OAK RIDGE NATIONAL LABORATORY
Oak Ridge, Tennessee 37830
operated by
UNION CARBIDE CORPORATION
for the
DEPARTMENT OF ENERGY

CONTENTS

# PREFACE

The Heavy-Section Steel Technology (HSST) Program, which is sponsored by the Nuclear Regulatory Commission, is an engineering research activity devoted to extending and developing the technology for assessing the margin of safety against fracture of the thick-walled steel pressure vessels used in light-water-cooled nuclear power reactors. The program is being carried out in close cooperation with the nuclear power industry. This report covers HSST work performed in January through March 1981. The work performed by Oak Ridge National Laboratory (ORNL) and by subcontractors is managed by the Engineering Technology Division. Major tasks at ORNL are carried out by the Engineering Technology Division and the Metals and Ceramics Division. Prior progress reports on this program are ORNL-4176, ORNL-4315, ORNL-4377, ORNL-4463, ORNL-4512, ORNL-4590, ORNL-4653, ORNL-4681, ORNL-4764, ORNL-4816, ORNL-4855, ORNL-4918, ORNL-4971, ORNL/TM-4655 (Vol. II), ORNL/TM-4729 (Vol. II), ORNL/TM-4805 (Vol. II), ORNL/TM-4914 (Vol. II), ORNL/TM-5021 (Vol. II), ORNL/TM-5170, ORNL/NUREG/TM-3, ORNL/NUREG/TM-28, ORNL/NUREG/TM-49, ORNL/NUREG/TM-64, ORNL/NUREG/TM-94, ORNL/NUREG/TM-120, ORNL/NUREG/TM-147, ORNL/NUREG/TM-166, ORNL/NUREG/TM-194, ORNL/NUREG/TM-209, ORNL/NUREG/TM-239, NUREG/CR-0476 (ORNL/NUREG/TM-275), NUREG/CR-0656 (ORNL/NUREG/TM-298), NUREG/CR-0818 (ORNL/NUREG/TM-324), NUREG/CR-0980 (ORNL/NUREG/TM-347), and NUREG/CR-1197 (ORNL/NUREG/TM-370), NUREG/CR-1305 (ORNL/NUREG/TM-380), NUREG/CR-1477 (ORNL/NUREG/TM-393), NUREG/CR-1627 (ORNL/NUREG/TM-401), NUREG/CR-1806 (ORNL/NUREG/TM-419), and NUREG/CR-1941 (ORNL/NUREG/TM-437).

# SUMMARY

## 1. PROGRAM ADMINISTRATION AND PROCUREMENT

The Heavy-Section Steel Technology (HSST) Program is an engineering research activity conducted by the Oak Ridge National Laboratory (ORNL) for the Nuclear Regulatory Commission (NRC) in coordination with other research sponsored by the federal government and private organizations. The program comprises studies related to all areas of the technology of materials fabricated into thick-section primary-coolant containment systems of light-water-cooled nuclear power reactors. The principal area of investigation is the behavior and structural integrity of steel pressure vessels containing crack-like flaws. Current work is organized into the following tasks: (1) program administration and procurement, (2) fracture mechanics analyses and investigations, (3) investigations of irradiated materials, (4) thermal shock investigations, and (5) pressure vessel investigations.

The work performed under the existing research and development subcontracts is included in this report.

Nine program briefings, reviews, or presentations were made during the quarter.

## 2. FRACTURE MECHANICS ANALYSES AND INVESTIGATIONS

Two finite-element computer programs have been written for elastic and elastic-plastic fracture mechanics analysis. The ORJINT-2D is a two-dimensional code for calculating the J-integral, which can be converted to $K_I$ for elastic problems. The ORVIRT-3D is a three-dimensional code using virtual crack extension for calculating strain energy release rates and related fracture parameters.

Battelle Columbus Laboratories (BCL) is providing analytical and experimental support to the HSST program. Dynamic fracture mechanics analyses were made of the crack jumps observed in the thermal shock experiment TSE-5A. The calculated crack jumps were sensitive to the choice of toughness values. Replacing mean values by lower-bound values of toughness produced good agreement between analysis and experiment.

Also, BCL made an analysis of the relative merits of spring and pneumatic loading for promoting crack instability. Such evaluations are being made to identify testing methods for measuring lower-bound toughness. Fractographic studies were also made to locate weak spots believed to trigger cleavage fracture.

At the University of Maryland, studies of ductile-brittle transition in fracture are continuing in cooperation with other laboratories. Double-width Charpy V-notch specimens were tested, indicating the existence of an effect of constraint in cleavage formation. Topological measurements of fracture surfaces of two materials agreed with fracture toughness estimates and provided useful information on fracture mechanisms.

A dynamic analysis of thermal shock experiment TSE-5 was completed with the SAMCR code. An extreme sensitivity of the results to the arrest toughness ($K_{Ia}$) vs temperature relationship was noted; however, the lower-bound $K_{Ia}$ produced an accurate estimate of the crack jump.

## 3. INVESTIGATIONS OF IRRADIATED MATERIALS

In the Fourth HSST Irradiation Series, about one-half of the Charpy V-notch specimens from Capsule A were tested; the transition temperature shift is close to that predicted by *Regulatory Guide 1.99*, but the upper-shelf energy loss is less than predicted. Irradiation of Capsule B was completed. Capsule C was assembled and installed in the Bulk Shielding Reactor.

## 4. THERMAL SHOCK INVESTIGATIONS

A computer code OCA-I for performing thermal, stress, and fracture mechanics analyses for a pressurized-water reactor (PWR) pressure vessel subjected to transient thermal and pressure loading was completed and documented. The code is designed to perform parametric-type analyses for hypothetical accidents.

A parametric analysis was performed for an overcooling accident involving both temperature and pressure transients for sets of parameters characterizing fluence, copper content, and nil ductility transition reference temperature ($RT_{NDT}$).

Thermal shock experiment TSE-6 was proposed and approved. The thermal shock conditions will be similar to those of TSE-5A, and the heat treatment will be similar to that of TSE-5. The desired behavior is to initiate a shallow flaw that will jump almost through the wall in one event.

Interpretation of scatter in toughness data in the transition, lower-bound toughness, and effects of testing system compliance was studied. Testing machine compliance probably had little effect on lower-bound data obtained for TSE-5 and TSE-5A materials.

Further Charpy-V impact specimens of thermal shock prolongation TSP-2 have been tested.

## 5. PRESSURE VESSEL INVESTIGATIONS

In preparation for testing intermediate vessel V-8A with the flaw in a low-upper-shelf seam weld, characterization of the final trial weld was completed. Work was started by the Babcock & Wilcox Company to repair vessel V-8, make the special vessel seam weld, and make additional welds for use in flawing practice and material characterization. In test preparations at ORNL instrumentation studies are continuing, and a scale model of the vessel ballast was constructed.

Preparations are in progress for pressurized thermal shock testing of intermediate test vessels. Based upon a preliminary layout of a cooling system, parametric analyses of dimensions, heat transfer, and fluid flow indicate the feasibility of the test facility concept. Fracture mechanics analyses for combined loading are being made with the ADINAT and OR-FLAW codes to estimate initiation and arrest behavior for a broad range of conditions. Results show that the test facilty should be capable of producing fractures in a variety of modes.

The nozzle-corner flaw in intermediate vessel V-5, which leaked but did not burst, was removed from the vessel. The fracture surfaces were displayed and measured.

# HEAVY-SECTION STEEL TECHNOLOGY PROGRAM QUARTERLY PROGRESS REPORT FOR JANUARY—MARCH 1981*

G. D. Whitman R. H. Bryan

## ABSTRACT

The Heavy-Section Steel Technology (HSST) Program is an engineering research activity conducted by the Oak Ridge National Laboratory for the Nuclear Regulatory Commission. The program comprises studies related to all areas of the technology of materials fabricated into thick-section primary-coolant containment systems of light-water-cooled nuclear power reactors. The investigation focuses on the behavior and structural integrity of steel pressure vessels containing cracklike flaws. Current work is organized into five tasks: (1) program administration and procurement, (2) fracture mechanics analyses and investigations, (3) investigations of irradiated materials, (4) thermal shock investigations, and (5) pressure vessel investigations.

Finite-element computer codes for elastic-plastic fracture analysis are operational. Dynamic analyses of thermal shock experiments have been performed by subcontractors. Studies of lower-bound toughness measurement and ductile-brittle transition are in progress. Irradiation of the second capsule of specimens in the Fourth HSST Irradiation Series was completed, Charpy specimens from the first capsule were tested, and the third capsule was installed in the reactor. A computer code for parametric analysis of transient temperature and pressure loading of pressurized-water reactor vessels was completed. Thermal shock experiment TSE-6 was proposed. Preparations for intermediate vessel Test V-8A are continuing, and preliminary pressurized thermal shock test plans were formulated.

## 1. PROGRAM ADMINISTRATION AND PROCUREMENT

G. D. Whitman

The Heavy-Section Steel Technology (HSST) Program, a major safety program sponsored by the Nuclear Regulatory Commission (NRC) at the Oak Ridge National Laboratory (ORNL), is concerned with the structural integrity of the primary systems (particularly the reactor pressure vessels) of light-water-cooled nuclear power reactors. The structural integrity of these vessels is ensured by (1) designing and fabricating them according

---

*Conversions from SI to English units for all SI quantities are listed on a foldout page at the end of this report.

to standards set by the code for nuclear pressure vessels, (2) detecting flaws of significant size that occur during fabrication and in service, and (3) developing methods of producing quantitative estimates of conditions under which fractures could occur. The program is concerned mainly with developing pertinent fracture technology, including knowledge of (1) the material used in these thick-walled vessels, (2) the flaw growth rate, and (3) the combination of flaw size and load that would cause fracture and thus limit the life and/or operating conditions of this type of reactor plant.

The program is coordinated with other government agencies and with the manufacturing and utility sectors of the nuclear power industry in the United States and abroad. The overall objective is a quantification of safety assessments for regulatory agencies, for professional code-writing bodies, and for the nuclear power industry. Several activities are conducted under subcontracts by research facilities in the United States and through informal cooperative efforts on an international basis. Two research and development subcontracts are currently in force.

Administratively, the program is organized into five tasks, as reflected in this report: (1) program administration and procurement, (2) fracture mechanics analyses and investigations, (3) investigations of irradiated material, (4) thermal shock investigations, and (5) pressure vessel investigations.

During this quarter, nine program briefings, reviews, or presentations were made by the HSST staff at technical meetings and at program reviews for the NRC staff or visitors. Two technical reports were published.[1,2]

## References

1. S. K. Iskander, *Two Finite Element Techniques for Computing Mode I Stress Intensity Factors in Two- or Three-Dimensional Problems*, NUREG/CR-1499 (ORNL/NUREG/CSD/TM-14) (February 1981).

2. S. N. Atluri, B. R. Bass, J. W. Bryson, and K. Kathiresan, *NOZ-FLAW: A Finite Element Program for Direct Evaluation of Stress Intensity Factors for Pressure Vessel Nozzle-Corner Flaws*, NUREG/CR-1843 (ORNL/NUREG/CSD/TM-18) (March 1981).

# 2. FRACTURE MECHANICS ANALYSES AND INVESTIGATIONS

## 2.1 Nonlinear Computational Fracture Mechanics

B. R. Bass*

### 2.1.1 Introduction

In nonlinear computational fracture mechanics, the two variables most commonly used for computing stress-intensity parameters of cracks are crack-opening displacements and strain energy release rates. Certain studies indicate that the energy release technique is the more accurate of the two methods.[1] For two-dimensional (2-D) problems, the path-independent J-integral[2] can be conveniently used to calculate the energy release rate for both elastic and elastic-plastic material models. A procedure for J-integral computation was installed in the Oak Ridge version of finite-element program ADINA,[3] and the modified code was identified as ORJINT-2D;[4] the technique is demonstrated below in an elastic-plastic application. However, the extension of the J-integral to three dimensions is unwieldy because of the necessity of evaluating the J-function over defined surfaces in three-dimensional (3-D) space.

A method much better suited for 3-D calculations of energy release rates is the virtual crack extension technique introduced by Hellen[5] and Parks[6] in the context of finite elements. In this formulation, the finite-element mesh around the crack tip is given a virtual displacement to simulate extension of the crack. Recently, deLorenzi[7] derived an expression for the energy release rate from the viewpoint of continuum mechanics. By comparing the material body before and after the crack advance, deLorenzi shows that the energy release rate G is given by

$$G = G^{\star}/\Delta A \ , \tag{2.1}$$

where

$\Delta A$ = area covered by virtual crack extension (Fig. 2.1),

$$G^{\star} = \int_V \left[ \left( \sigma_{\alpha\beta} \frac{\partial u_\alpha}{\partial x_\delta} - W\delta_{\beta\delta} \right) \frac{\partial \Delta x_\delta}{\partial x_\beta} - f_\alpha \frac{\partial u_\alpha}{\partial x_\beta} \Delta x_\beta \right] dV \ . \tag{2.2}$$

In Eq. (2.2),

$\sigma_{\alpha\beta}$ = stress tensor,
$u_\alpha$ = displacement vector,
$W$ = internal energy density,
$f_\alpha$ = body force,
$\Delta x_\alpha$ = increment in virtual displacement,
$V$ = volume of the body.

---

*Computer Sciences Division, Union Carbide Corporation—Nuclear Division (UCC—ND).

ORNL-DWG 81-8731

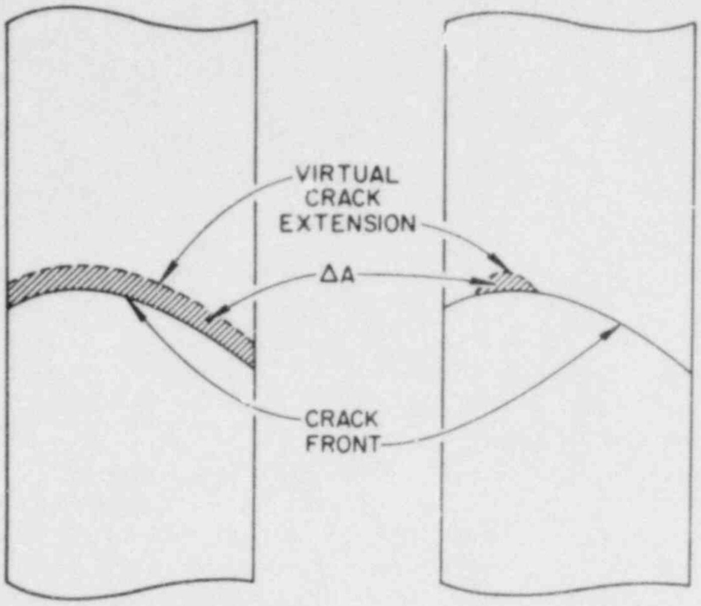

(*a*) UNIFORM EXTENSION (*b*) LOCAL EXTENSION

Fig. 2.1. Virtual crack extension for calculating energy release rate G for (a) uniform extension and (b) local extension.

Thus, average and local values of the energy release rate are evaluated from a natural extension of the volume integration already performed in the finite-element analysis. The formulation is valid for general fracture behavior, including nonplanar fracture, and applies to elastic as well as elastic-plastic material models.

During this quarter, program ORVIRT-3D was written at Oak Ridge by the Computing Applications Engineering Department to perform energy release rate calculations using the method of deLorenzi. The program functions as a postprocessor of results from a conventional ADINA finite-element solution. A detailed description of ORVIRT-3D, including user instructions, will be available in a forthcoming document. Results from an application of the program to a 3-D fracture analysis are described in the following section.

### 2.1.2 Three-dimensional numerical application

For purposes of validating program ORVIRT-3D, an elastic analysis was performed on a standard compact tension specimen (Fig. 2.2) previously analyzed by deLorenzi.[1,8] Figure 2.3 depicts the 3-D finite-element model of the specimen, consisting of 295 twenty-node isoparametric elements and 1476 node points. From symmetry considerations, only one-quarter of the specimen is modeled. Special quarter-point elements[9,10] were used at the crack tip [Fig. 2.3(b)] to represent the $1/\sqrt{r}$ singularity in the stress field. A line load was applied to the nodes at the top of the loading hole. Material properties for the model were specified as Young's modulus

ORNL-DWG 81-8732R

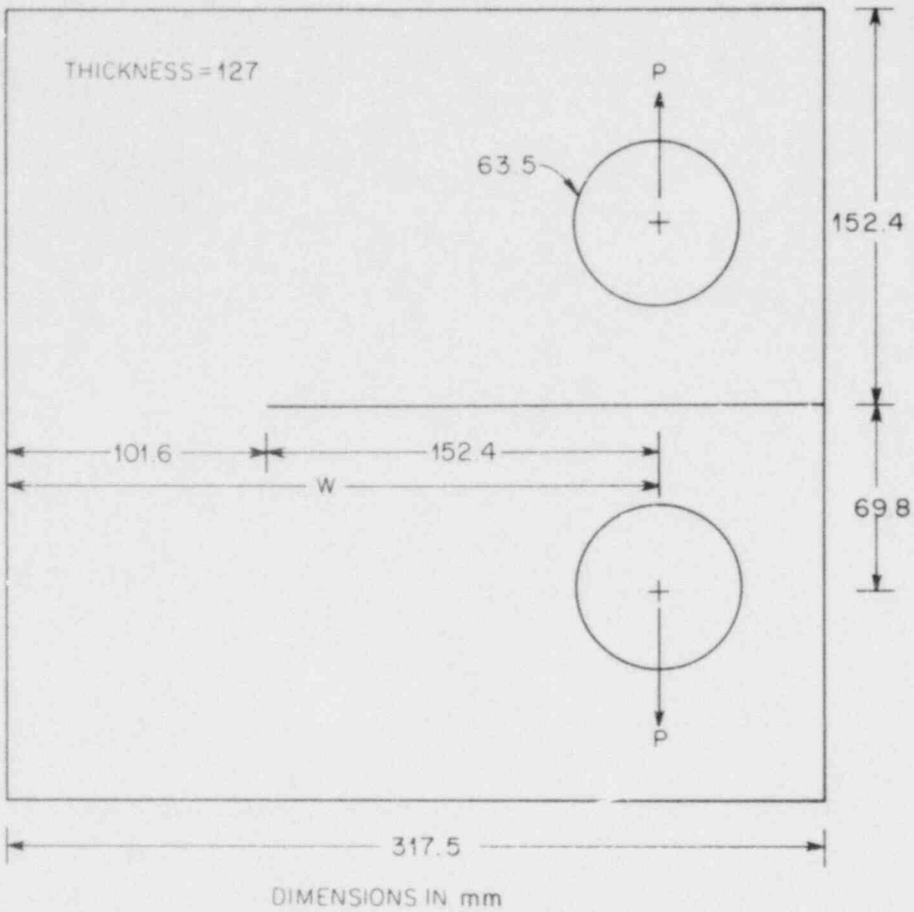

Fig. 2.2. Compact tension specimen geometry for ORVIRT-3D analysis.

$E = 207$ GPa and Poisson's ratio $\nu = 0.3$. For comparison, both plane strain and plane stress analyses were performed on the test specimen using the ORJINT-2D program. The finite-element mesh for the 2-D model was identical to that on the face of the 3-D model.

Table 2.1 shows the dimensionless crack-opening displacement vE/P, where v = crack opening at the load line and P = load per unit thickness, calculated for the plane strain, plane stress, and 3-D models. Included in the table are results from deLorenzi[1,8] and from the 2-D analysis of Newman.[11] The computed value for the 3-D model is closer to the plane stress result in both deLorenzi and the present study. Mode I stress-intensity factors $K_I$ are given in Table 2.2, where $K_I$ was calculated from the relation

$$K_I = \sqrt{GE'} \ , \qquad (2.3)$$

with

$$E' = E \text{ for plane stress or } E/(1 - \nu^2) \text{ for plane strain.} \qquad (2.4)$$

ORNL-DWG 81-8734

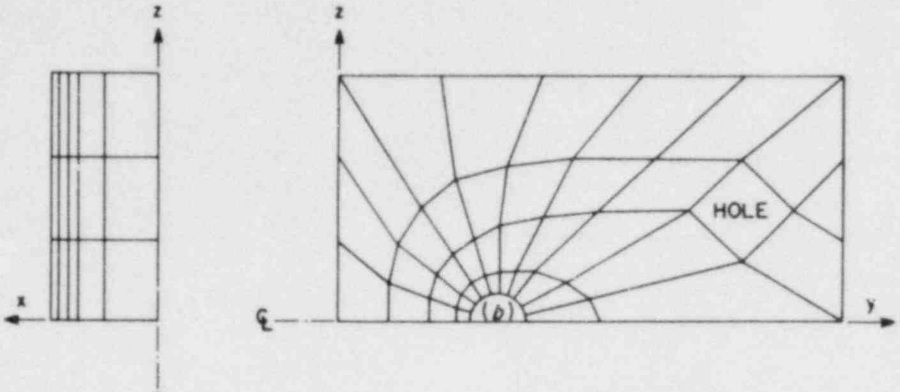

(a) FINITE ELEMENT MODEL

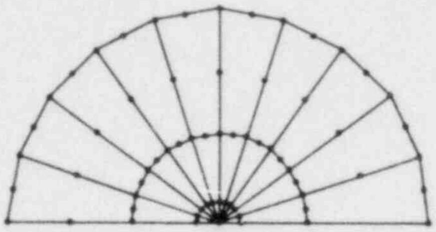

(b) DETAIL OF CRACK TIP ELEMENTS

Fig. 2.3. Finite-element model of compact tension specimen, consisting of 295 elements and 1476 nodes, for ORVIRT-3D analysis.

Table 2.1. Dimensionless crack opening displacement, vE/P

| Model | Method | | |
|---|---|---|---|
| | Present study | deLorenzi | Newman |
| Plane strain | 56.8 | 57.8 | 57.6 |
| Plane stress | 62.6 | 63.5 | 63.3 |
| 3-D model | 61.4 | 62.1 | |

For purposes of comparison with deLorenzi,[1,8] the plane strain value of E' was used exclusively in the 3-D computations.

The variations of the energy release rate G and the stress-intensity factor $K_I$ along the crack front in Fig. 2.4 are identical to those reported by deLorenzi.[1] The $G_{AVERAGE}$ value was computed by uniformly extending all nodes on the crack front and dividing the total energy release by the area increment of the extension. Local values of the energy

Table 2.2 Dimensionless stress-intensity factor, $K_I/\sqrt{w}\ P$[a]

| Model | Method | | |
|---|---|---|---|
| | Present study | deLorenzi | Newman |
| Plane strain | 13.6 | 13.6 | 13.6 |
| Plane stress | 13.6 | 13.6 | 13.6 |
| 3-D model average | 14.1[b] | 14.1[b] | |
| Centerline | 14.6[b] | 14.5[b] | |

[a] Figure 2.2 gives a definition of w.

[b] Three-dimensional values are computed from $K_I = \sqrt{GE/(1 - \nu^2)}$.

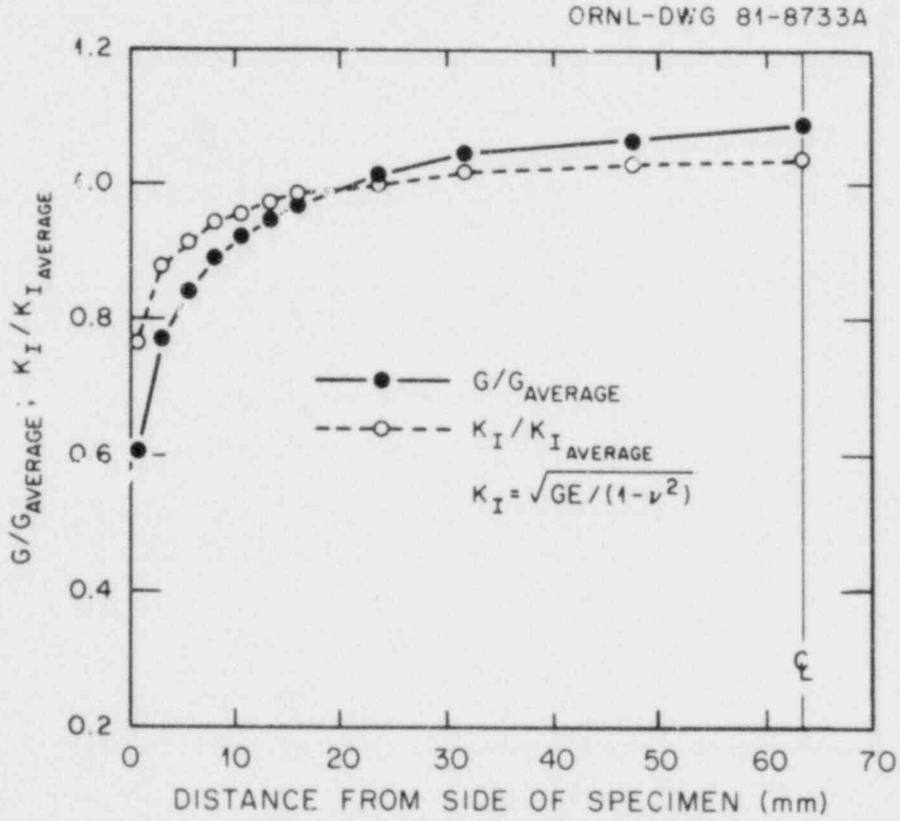

Fig. 2.4. Variation of energy release rate and stress-intensity factor along crack front for compact tension specimen.

release rate are determined by advancing one node at a time and calculating the area increment from the finite-element interpolation functions.

Current work under way includes application of program ORVIRT-3D to a 3-D elastic-plastic analysis of the compact tension specimen previously described. In this materially nonlinear analysis, the crack tip is modeled with 20-node collapsed prism elements to permit crack-tip blunting and to allow for a $1/r$ singularity[10] at the crack front. Results from this study will be reported in a future document.

### 2.1.3 Two-dimensional numerical applications

The Oak Ridge version of the ORJINT-2D program[4] was applied to the 2-D elastic-plastic analysis of a compact tension specimen (Fig. 2.5) previously studied by Atluri et al.[12] The present study made use of elastic-plastic material model 8 in ADINA, consisting of a von Mises yield condition with an isotropic strain-hardening rule. Two analytic stress-strain laws taken from Ref. 12 were employed. Both are represented by the

ORNL-DWG 81-8735R

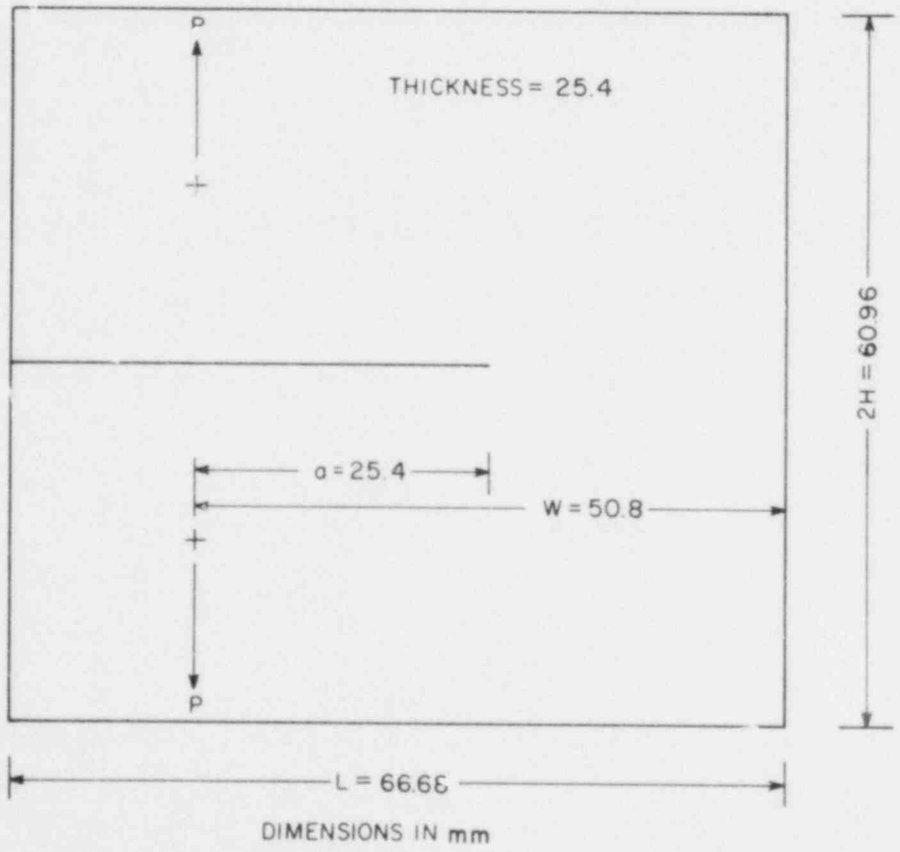

Fig. 2.5. Compact tension specimen configuration for ORJINT-2D elastic-plastic analysis.

Ramberg-Osgood relation:

$$\varepsilon = (\sigma/E) + (\sigma/B)^n , \qquad \sigma \geq \sigma_y , \tag{2.5}$$

$$\varepsilon = \sigma/E , \qquad \sigma < \sigma_y ,$$

where $\sigma_y$ = yield stress and where for law No. 1 $n = 6.971$, $B = 991.67$ MPa, and $\sigma_y = 207$ MPa, and for law No. 2 $n = 50$, $B = 563.44$ MPa, and $\sigma_y = 483$ MPa. In each case, $E = 201$ GPa and $\nu = 0.3$. Modifications were made to ORJINT-2D to accommodate a variable stress-strain tangent modulus $E_T$ given by

$$E_T = \partial\sigma/\partial\varepsilon = \frac{E}{1 + (nE/B)(\sigma/B)^{n-1}} ; \qquad \sigma \geq \sigma_y . \tag{2.6}$$

The finite-element model used in the analysis (Fig. 2.6) consists of 30 eight-noded isoparametric elements and 115 nodes. Because of symmetry

ORNL-DWG 81-8736

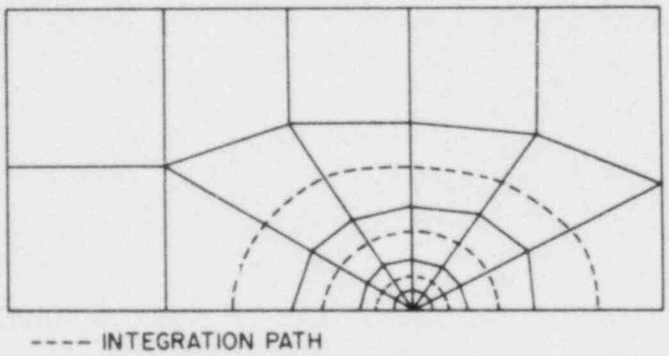

(a) FINITE ELEMENT MODEL

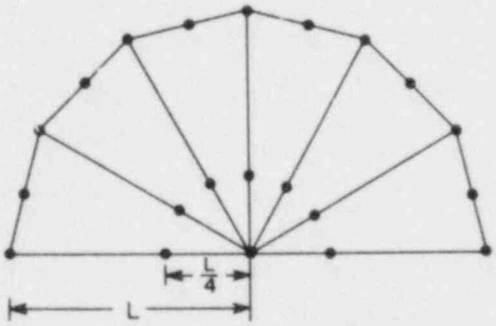

(b) DISTORTED ISOPARAMETRIC ELEMENTS AT CRACK TIP

Fig. 2.6. Finite-element model of compact tension specimen for ORJINT-2D analysis.

conditions, only one-half of the specimen is modeled. Also shown in Fig. 2.6 are the integration paths used to evaluate the J-integral at each load step. Degenerate 8-noded triangular elements are used to model the crack tip; a total of 13 nodes were positioned at the tip to permit crack-tip blunting in the loading cycle.

The first analysis consisted of elastic loading. For this case, the J-integral calculation gave a value of $K_I/P = 34.7\ \sqrt{\text{mm}}$ in the plane strain case. This value agrees well with the value of $K_I/P = 34.2\ \sqrt{\text{mm}}$ ($6.79\ \sqrt{\text{in.}}$) reported by Bucci et al.[13]

The results of the elastic-plastic analysis are reported in Fig. 2.7 for both the plane strain and the plane stress assumptions. Also included in the figure are experimental values determined by Bucci et al.[13] and Begley and Landes.[14] For both of the Ramberg-Osgood material laws, the plane stress representation compares more favorably with the experimental data points than does the plane strain solution.

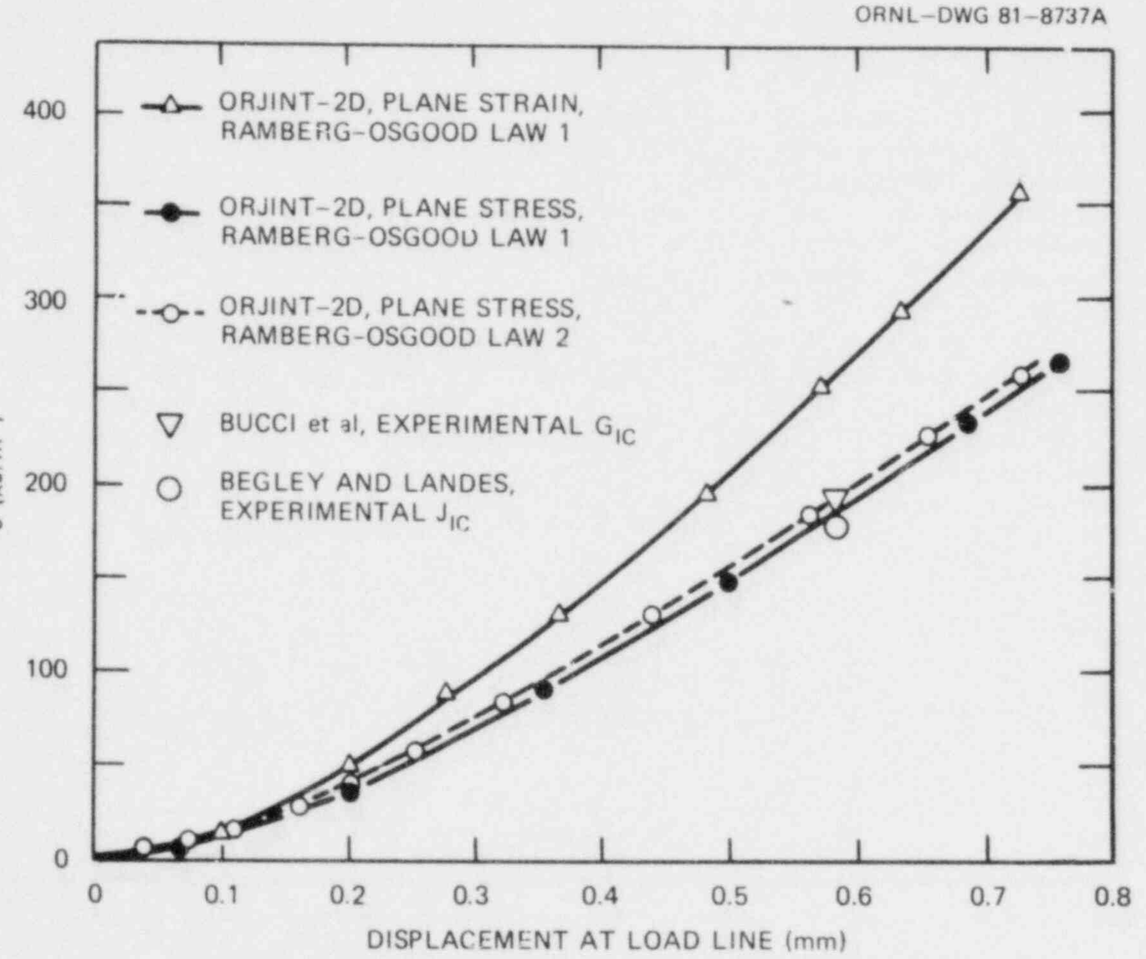

Fig. 2.7. J-integral vs load-line displacement for compact tension specimen by ORJINT-2D elastic-plastic analysis.

## 2.2 BCL HSST Support Program[*]

A. R. Rosenfield[†] J. Jung[†]
J. Ahmad[‡] M. F. Kanninen[†]
R. G. Hoagland[‡][†] C. W. Marschall[†]
D. K. Shetty[†]

### 2.2.1 Introduction and summary

The objective of the Battelle-Columbus Laboratories (BCL) HSST Support Program is to provide analytical and experimental research relevant to the fracture of steel cylinders subjected to thermal shocks. Particular attention is focused on analyzing crack propagation and arrest using appropriate material property data. The program consists of three research tasks:

1. dynamic fracture mechanics analyses,
2. lower-bound toughness determinations, and
3. determinations of fracture behavior of steel from TSE-6.

On Task 1, a dynamic finite-element analysis was made of the crack jumps in thermal shock experiment TSE-5A. Results showed that use of the crack arrest data from compact specimens underpredicted the actual jump lengths. Nevertheless, the results were closer than those found using a static analysis. The calculated crack jumps were also very sensitive to the choice of toughness values; replacing mean toughness by lower-bound toughness produced results in good agreement between analysis and experiment.

On Task 2, an analysis was made of the relative merits of spring loading and pneumatic loading for promoting crack instability. Results indicate that it might be possible to design a spring system whose weight is close to that of a piston and is only slightly less compliant. Fractographic examination of broken compact specimens was also made to locate weak spots in the microstructure, which are believed to trigger cleavage fracture. Preliminary results indicate that cleavage origins are associated with inclusions.

Task 3 will be initiated on receipt of the steel from the TSE-6 cylinder.

### 2.2.2 Task 1. Analysis of crack propagation and arrest

Basis of the analysis. An analysis of the ORNL thermal shock experiment TSE-5A was performed using a new BCL elastodynamic-crack-propagation-and-arrest finite-element code, FRACDYN. The current version of FRACDYN

---

[*] Work sponsored by HSST Program under UCC-ND Subcontract 85B-13876C between UCC-ND and BCL.

[†] BCL, Columbus, Ohio 43201.

[‡] Ohio State University.

is capable of analyzing 2-D static and dynamic plane stress, plain strain, or axisymmetric problems. The program employs eight-noded isoparametric quadratic elements.[15] Under static loading conditions, FRACDYN is capable of modeling not only externally applied loads and displacements but also thermal effects. Stress-intensity factors can be determined by either performing a J-integral evaluation or by employing quarter-point singularities in the elements adjacent to the crack tip.[16]

The dynamic capabilities of FRACDYN include the use of either lumped or consistent mass formulations. Time integration is performed either using a Newmark implicit scheme or a central difference explicit method.[15] Dynamic stress-intensity factors can also be calculated using a dynamic formulation of the J-integral.[17] Impact loading can be modeled by prescribing either forces or displacements as functions of time. The program also allows for impact, separations, and recontact with a rigid body.

The FRACDYN code can perform either generation-phase or application-phase analysis. In the former, a crack-length/time history is specified, and the facture toughness is computed. In contrast, in an application-phase analysis, the dynamic fracture toughness is specified and the crack-length/time history is sought. Generally, the dynamic fracture toughness can be a function of both crack velocity and temperature; that is, $K_{ID} = K_{ID}(V,T)$.

Analysis approach for TSE-5A. Separate dynamic computations of each of the four crack jump events detected in the experiment were performed. These application-phase analyses assumed that $K_{ID} = K_{Ia}$ and used BCL data for the latter quantity. Note that the $K_{Ia}$ data reported in BMI-2071 need to be corrected for ligament formation. Corrected values are given in Table 2.3.

Table 2.3. BCL crack arrest data for TSE-5A steel

| BCL specimen No. | Test temperature (°C) | $K_{Ia}$ ($MPa\cdot\sqrt{m}$) Originally reported | $K_{Ia}$ ($MPa\cdot\sqrt{m}$) Corrected for ligaments |
|---|---|---|---|
| 45 | 0 | 82 | 74 |
| 46 | 28 | 118 | 107 |
| 48 | 28 | 97 | 88 |
| 53 | 22 | 80 | 80 |
| 54 | 51 | 134 | 134 |
| 55 | 0 | 73 | 73 |

For the initial set of computations, a straight line representation of the data was made:

$$K_{Ia} = K_{ID} = 65 + 1.42T \ , \qquad (2.7)$$

where $K_{Ia}$ and $K_{ID}$ are in MPa$\cdot\sqrt{m}$ and T is in °C. This relation closely matches the ORNL characterization[18] of the $K_{Ia}$ data over the range of temperatures in which the data were taken. Dynamic computations were performed using Eq. (2.7) for initial crack positions as measured by both the ultrasonic transducers and the crack-opening displacement (COD) gages.

A second set of computations with the initial crack positions based on the ultrasonic transducer was also made using the ORNL temperature-shifted (17 K) $K_{Ia}$ curve.[18] The linear representation used in these analyses was

$$K_{Ia} = K_{ID} = [65 + 1.42(T - 17.0)] = 40.9 + 1.42T \ . \qquad (2.8)$$

This relation corresponds approximately to lowering the toughness at a given temperature by 24 MPa$\cdot\sqrt{m}$ from Eq. (2.7), which is essentially the estimated lower-bound value.[19] Equations (2.7) and (2.8) are shown in Fig. 2.8 along with the BCL experimental data.

A typical finite-element mesh used in these analyses is shown in Fig. 2.9. All of the computations employed 329 nodes and 96 eight-noded isoparametric elements. The stress-intensity factors were calculated by performing J-integral calculations that take thermal and dynamic effects into account.

An examination of the reproducibility of the BCL and ORNL analyses is made by performing static analyses of each crack jump at initiation and at arrest as measured by ultrasonic instrumentation (Table 2.4). As evident, the procedures are generally in good agreement. The maximum error is 9.7%, but most differences were less than ±5%.

Computational results. A comparison between the predicted crack jump lengths (based on initial crack positions as measured by the ultrasonic transducers) from the finite-element dynamic and the quasi-static analyses are given in Table 2.5. As expected, the dynamic analyses predict longer crack jumps than the corresponding quasi-static analyses. All of the quasi-static predictions based on the BCL compact tension data substantially underestimated the experimental results. In contrast, the dynamic computations gave close agreement between the experimentally measured crack jump lengths for the first and third crack jumps. The second and fourth computations underestimated the actual crack jumps, but not as severely as did the quasi-static procedure.

In the computations using the temperature-shifted $K_{Ia}$ curve [Eq. (2.8)], the quasi-static analyses were much improved. This is, of course, not too surprising because the shift of the data was made precisely to achieve this. However, with the single exception of the first jump, the dynamic analysis was still somewhat closer to the measured jump lengths. Again, the dynamic analyses in general predicted longer crack jumps than the corresponding quasi-static analyses. The exception was the third

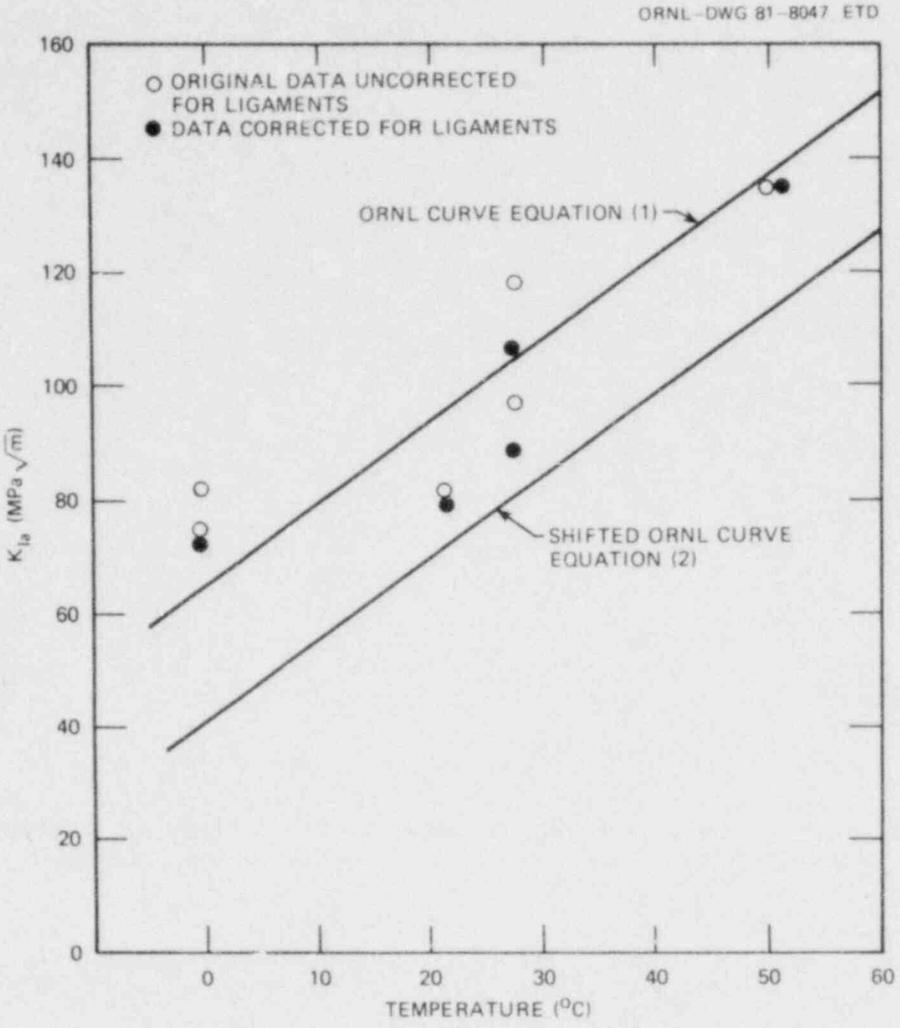

Fig. 2.8. $K_{Ia}$ TSE-5A material.

jump in which the quasi-static and dynamic predicted crack jumps were, within computational accuracy, essentially identical.

The sensitivity of the crack jump predictions to a variation in fracture toughness is shown in Fig. 2.10. This figure gives predicted crack jumps for the quasi-static and dynamic approaches. The plot using Eqs. (2.7) and (2.8) shows that the shifted toughness values from Eq. (2.8) produce static or dynamic crack jump predictions that are ~63% greater than values from Eq. (2.7), which is representative of BCL crack arrest data. Recalling that Eq. (2.8) corresponds to lowering the toughness at a given temperature by ~24 MPa$\cdot\sqrt{m}$ from Eq. (2.7), this figure illustrates that the TSE-5A results are fairly sensitive to relatively small changes in fracture toughness.

A comparison of quasi-static and dynamic predicted crack jump lengths based on initial crack positions deduced from the COD gages can also be made. Using Eq. (2.7) as the fracture toughness, the comparison is given in Table 2.6. Both the dynamic and quasi-static analyses underpredicted

ORNL–DWG 81–8048 ETD

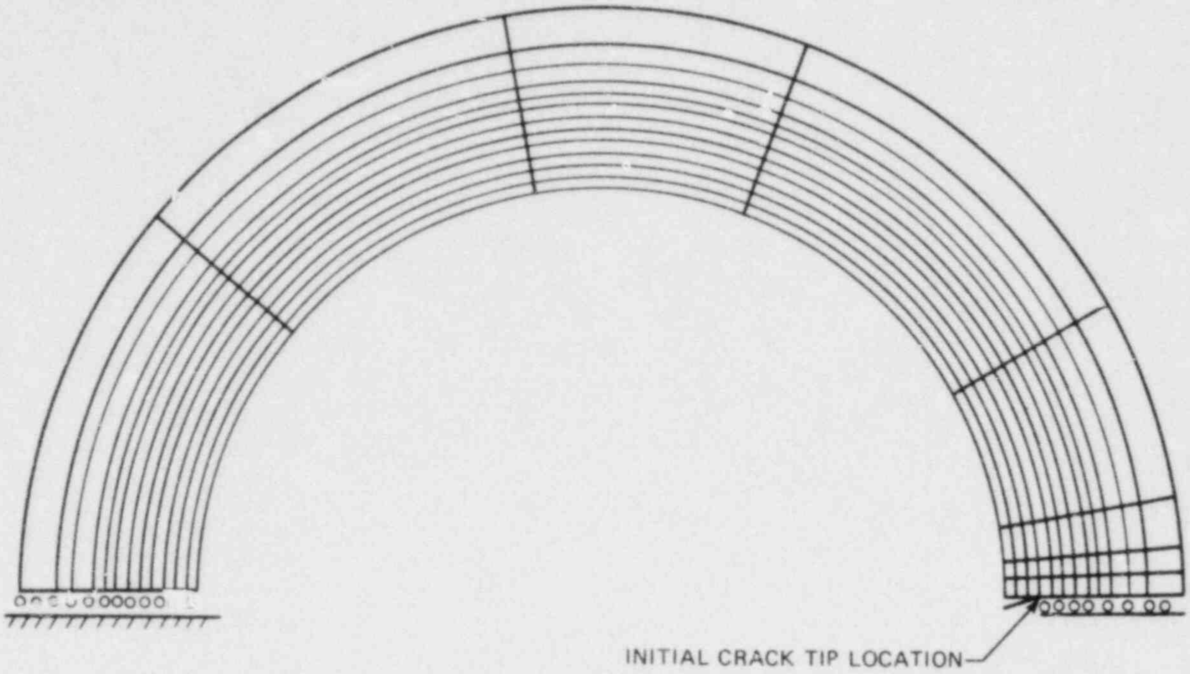

Fig. 2.9. Typical finite-element mesh for dynamic analysis.

Table 2.4. Comparison of stress-intensity factors computed with BCL and ORNL finite-element codes at initiation and arrest locations[a] in TSE-5A

| Event | K at initiation ($MPa\cdot\sqrt{m}$) | | Percent difference[b] | K at arrest ($MPa\cdot\sqrt{m}$) | | Percent difference[b] |
|---|---|---|---|---|---|---|
| | BCL | ORNL | | BCL | ORNL | |
| 1 | 64.1 | 70.3 | 9.7 | 78.3 | 74.7 | −4.6 |
| 2 | 86.8 | 83.5 | −3.8 | 85.6 | 85.7 | 0.12 |
| 3 | 114.1 | 107.6 | −5.7 | 108.2 | 107.7 | −0.46 |
| 4 | 142.2 | 135.1 | −4.7 | 137.0 | 129.6 | −5.40 |

[a] Based on ultrasonic data.

[b] Percent difference = (ORNL − BCL)/BCL × 100.

Table 2.5. Comparison of predicted and measured crack jump lengths in TSE-5A based on ultrasonic transducer data

| Event | Experimental lengths (mm) | Predicted lengths (mm) | | | |
|---|---|---|---|---|---|
| | | Using Eq. (2.7) | | Using Eq. (2.8) | |
| | | Dynamic | Quasi static | Dynamic | Quasi static |
| 1 | 5.78 | 6.60 | 2.14 | 13.3 | 5.19 |
| 2 | 13.7 | 7.25 | 3.81 | 17.8 | [illegible] 15 |
| 3 | 10.7 | 11.0 | 6.10 | 14.3 | 15.[illegible] |
| 4 | 39.7 | 27.2 | 23.3 | 43.8 | 36.6 |

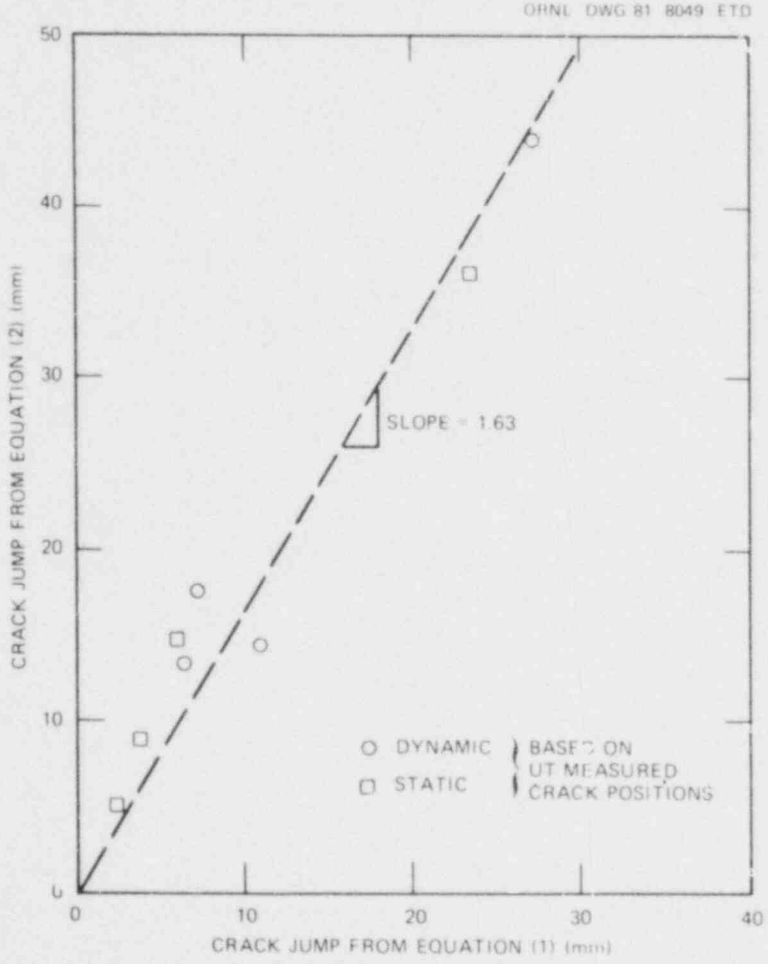

Fig. 2.10. The effect of the fracture toughness relation on predicted crack jump lengths.

Table 2.6. Comparison of predicted[a] and measured crack jump lengths in TSE-5A based on COD data

| Event | Experimental (mm) | Dynamic (mm) | Quasi static (mm) |
|---|---|---|---|
| 1 | 10.2 | 6.60 | 2.14 |
| 2 | 9.15 | 6.00 | 0.0 |
| 3 | 17.5 | 10.1 | 6.40 |
| 4 | 33.6 | 17.6 | 16.3 |

[a] Using Eq. (2.7).

the experimental results, but, again, the dynamic analyses predicted longer crack jumps than the quasi-static computations. The use of Eq. (2.7), together with the COD-deduced crack lengths, produced an inconsistent result for crack jump No. 2. For this event, the quasi-static approach predicted that no crack extension would occur at the time that the second jump took place.

Given that the toughness data for this material are sparse and subject to a great deal of scatter, it is difficult to conclude if a quasi-static analysis of TSE-5A is sufficient to describe the fracture events. Using the curve that described the original data [Eq. (2.7)], the quasi-static analysis will severely underpredict the crack jumps for both the ultrasonic and COD-based crack positions. The dynamic analysis also underpredicted but was at least close on two of the jumps for crack positions based on the ultrasonic transducer measurements. This basically unsatisfactory result is mainly caused by the uncertainty in the $K_{Ia}$ values — a conclusion that is partially borne out by the improvement noted when the data are shifted.

Although the concept of using a shifted toughness curve does give better agreement between the experimental and quasi-static analyses, the criteria for such a shift are generally unknown. Thus, this concept cannot be part of a predictive analysis procedure. Until more detailed toughness data are obtained, performing truly predictive analyses, either static or dynamic, will be difficult without introducing concepts such as toughness curve shifts which, in effect, fit the analyses to the experimental results.

During the next quarter, analysis of a full-scale vessel will be initiated.

### 2.2.3 Task 2. Lower-bound toughness values

Background. In earlier research, BCL investigators have examined material variability effects on both crack initiation[20] and crack arrest.[19] Research in this quarter emphasized crack initiation.

Table 2.7 and Fig. 2.11 summarize the status at the onset of the present program. As shown in Table 2.7, several methods were examined to analyze results using 1T compact tension specimens to determine the lower-bound crack initiation toughness at −4°C of steel from the TSE-5A vessel. Of these, an elastic energy method based on a suggestion of Seidl[21] gave the lowest and most reproducible results. The BCL lower-bound $K_{Ic}$ values also were close to the ORNL value for the same test temperature.

Table 2.7. Tabulation of lower-bound toughness ($K_{Ic}$) estimates obtained on CT specimens[a]

[Temperature = (−4°C)]

| Laboratory | Method | Number of specimens | Lower-bound $K_{Ic}$ (MPa·$\sqrt{m}$) | Coefficient of variation (%) |
|---|---|---|---|---|
| ORNL | Equivalent energy | 10 | 117[b] | 40[c] |
| BCL | Equivalent energy | 6 | 132 | 22 |
| BCL | Unloading compliance | 4 | 118 | 29 |
| BCL | Elastic energy | 6 | 111 | 4 |

[a] Data from Rosenfield and Shetty unless otherwise indicated.

[b] Data from R. D. Cheverton, "TSE-5A Quick Look Report" (1980).

[c] Data from R. D. Cheverton, private communication (1980).

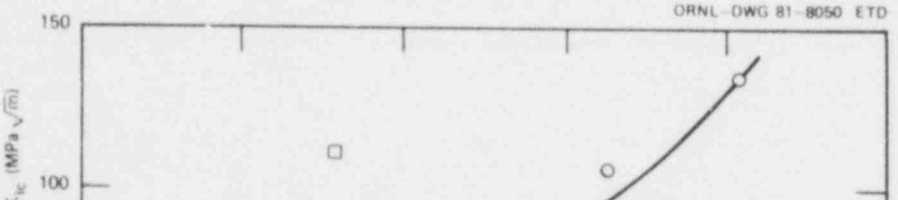

Fig. 2.11. Crack initiation fracture toughness.

The elastic energy method is a means of eliminating the contribution of stable crack growth to the measured load-displacement curve. In effect, it treats the nonlinear displacement associated with stable crack growth as irrelevant to the final instability associated with cleavage fracture. In practice, the method adopted by Rosenfield and Shetty[20] involves a linear-elastic calculation of fracture toughness at the moment of instability using the instantaneous values of load and crack length. The latter may be obtained either from fractographic examination or from an unloading compliance record.

Data presented by Witt[22] appear to be consistent with the elastic energy method. Witt reported failure loads of compact specimens over a wide range of thicknesses tested at 10 to 24°C. These loads were converted to stress intensities by assuming that no significant tearing occurred and by using the relations of Srawley.[23] As shown in Fig. 2.12, the resulting $K_{Ic}$ values are independent of thickness for all specimens that failed before reaching limit load and also for the 2T specimens that appear to have failed upon reaching limit load. Note that only the less tough 12T specimen is a valid result according to ASTM E399. The samples thinner than 2T produce apparently lower toughness for two possible reasons: (1) either they failed completely by dimpled rupture so that the elastic energy method is inappropriate or (2) they converted to cleavage after substantial tearing so that too short a crack length was inserted into the analysis. Despite this, these data do provide support for the

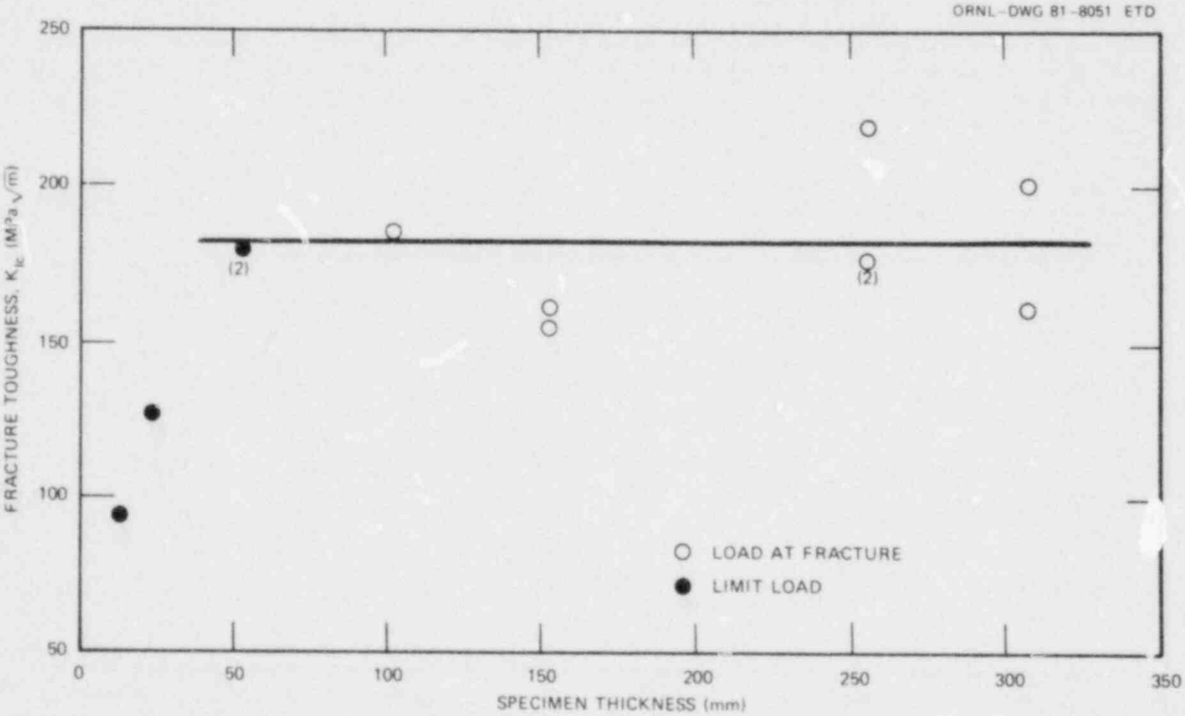

Fig. 2.12. Fracture toughness calculated using the elastic energy method of Witt.

idea that the elastic energy method is a valid means for obtaining lower-bound toughness values when the test specimen does not reach limit load.

The difficulty with results based on the elastic energy method is that the $K_{Ic}$ values for the TSE-5A vessel fall considerably below the values for 1T specimens (Fig. 2.11). The reasons for this discrepancy are not clear. Current plans of this program call for examining two areas: (1) promotion of cleavage failure by use of a soft loading system and (2) examination of a statistical explanation.

Soft loading systems. Recent experiments have shown that conversion from stable dimpled-rupture crack growth to unstable cleavage fracture is promoted by use of a soft loading system.[24] To reduce the stiffness of their machine, Gudas and Joyce inserted a steel bar loaded in three-point bending in series with their specimen. In current work at BCL, the initial plan was to search for lower-bound toughness values by using an even softer deadweight machine. However, conventional machines, such as creep stands, have a large inertia, which may partially nullify the effects of their reduced stiffness. To reduce the mass, it would be necessary to approximate dead loading by applying the load with a hydraulic or pneumatic cylinder.

To insure that the dead-loading system is an appreciable improvement over a spring system, some preliminary calculations have been carried out to ascertain the achievable characteristics of the spring-loaded system. Both mass and compliance need to be taken into account. The question to be investigated is whether the compliance of the spring can be made sufficiently high so that further increases produce only a marginal benefit. At the same time, the mass of the spring must not be significantly greater than the mass of the plunger in any hydraulic or pneumatic system.

The spring can be considered as a simply supported beam of span L, depth H, and thickness $B_m$, which is loaded by a force P. If the load-point displacement is $y_m$ and the modulus $E_m$, the compliance $\phi_m$ is given by

$$\phi_m = E_m B_m y_m / P = (1/4)(L/H)^3 , \qquad (2.9)$$

so that

$$L/H = (4\phi_m)^{1/3} . \qquad (2.10)$$

The spring must also be able to support the load elastically, so that the maximum stress is

$$\alpha\sigma_y = 1.5PL/B_m H^2 , \qquad (2.11)$$

where $\alpha$ is a safety factor and $\sigma_y$ is the yield stress. Combining Eqs. (2.10) and (2.11),

$$\sigma_y = (1.5P/\alpha B_m H)(4\phi_m)^{1/3} . \qquad (2.12)$$

The mass M of the beam is given by

$$M = \rho_m B_m LH \ , \tag{2.13}$$

where $\rho_m$ is the density. Combining Eqs. (2.12) and (2.13),

$$M = [1.5P\rho L(4\phi_m)^{1/3}]/\alpha\sigma_y \ . \tag{2.14}$$

Equation (2.14) defines the mass associated with a given spring compliance. The next step is to evaluate whether a spring can be made compliant enough to approximate dead loading. The analysis is based on the crack stability calculations of Clausing,[25] who treated the specimen and machine as two springs in series. Accordingly,

$$y/P = \lambda = \lambda_m + \lambda_s \ , \tag{2.15}$$

where y is total displacement with $\lambda_m$ and $\lambda_s$ being the machine and specimen contributions to compliance, respectively. The strain energy release rate G is given by

$$G = (P^2Y^2/B_s^2w^2)a \ , \tag{2.16}$$

where $B_s$ is the thickness and Y is a function of a/w (crack length/specimen width), which can be evaluated from Srawley.[23] Combining Eqs. (2.15) and (2.16) and differentiating,

$$\frac{1}{G}\frac{dG}{da} = \frac{2}{Y}\frac{dY}{da} + \frac{2}{y}\frac{dy}{da} - \frac{2}{\lambda}\frac{d\lambda}{da} + \frac{1}{a} \ . \tag{2.17}$$

Equation (2.17) shows that crack stability, which is reflected in the parameter dG/da, is influenced by the compliance of the load train which contributes to $\lambda$. Furthermore, the machine compliance is independent of crack length so that

$$d\lambda/da = d\lambda_s/da \ . \tag{2.18}$$

In analyzing the compliance effect, one limiting condition is the perfectly stiff machine where, for a virtual extension of the crack,

$$dy/da = 0 \ . \tag{2.19}$$

Note that Eq. (2.19) will apply to the onset of rapid fracture accompanying instability. Another characteristic of the perfectly stiff machine is that $\lambda = \lambda_s$ so that

$$\left(\frac{1}{G}\frac{dG}{da}\right)_0 = \frac{2}{Y}\frac{dY}{da} - \frac{2}{\lambda_s}\frac{d\lambda_s}{da} + \frac{1}{a}\ , \tag{2.20}$$

where the subscript 0 refers to a perfectly stiff machine.

Real machines can be considered as departures from perfect stiffness. Combining Eqs. (2.17) through (2.20),

$$\frac{1}{G}\frac{dG}{da} - \left(\frac{1}{G}\frac{dG}{da}\right)_0 = 2\,\frac{d\lambda_s}{da}\left(\frac{1}{\lambda_s} - \frac{1}{\lambda}\right)\,. \tag{2.21}$$

Equation (2.21) defines the relative crack stability in terms of machine and specimen compliance. If $\lambda_m$ is set to equal $\beta\lambda_s$, Eq. (2.21) becomes

$$\frac{1}{G}\frac{dG}{da} - \left(\frac{1}{G}\frac{dG}{da}\right)_0 = \frac{2}{\lambda_s}\frac{d\lambda_s}{da}\,(\beta/\beta + 1)\ . \tag{2.22}$$

The term on the right is very insensitive to $\beta$ provided $\beta >> 1$. In the limit of a perfectly soft machine, $\beta = \infty$ and $\beta/(\beta + 1) = 1$.

Values of $\beta$ were calculated from Eqs. (2.10), (2.13), and (2.14) for hardened, SAE 4340, rectangular steel springs using the values $\sigma_y = 1380$ MPa, $\rho_m \approx 7750$ kg/m$^3$, $\alpha = 3/4$, and $\lambda_s = 1.1 \times 10^{-5}$ mm/N; these values are characteristic of a 1T compact steel specimen when $a/w = 0.6$ (Ref. 26). The results are shown in Table 2.8, and examination of them shows that $\beta \approx 3.3M$. Thus, a value of $\beta = 20$ corresponds to a mass of 6.12 kg. This value can be obtained with beam dimensions of L, B, and H equal to 914, 12.7, and 68.3 mm, respectively.

A value of $\beta = 20$ corresponds to $\beta/(\beta + 1) = 0.95$, which is close to ideal softness. Further increases in $\beta$ and/or decreases in M can be made by using a material with a higher strength-per-mass ratio or by altering the beam design.

Turning to softer machines, a creep stand with a 20:1 lever arm would result in $\beta = \infty$ so that $\beta/(\beta + 1) = 1.00$, but it would require a mass in excess of 230 kg. Lower weights could be obtained with hydraulic or pneumatic loading as sketched schematically in Fig. 2.13. In this case,

$$\lambda_m \approx (k\ell_f/A_f) + (\ell_p/EA_p)\ , \tag{2.23}$$

where k is the compressibility of the fluid. For hydraulic oil, $k \approx 7 \times 10^{-3}$ MPa$^{-1}$. The second term is negligible so that $\lambda_m \approx 3 \times 10^{-4}$ mm/N, and $\beta/(\beta + 1) = 0.96$ using the dimensions in Fig. 2.13. This compliance is only a 25% improvement over a 6-kg rectangular steel beam, but the mass is decreased to 2.5 kg or by a factor of about 2.5 over the beam.

Table 2.8 Mass and stiffness of candidate beam proportions for SAE-4340 steel

(Yield strength = 1.4 GPa)

| $\phi$ | Dimensions (mm) | | | Mass (kg) | Beam compliance $\lambda_m$ ($10^{-5}$ mm/N) | $\beta$ |
|---|---|---|---|---|---|---|
| | B | L | H | | | |
| 300 | 11.9 | 610 | 57.4 | 3.22 | 12.2 | 10.6 |
| 300 | 8.1 | 914 | 86.1 | 4.85 | 18.2 | 15.9 |
| 450 | 12.4 | 762 | 62.7 | 4.63 | 17.5 | 15.3 |
| 600 | 37.8 | 305 | 22.9 | 2.04 | 7.7 | 6.7 |
| 600 | 19.1 | 610 | 45.5 | 4.08 | 15.2 | 13.3 |
| 600 | 14.0 | 838 | 62.5 | 5.62 | 20.9 | 18.3 |
| 600 | 12.7 | 914 | 68.3 | 6.12 | 22.8 | 20.0 |
| 900 | 18.0 | 838 | 54.6 | 6.44 | 24.2 | 21.1 |
| 1200 | 60.2 | 305 | 18.0 | 2.59 | 10.2 | 8.4 |
| 3000 | 74.2 | 457 | 20.1 | 5.26 | 19.6 | 17.2 |
| 3000 | 55.4 | 610 | 26.7 | 6.99 | 26.2 | 22.9 |
| 3000 | 44.2 | 762 | 33.3 | 8.71 | 32.8 | 28.7 |
| 3000 | 34.3 | 991 | 43.2 | 11.34 | 42.3 | 37.0 |

ORNL-DWG 81-8052 ETD

$A_f$ = 6500 mm$^2$
$A_r$ = 650 mm$^2$
$\ell_f$ = 250 mm
$\ell_p$ = 25 mm
$\ell_r$ = 250 mm

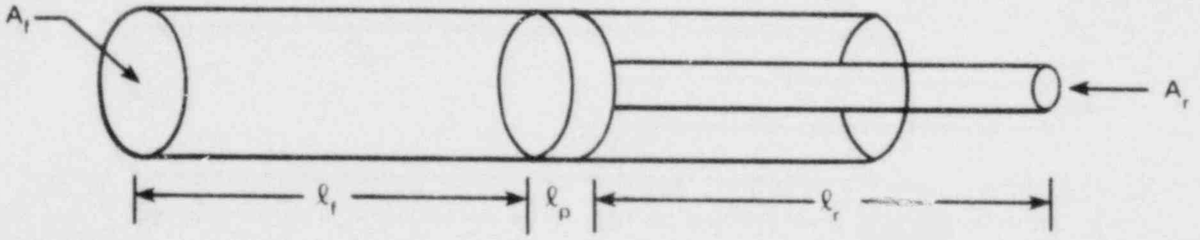

Fig. 2.13. Schematic diagram of soft loading system.

However, if pneumatic loading is used, $k \approx 1/p$ where p is pressure. Setting $p = 7$ MPa, $\lambda_m = 0.005$ mm/N and $\beta/(\beta + 1) = 0.998$. The weight would be the same as for the hydraulic cylinder.

Table 2.9 lists the possible alternatives for soft loading. Because none of these systems have been optimized, their characteristics should be better than those listed on the table. At this point, whether the additional cost and safety considerations are balanced by the greater efficiency of the pneumatic loading is not clear. Further consideration will be given to these problems early in the next quarter before a final decision is made as to system design.

Table 2.9. Characteristics of candidate soft-loading systems

| Loading system | Mass (kg) | Relative softness $\beta/(\beta + 1)$ |
|---|---|---|
| Dead load | 230 | 1.00 |
| Pneumatic cylinder | 2.5 | 0.998 |
| Hydraulic cylinder | 2.5 | 0.96 |
| Leaf spring | 2.5 | 0.89 |
| Leaf spring | 7.6 | 0.96 |

Statistical approach to lower-bound toughness. One possible reason for the lower toughness of the 1T specimens when compared with the large cylinder is a size dependence of $K_{Ic}$. Leaving aside questions of thickness requirements for valid plane strain data (which may be important), a weakest-link explanation is being explored. According to this explanation, brittle spots exist in the steel that can trigger cleavage fracture. If this is the case, the statistical fracture theory of Weibull[27] should apply.

According to Weibull's analysis, the cumulative failure probability F is

$$F = 1 - \exp(-\int_V \sigma^m \, dV) , \tag{2.24}$$

where σ is the local value of stress in a volume element dV and m is a material property characterizing the breadth of the failure stress distribution. The only data on metals (that BCL investigators are aware of) that can be used to test Eq. (2.24) are those of a Cr-Mo-V steel studied by Kotilainen[28] (Fig. 2.14). These data can be interpreted as implying

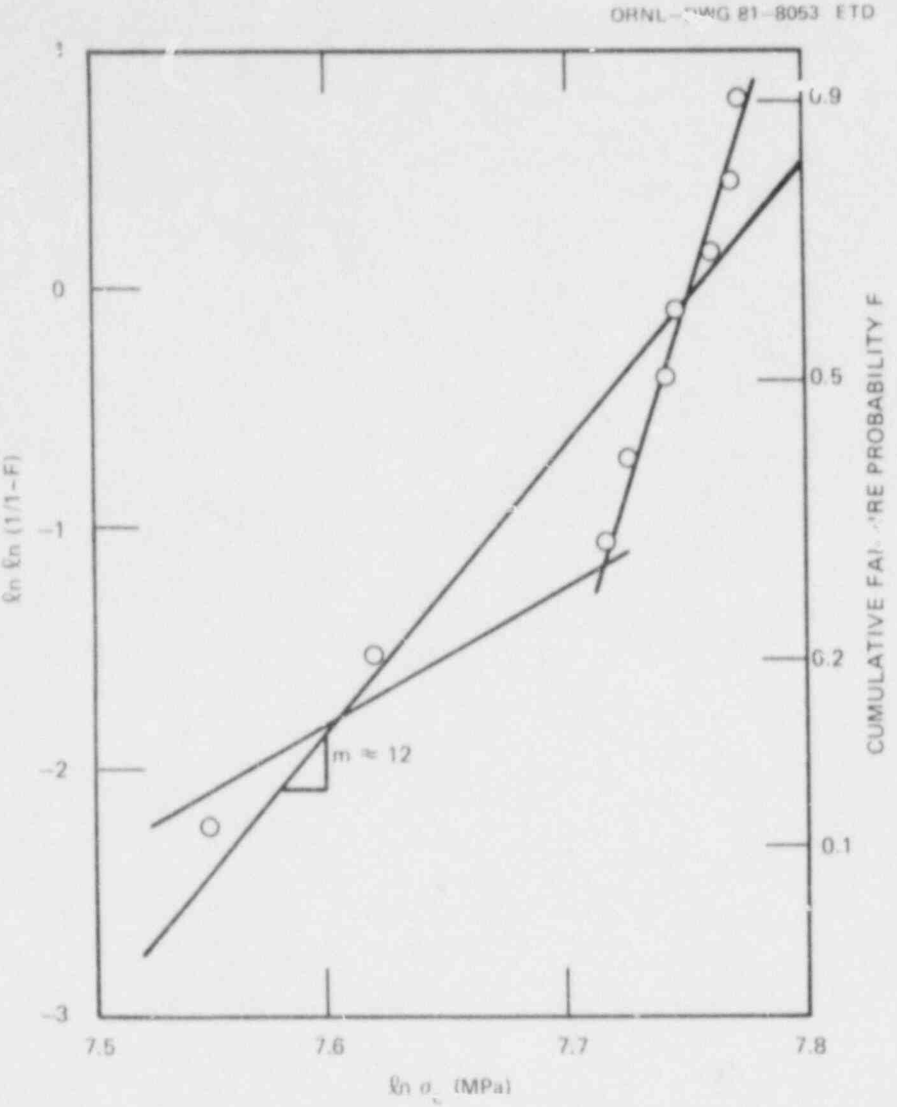

Fig. 2.14. Weibull plot of cleavage strength for Cr-Mo-V steel.

a bimodal flaw distribution. The flaws giving rise to low failure probabilities are somewhat more rare than those causing fracture in the majority of specimens. However, for the balance of this discussion, an average m value of 12 will be used for simplicity.

Adaptation of the Weibull methodology to precracked steel specimens has been discussed by Hahn et al.[29] The method is based on the now generally accepted idea of Ritchie et al.[30] that cleavage fracture is nucleated by slip-induced fracture of carbide particles. Accordingly, the effective specimen size is the size of the crack-tip plastic zone. Fracture in two specimens is equally probable when

$$\sigma_1^m V_1 = \sigma_2^m V_2 , \qquad (2.25)$$

if the average stress is used instead of the local stress in Eq. (2.24). In a precracked specimen the local stress is $\alpha'\sigma_y$, where $\alpha'$ is a constraint factor and $\sigma_y$ is the flow strength, and the specimen volume is $\alpha''(K_{Ic}/\sigma_y)^4$ where $\alpha''$ is another proportionality constant. If $\sigma_c$ is the cleavage fracture stress of a smooth bar specimen corresponding to the same probability level, Eq. (2.25) becomes

$$(K_{Ic}/\sigma_y)^4 = \alpha(\sigma_c/\sigma_y)^m \ . \tag{2.26}$$

As discussed by Kotilainen,[28] Eq. (2.26) has been derived in alternative ways by other authors and has been confirmed experimentally. Figure 2.15 shows one example, using the same steel as in Fig. 2.14. Because the value of m associated with Fig. 2.15 is 16, the agreement with the value of 12 from Fig. 2.14 is only fair. However, the two values are not too far apart considering the approximate nature of the analysis.

ORNL-DWG 81-8054 ETD

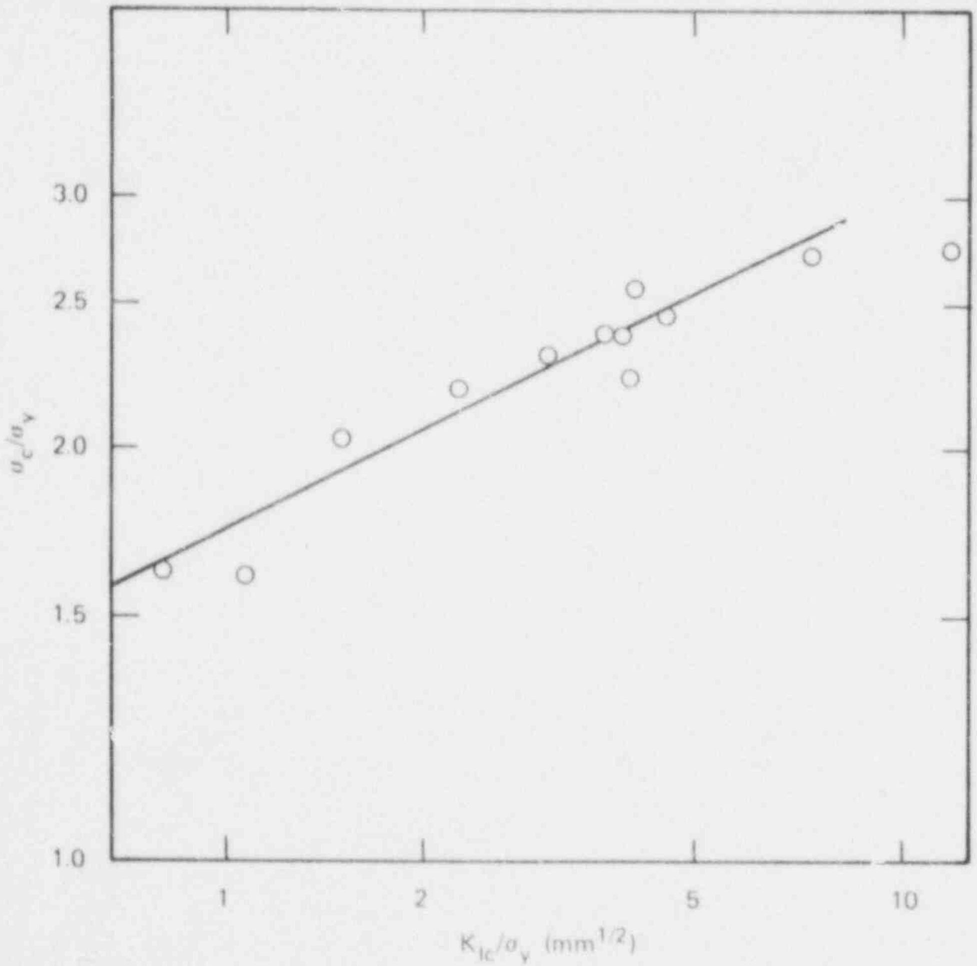

Fig. 2.15. Relation among cleavage strength, yield strength, and fracture toughness.

Although the statistical analysis has not yet been extended to include predictions of an effect of thickness on $K_{Ic}$, clearly such predictions are within its scope. From Eq. (2.[illegible]6) the toughness ($K_{Ic}$) variability can arise from either variations in yield strength ($\sigma_y$) or in cleavage strength ($\sigma_c$). While there is some scatter in yield strengths of steels,[31] a size dependence of $\sigma_y$ large enough to explain the discrepancy between 1T specimens and the TSE-5A vessel is unlikely. The more plausible explanation is that weak spots in the microstructure trigger cleavage. For this reason, a fractographic study has been undertaken to attempt to isolate these weak spots.

<u>Fractography</u>. The fracture toughness ($K_{Ic}$) measurements on the ORNL TSE-5A steel, conducted at BCL in support of the ORNL thermal shock experiment, exhibited large scatter.[19] This is typical of most plain carbon and low-alloy steels in the ductile-brittle transition region.[20] A fractographic study was initiated on the 1T compact specimens with the objective of providing a microstructural rationale for the observed variations in $K_{Ic}$. Preliminary fracture surface observations on three specimens indicated that the toughness variations were associated with different extents of stable crack growth by the dimple-rupture mechanism that was followed by unstable fracture by the cleavage mode. The cleavage fracture was triggered from identifiable stress on the stable crack front or slightly ahead of it. This observation was consistent with the concept of weak spots in the microstructure leading to the scatter and size dependence of fracture toughness.

Two additional specimens, identified by the numbers 2TP 36 and 2TP 33 from the original batch of six 1T compact specimens received from ORNL, were examined by fractography techniques. In these studies, efforts were concentrated on locating and identifying the microstructural feature(s) triggering the cleavage mode of fracture (Figs. 2.16 through 2.19). Figures 2.16(a) and 2.18(a) show the low-magnification optical fractographs corresponding to the specimens 2TP 36 and 2TP 33, respectively. Fracture origins in each of these specimens could be easily located by following the chevron patterns radiating outward from the origins. Small regions surrounding the origins, indicated by the arrows and the boxes in Figs. 2.16(a) and 2.18(a), were further examined in a scanning electron microscope. Figures 2.16(b) and 2.18(b) are low-magnification scanning electron fractographs of the boxed regions in Figs. 2.16(a) and 2.18(a), respectively. The radiating ridges can still be identified, and the suspected fracture initiation points are indicated by the arrows. Figures 2.17(a and b) and 2.19(a and b) are higher-magnification fractographs of these initiation points. As seen in these figures, the fracture-initiation points in both of these specimens contain inclusions. Two features of these inclusions are noteworthy. They show large, flat, featureless surfaces parallel to the fracture surface that were presumably the inclusion/matrix interfaces prior to the fracture. Secondly, the inclusions are like hollow shells with a porous material inside [Fig. 2.19(b)]. Several inclusions can be noted in the fracture-initiating region, and these are indicated by the arrows in Figs. 2.17(a) and 2.19(a). The inclusions suspected to have initiated the cleavage fracture are the large ones in the center of the fields [Figs. 2.17(b) and 2.19(b)]. No chemical analysis was done on these inclusions, but they are very likely to be manganese sulfide. The occurrence of the flat surfaces of the inclusions,

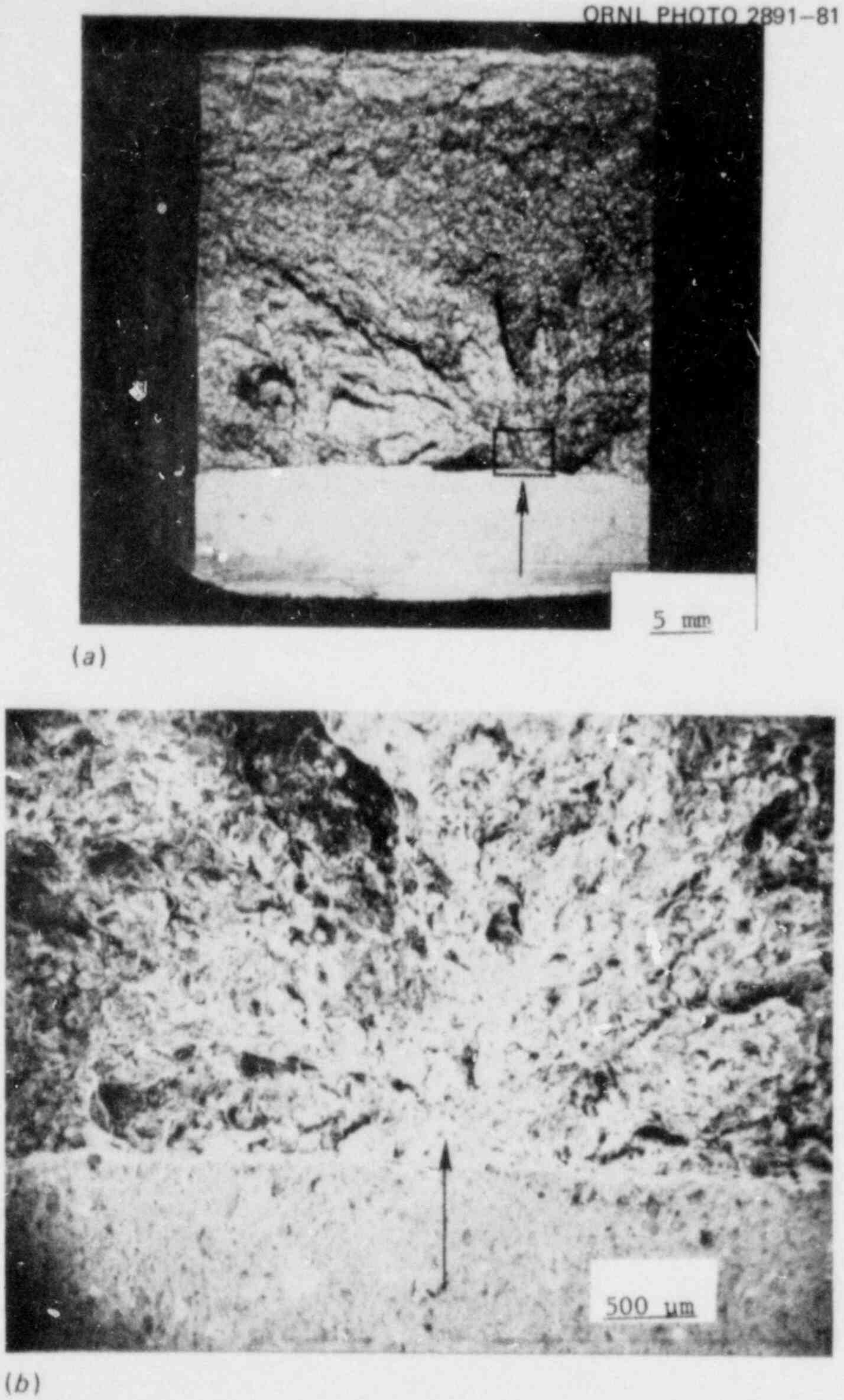

Fig. 2.16. Fracture surface of 1T compact specimen (2TP36) of ORNL steel tested at −4°C. (a) Arrow and box identify fracture origin, (b) fracture-initiation region corresponds to box in (a).

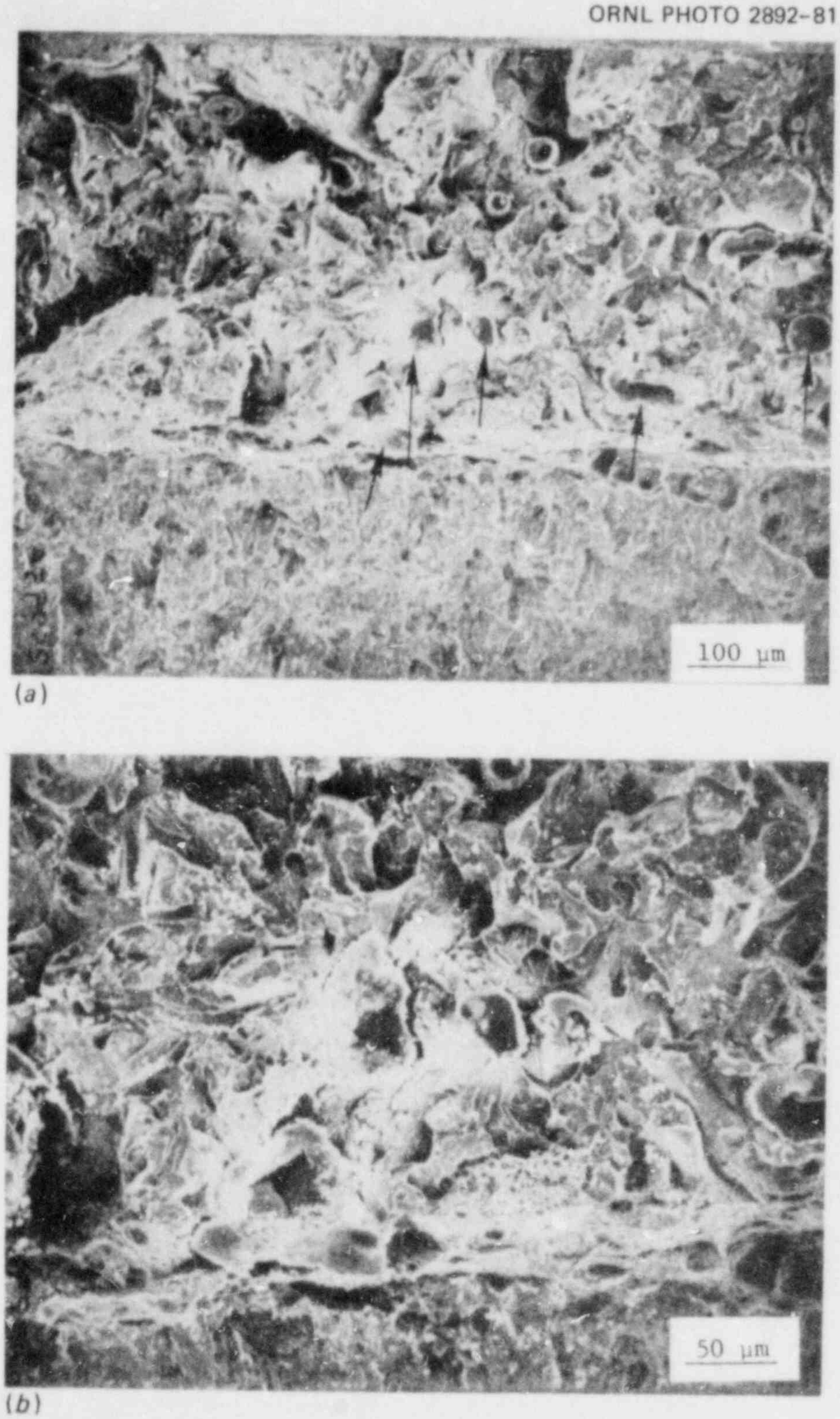

Fig. 2.17. Cleavage fracture-initiation site in specimen 2TP36. (a) Inclusions indicated by arrows, (b) group of closely placed inclusions at the cleavage fracture origination site.

ORNL PHOTO 2893–81

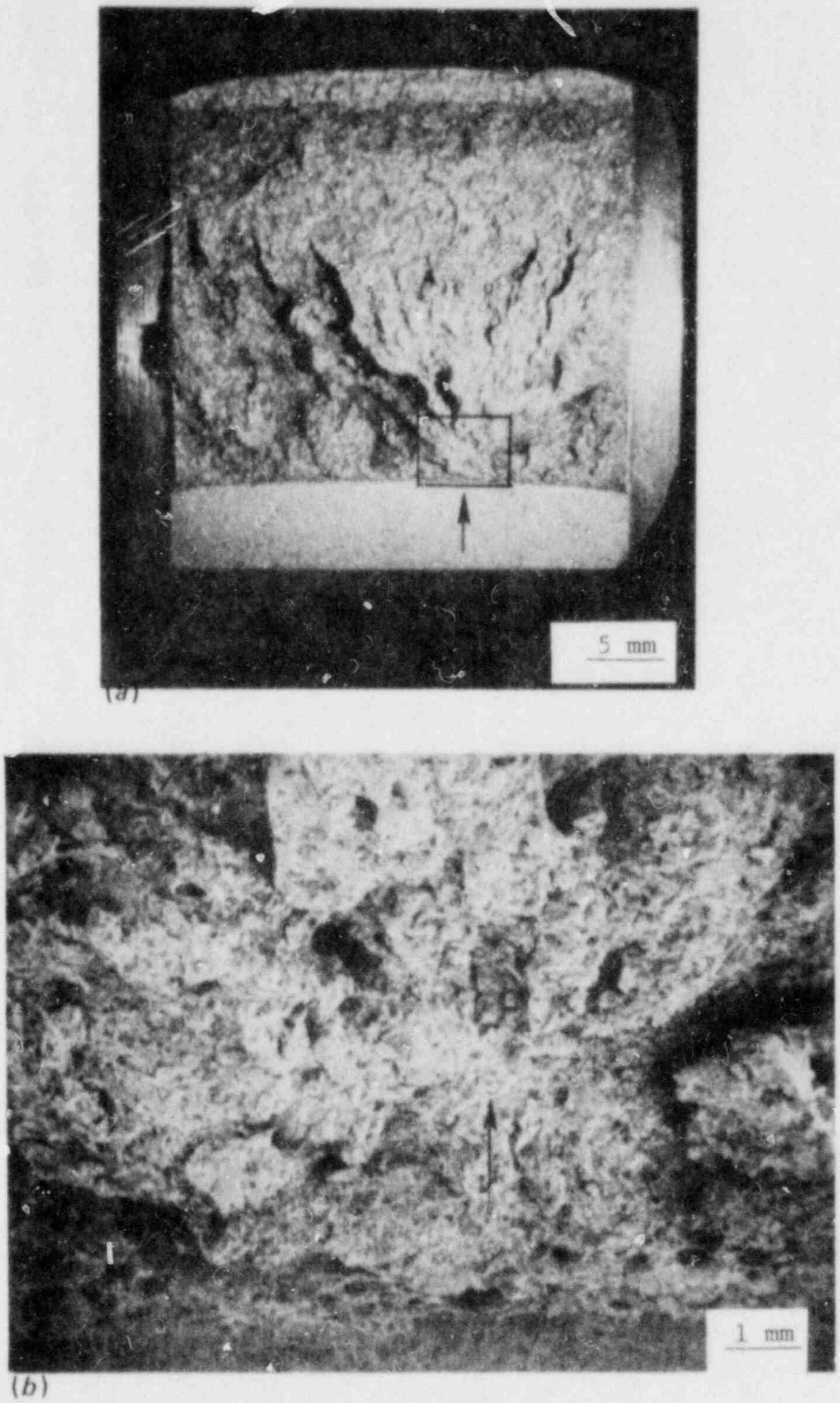

Fig. 2.18. Fracture surface of 1T compact specimen (2TP33) of ORNL steel tested at −4°C. (a) Arrow and box identify fracture origin, (b) fracture-initiation region corresponds to box in (a).

ORNL PHOTO 2894-81

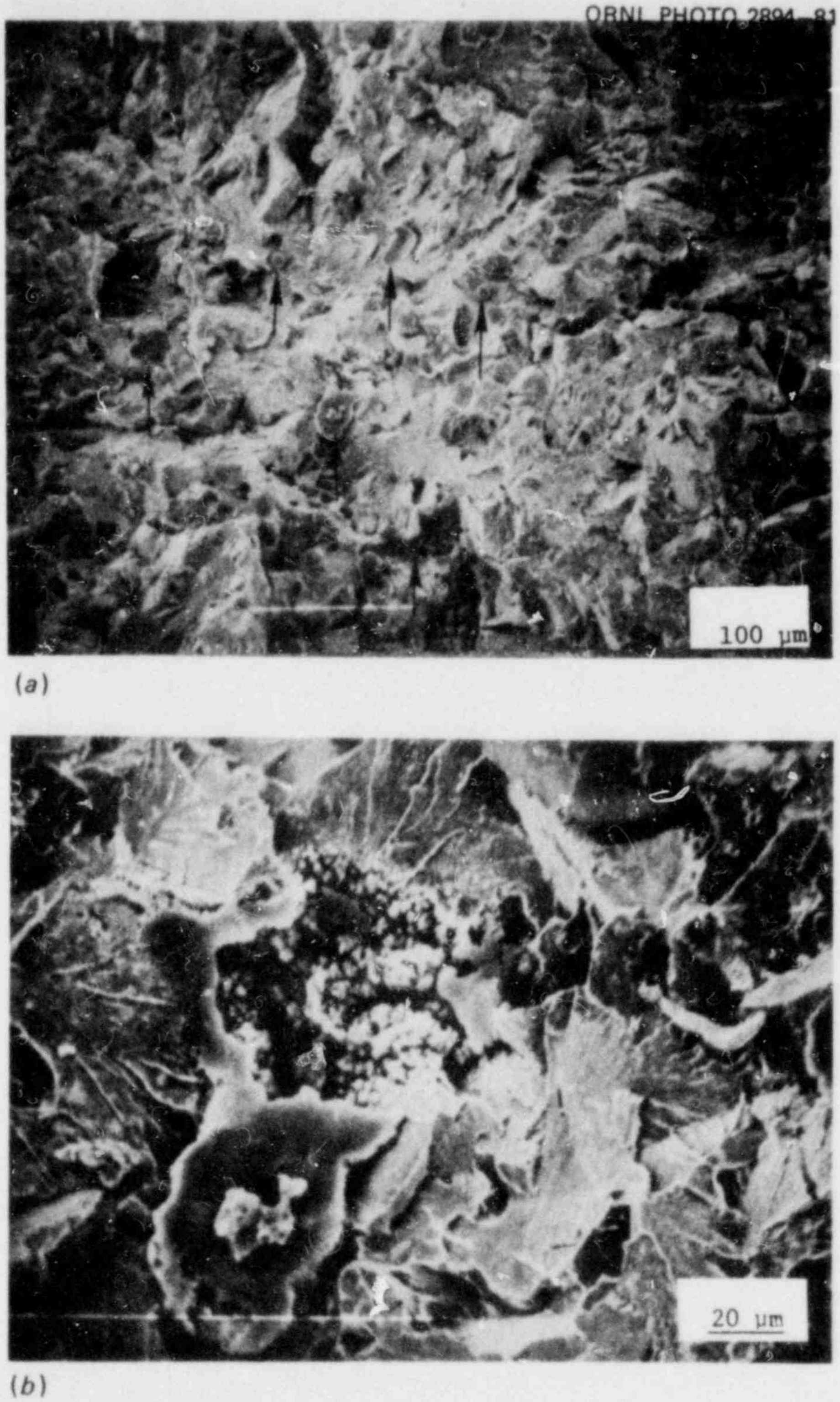

Fig. 2.19. Fracture-initiation site in specimen 2TP33. (a) Inclusions indicated by arrows, (b) suspected fracture-originating inclusion. Note hollow structure of the inclusion with porous mass.

parallel to the fracture surface, was unexpected. The crack planes in the 1T compact specimens were believed to have oriented in the thickness direction of the original steel shell; that is, the inclusions were expected to be oriented normal to the fracture surface. The reasons for the porous nature of the inclusions are also not understood. Clearly, nonmetallic inclusions in this steel should be characterized both in terms of their chemical composition as well as their size, shape, and orientation with respect to the crack plane.

In the initial fractography conducted on the three specimens of the group,[19] the cleavage initiation point was identified in specimen 2TP 32. A large grain with the cleavage plane parallel to the fracture surface and an inclusion in the vicinity were identified as the starting points for the cleavage fracture. Possibly both large grains and inclusions, either separately or in concert, can act as weak spots of the microstructure that trigger cleavage fracture. The inclusion sites are particularly vulnerable when they are hollow and act as stress concentrators. The relative frequency of the occurrence of these two types of defects can only be established by examining a large number of fracture toughness specimens. With continued improvements in both the skill and the techniques of fractography, hopefully a microstructural rationale can be provided for the statistical nature of the fracture toughness.

## 2.3 Investigation of Damping and of Cleavage-Fibrous Transition in Reactor-Grade Steel*

W. L. Fourney†

### 2.3.1 Introduction

The aim of the research program is to investigate in detail the transition region from cleavage to fibrous fracture and its effect on toughness determinations. A complete understanding of this phenomenon is extremely important in predicting fast fracture behavior in a structure.

Within the upper area of the transition temperature range, an observation can be made of the onset of rapid cleavage fracturing caused by increases of strain rate at a point of tearing instability. Likewise, in the lower portion of the transition range, one could expect that sudden fracture of regions of local weakness will cause a conversion from slow fibrous tearing to rapid cleavage prior to the instability point, as estimated in terms of R-curve considerations.

Studies of run arrest fracturing in crack arrest specimens have shown that tough late-breaking regions and a diffuse nature of the crack front occur to an increasing degree with increase of toughness and test temperature. Plausible ways exist in which behaviors of this kind can eliminate

---

*Work sponsored by HSST Program under UCC-ND Subcontract 7778 between UCC-ND and the University of Maryland.

†Department of Mechanical Engineering, University of Maryland, College Park.

conditions necessary for dominant cleavage fracturing. Thus, information from crack arrest research is related to cleavage-fibrous transition research in a natural way.

The expected flaw-probability influence on (1) scatter of toughness values in the lower regions of the transition temperature range, (2) conditions governing onset of cleavage in higher regions of the transition temperature range, and (3) the determination of a temperature $T_A$ high enough to exclude dominant cleavage fracturing are important aspects of transition behavior and are expected results from this research program.

The general topic of cleavage-fibrous transition is complex and difficult, but the importance of advancement of understanding in this area is widely recognized. In addition to research being conducted at Maryland, hopefully other research groups will become involved in cleavage-fibrous transition studies.

### 2.3.2 Research program

To obtain measurement data and a reasonable understanding of the aspects of the cleavage-fibrous transition that are of major importance, the following tasks make up the research program during 1980-1981:

A. tearing-instability fracture-toughness experiments,
B. investigation of statistical aspects of slow and rapid $K_{Ic}$ toughness values,
C. development of a mechanistic model for cleavage-fibrous behavior, and
D. coordination of related work performed at other interested laboratories.

Task A. The purposes of Task A are (1) to collect information illustrative of the role of tearing instability in causing the onset of dominant cleavage fracturing in the upper portion of the transition temperature range and (2) to explore the loss of tearing-instability control with reduction of testing temperature. Much of the information needed can be obtained through attracted interest at other laboratories or from samples previously tested elsewhere, but some testing will be conducted at Maryland. Tests to be conducted for a selected material would include

1. notch bend tests to determine the temperature $T_A$ high enough to exclude dominant cleavage fracturing,
2. 1T compact tests within the upper region of the transition range to establish the J-R curve for the material chosen,
3. 1T and 2T compact tests within the transition range to obtain cleavage fracture induced by J-R instability, and
4. 1T and 2T compact tests at lower temperature to demonstrate loss of J-R controlled instability.

Task B. The purposes of Task B are (1) to collect data from other laboratories that would be pertinent to this study, including review of previous studies of $K_{Ic}$ variations (Westinghouse, Alcoa, and NASA-Lewis) and (2) to use data from Task A to measure test result scatter at a selected temperature.

This work will be conducted in the most efficient manner taking account of such data and information as can be obtained from closely related research at other laboratories. Modifications of the test program, as necessary and appropriate, may occur.

Task C. Model development for the transition behavior would involve both photoelastic tests (with polymeric models and birefringent-coated steel samples) as well as 2-D dynamic calculations. Purposes are to

1. continue development and refinement of a theoretical model to describe the fibrous-cleavage transition taking into account weak-region (statistical) variations and quenching of cleavage by an increase in late-breaking ligaments;
2. continue trials of computer models of late-breaking ligaments, exploring the effects of locally weak or tough regions;
3. explore photoelastically the effect of local regions of tough or weak material in a specimen and the effect of nonuniform crack fronts on crack advance; and
4. obtain estimates of the closing forces resulting from late-breaking ligaments by fractography and by using photoelastic coatings on steel specimens.

Task D. As a topic, the cleavage-fibrous transition has been of interest to fracture researchers for a very long time. Recent findings suggest that a substantial advance in understanding, particularly of significant practical aspects, is possible. To proceed efficiently toward realization of these possibilities, the University of Maryland project is intended to provide (1) enough examples of clarification to attract wider interest in similar work, and (2) coordination and information exchange between those laboratories engaged in a cleavage-fibrous research effort. Task D is devoted to coordination and information exchange relative to enhanced understanding of cleavage-fibrous transition behaviors with particular emphasis on aspects of current practical importance to NRC.

### 2.3.3 Progress to date

Ductile-brittle transition studies. During this quarter, major progress was made in two areas: (1) testing of side-grooved double-width (SGDW) Charpy V-notch (CVN) specimens; and (2) topological characterization of fracture surfaces.

The results of standard CVN impact specimens were covered in a previous report.[32] Figure 2.20 shows the fracture surface appearances of those specimens. As evident from viewing the photograph, the occurrence of shear lips interferes with the clear determination of cleavage dominant fracture. The SGDW specimens were machined from a second beam of the three-point bend specimens provided by Del Research Corporation.[32] Geometry and dimensions of a SGDW specimen are shown in Fig. 2.21. An impact-testing machine was modified to accept the double-width specimens. Three SGDW specimens were tested at elevated temperatures, and results of Charpy impact energy are compared with previous results obtained for standard specimens in Fig. 2.22. Fracture surfaces for the wide specimens are shown in Fig. 2.23.

ORNL PHOTO 2895–81

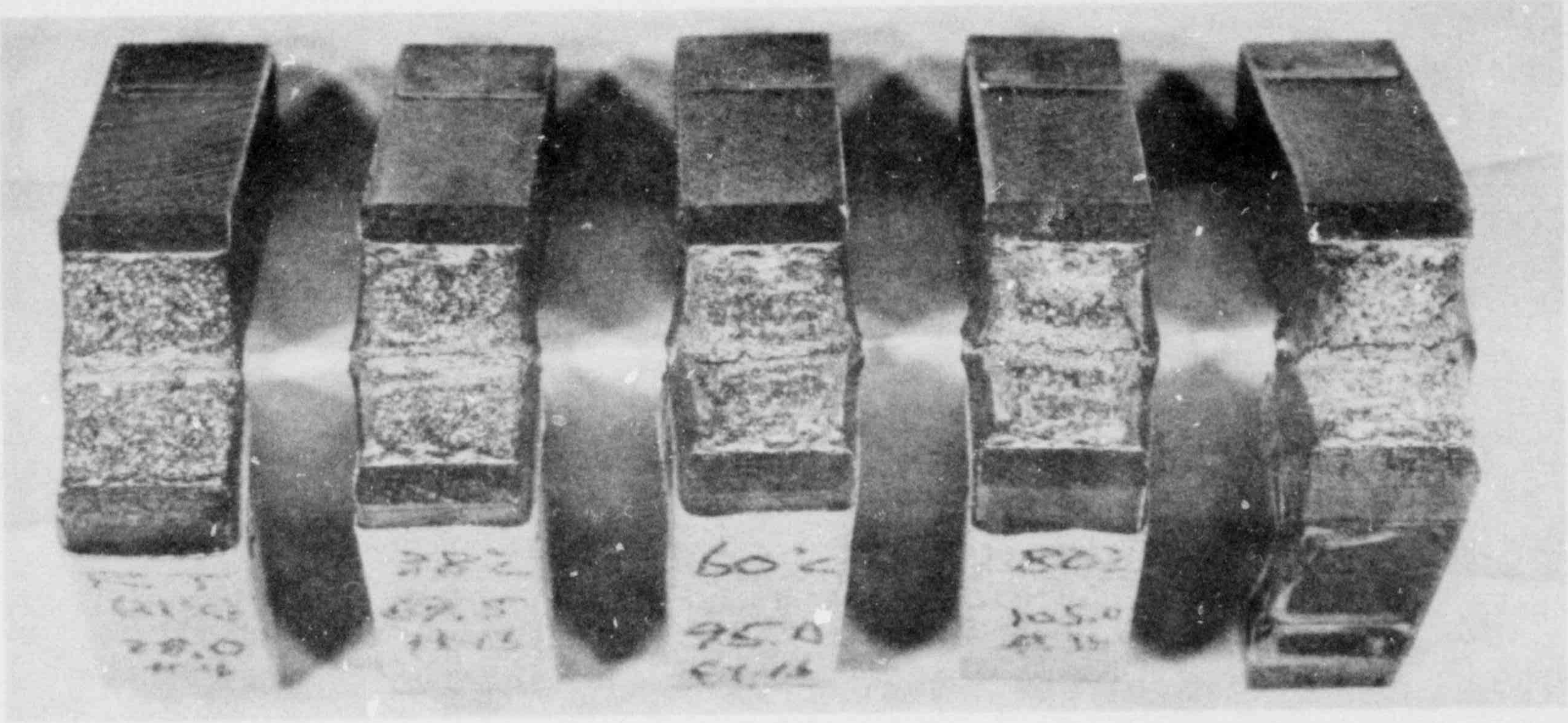

Fig. 2.20. Fracture surface appearances of standard CVN specimens of A36.

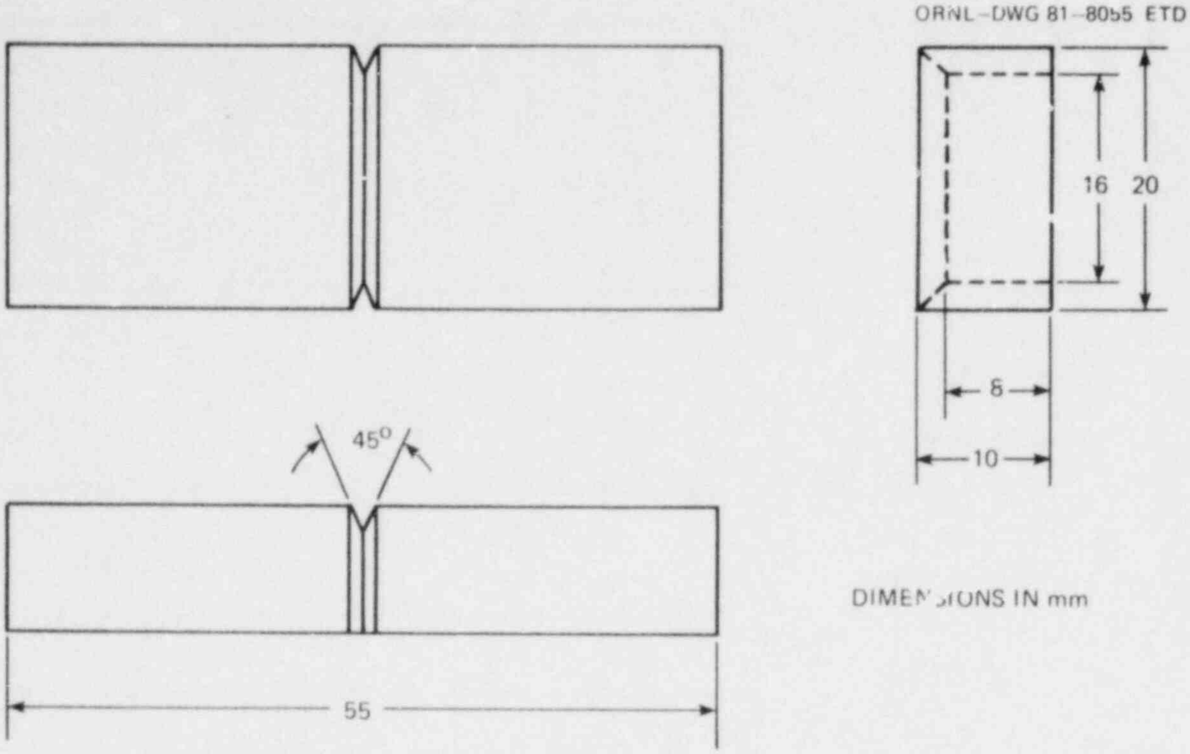

Fig. 2.21. Geometry and dimensions of SGDW specimen.

Close examination of the fracture surfaces of the SGDW specimens indicates that there was an effect of constraint in cleavage fracture formation obtained earlier for the standard specimens. A comparison of fracture surfaces of standard CVN specimens and of SGDW specimens shows that the surface features of SGDW specimens correspond to those of standard specimens tested 10 to 20 K lower in temperature.

The plot of impact energy vs test temperature (Fig. 2.22) also shows a steeper slope for the wider specimens than for standard CVN specimens.

Because testing to date has not established a temperature at which cleavage fracture does not occur in the SGDW specimens, additional specimens are being made and will be tested at higher temperatures (90, 95, 100, and 105°C).

In a previous report, preliminary results of topological characterization of a fracture surface were covered.[32] An extension of those results is presented here.

Topological characterizations were made with a parallax bar in conjunction with stereophotographs. A height measurement of points on the fracture surface was made relative to a reference plane (such as an initial fatigue crack surface in the photograph). The following equation was used to compute the actual height difference:

$$\Delta h = \frac{\Delta m}{2M \sin(\theta/2)} , \tag{2.27}$$

ORNL-DWG 81-8056 ETD

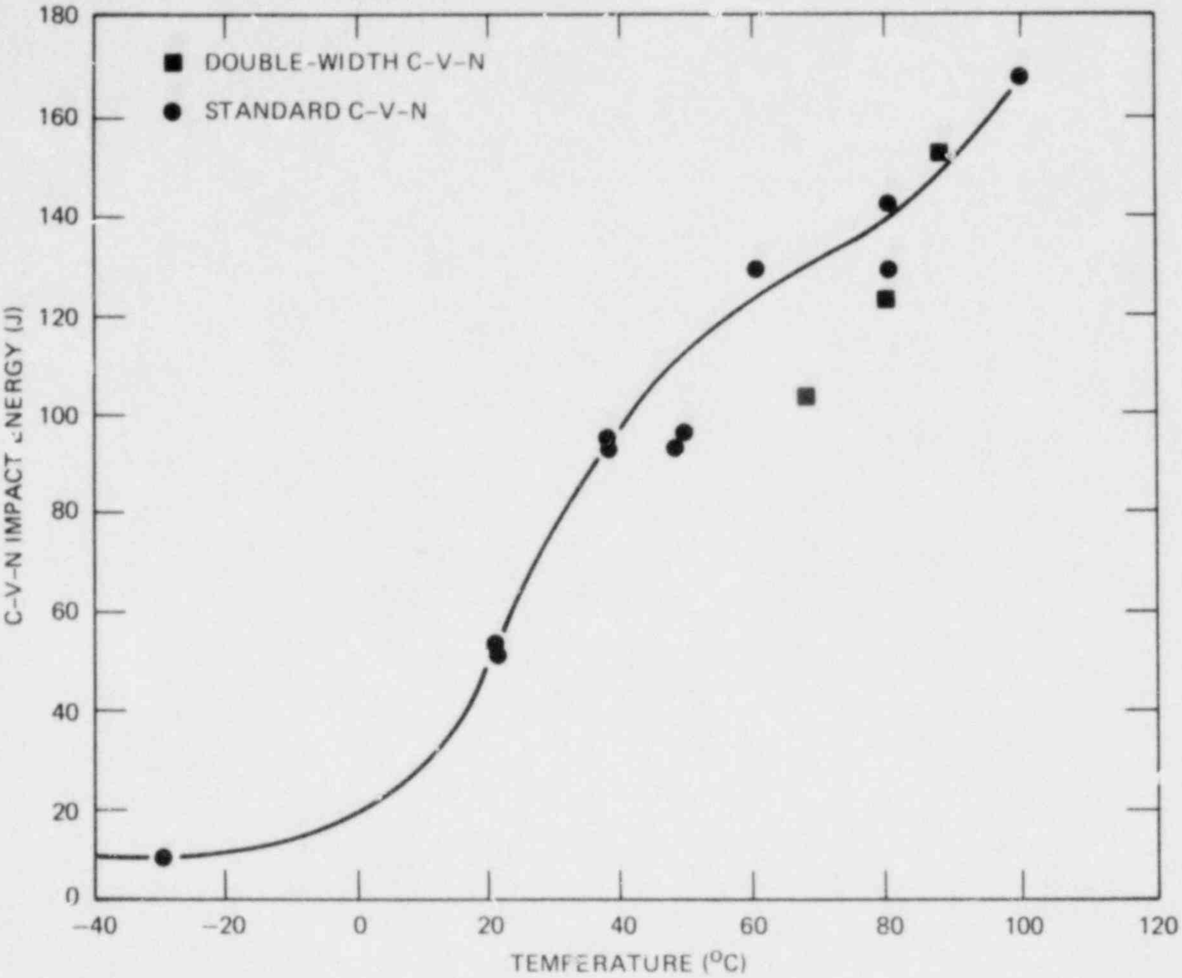

Fig. 2.22. CVN impact energy vs test temperature.

where

Δh = height elevation,
Δm = difference in parallax bar micrometer reading,
M = magnification of photograph,
θ = rotational angle of the specimen holder between a pair of stereophotographs.

Figures 2.24 and 2.25 show stereopairs of photographs taken from the matching site of top and bottom fracture surfaces. The area shown is the end of a fatigue crack region and the beginning of a fibrous fracture zone under monotonically increasing load. The specimen selected was an A533B compact specimen tested at 59°C. Height measurements were made along the three lines shown in Fig. 2.24. The upper and lower surface contours are shown in Figs. 2.26 through 2.28 for lines A, B, and C, respectively. To assess the deformation and fracture processes, the surface contours from

ORNL PHOTO 2896–81

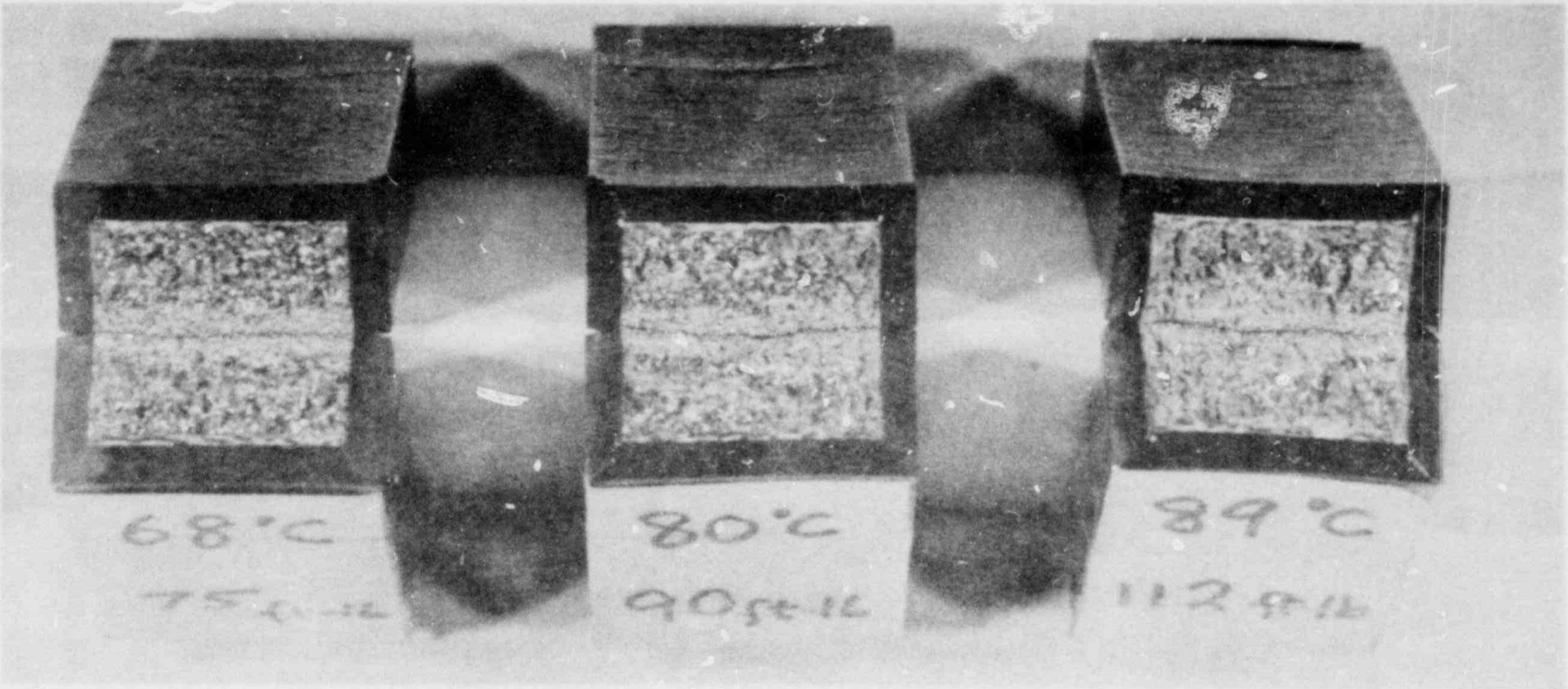

Fig. 2.23. Fracture surface appearances of SGDW specimens.

ORNL PHOTO 2897-81

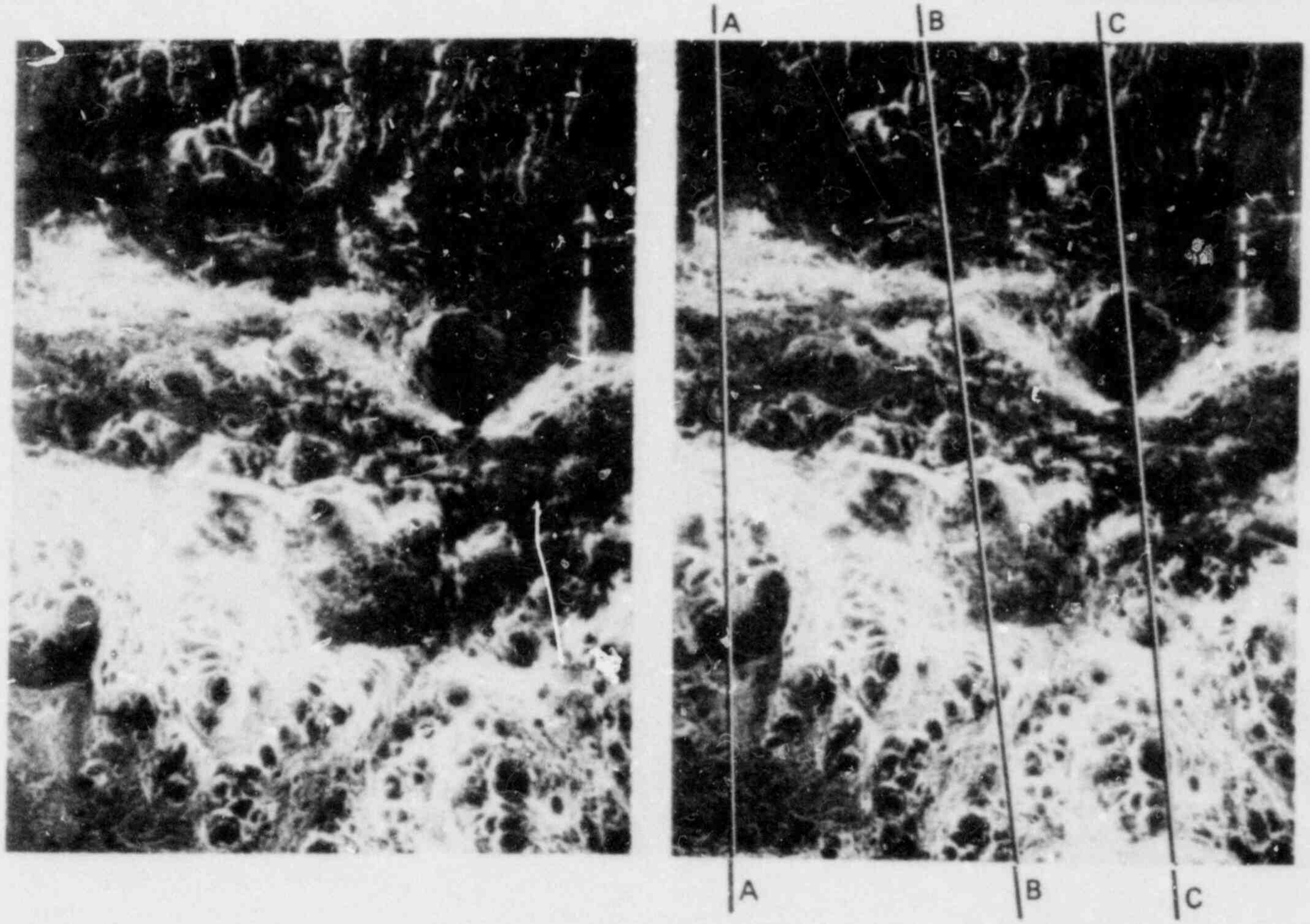

Fig. 2.24. A pair of stereophotographs of upper fracture surface U.

ORNL PHOTO 2898--81

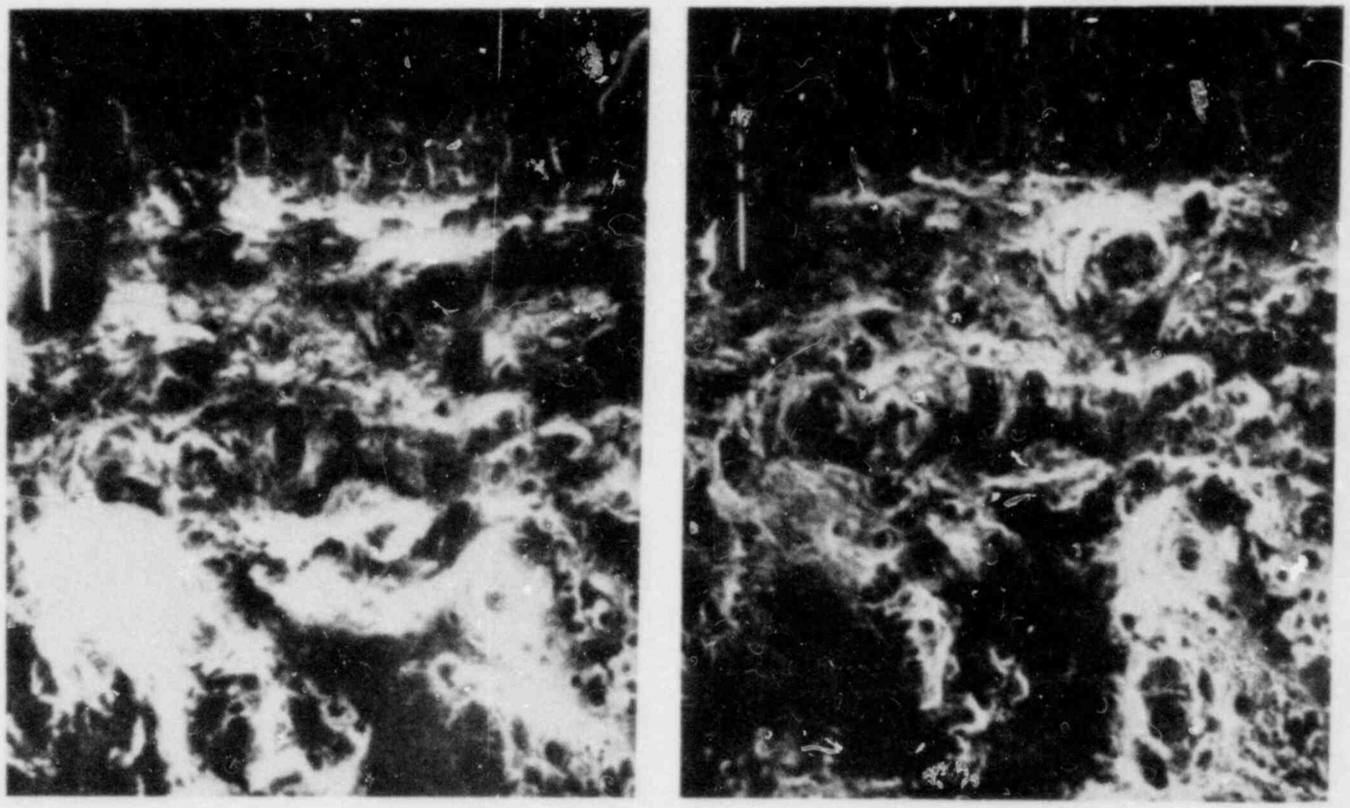

Fig. 2.25. A pair of stereophotographs of lower fracture surface L.

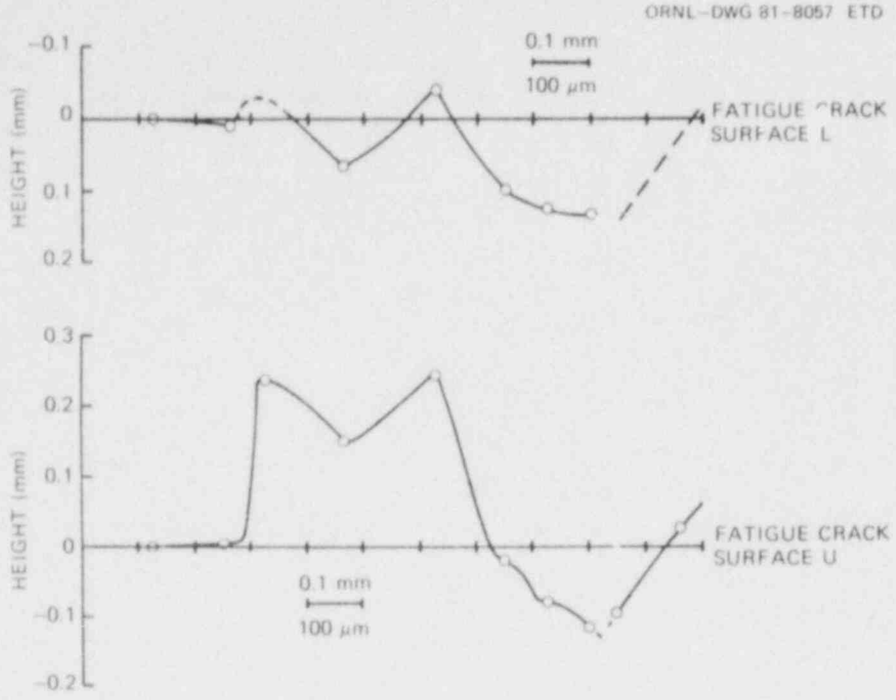

Fig. 2.26. Surface contours of fracture surfaces L and U along line A.

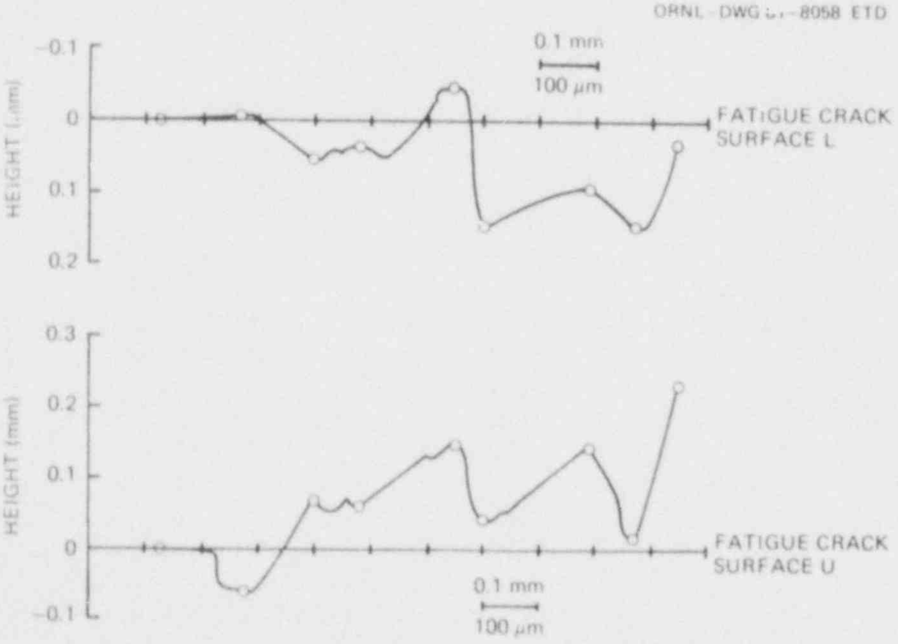

Fig. 2.27. Surface contours of fracture surfaces L and U along line B.

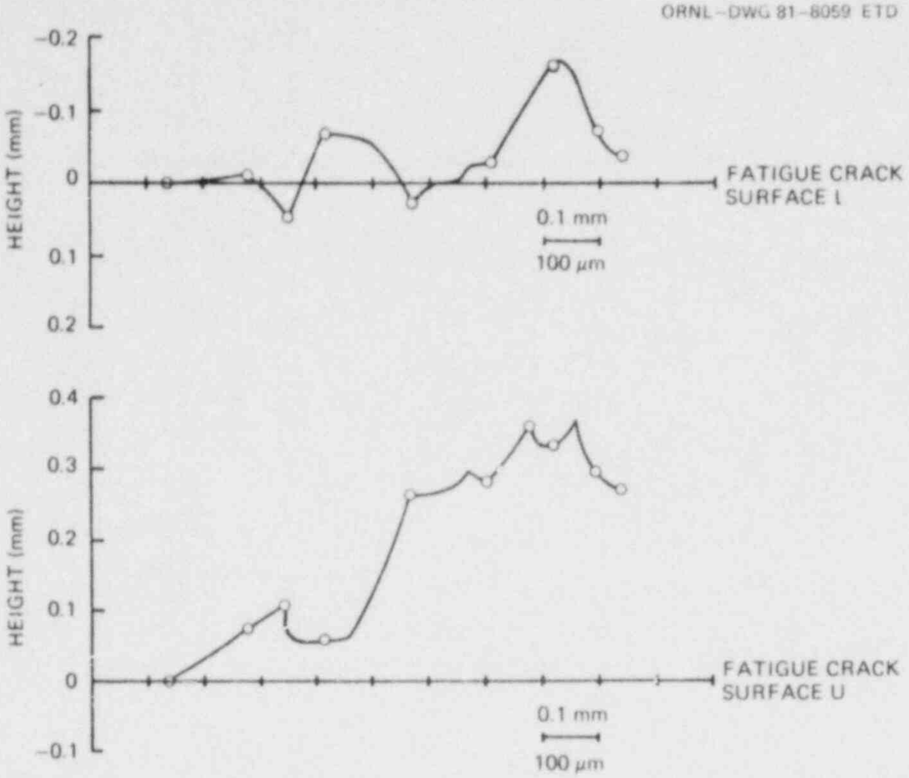

Fig. 2.28. Surface contours of fracture surfaces L and U along line C.

the top and the bottom surfaces were brought together until the segments of the surface curves contacted each other. The results are shown in Figs. 2.29 through 2.31.

Figure 2.29 shows that the fatigue-crack surface separation distance was about 0.22 mm. Furthermore, an inclusion of 0.22 mm in diameter, which existed about 0.6 mm away from the fatigue crack tip, fractured almost immediately as the fatigue crack opened up. This is evidenced by the fact that the separation distance between top and bottom surfaces at the inclusion is identical to the separation distance at the fatigue fracture surfaces (marked as distance d in Fig. 2.29). The area between the fatigue fracture zone and inclusion plastically deformed as if it was an unbroken ligament before it failed in shear.

Figure 2.30 shows similar results: the fatigue fracture surface separation distance was about 0.23 mm. Along line B, a crack propagated from the end of the fatigue crack tip without jumping, although the crack path was irregular.

Figure 2.31 indicates that the fatigue fracture surface separation was 0.29 mm. An inclusion of ~0.1 mm in diameter that existed 0.2 mm ahead of the fatigue crack tip separated first. A void formation can be seen at 0.6 mm ahead of the fatigue crack tip. The contours also indicate that shear fracture along a conical plane was induced from the void formed. This fracture moved back toward the fatigue crack tip and connected with the opening produced by the inclusion.

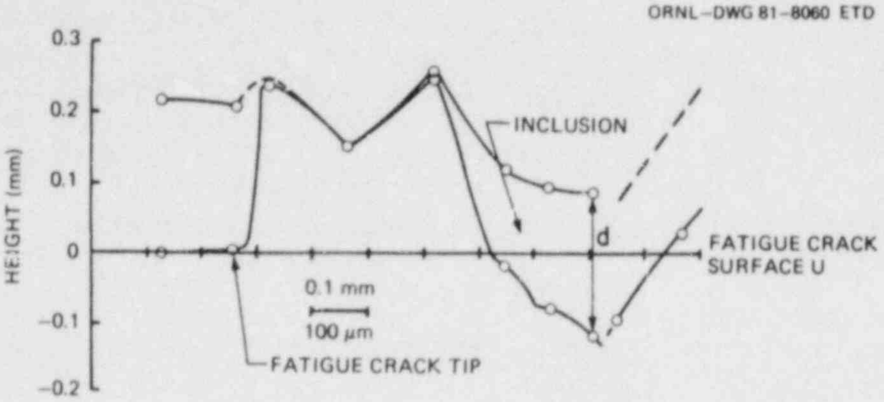

Fig. 2.29. Deformation of surfaces along line A.

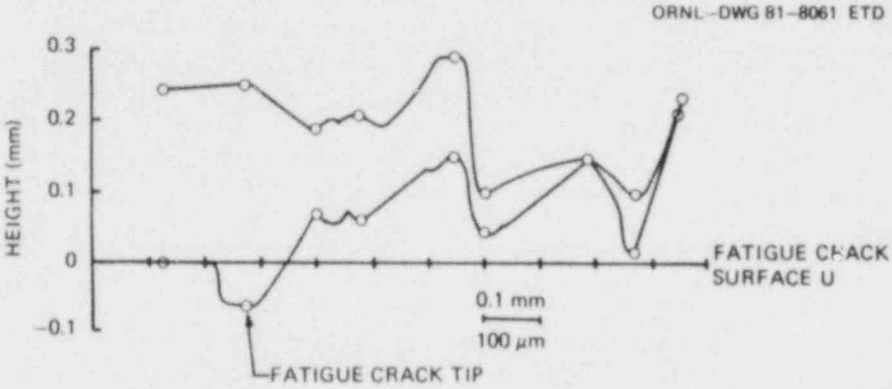

Fig. 2.30. Deformation of surfaces along line B.

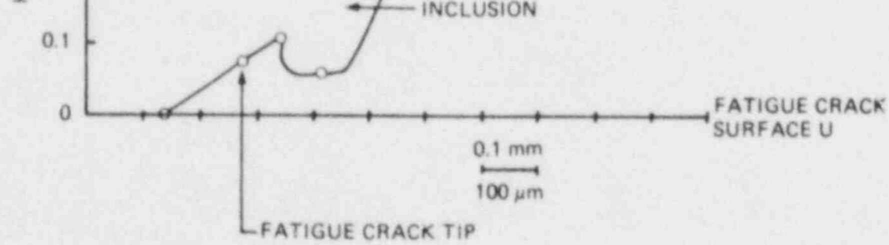

Fig. 2.31. Deformation of surfaces along line C.

Examination of Figs. 2.29 through 2.31 indicates that the fatigue surface separation along lines A, B, and C was 0.22, 0.23, and 0.29 mm, respectively. These separation distances can be interpreted as the crack-tip-opening displacement and used in computation of J values ($J = \delta\sigma_{ys}$). With a median value of 0.23 mm as crack-tip-opening stretch and a yield strength of 495 MPa for an A533B, a J value of 114 kJ/m$^2$ was obtained. This J value can be converted to K by the equation $K^2 = JE$. The value of K thus obtained was 151 MPa$\sqrt{m}$, which appeared to be quite reasonable.

Anotner trial of topological characterization was made on the fracture surface shown in Fig. 2.32. This fracture surface was from an A36 Steel specimen, and the test temperature was 38°C. The appearance of the fracture surface represents cleavage surfaces separated by fibrous fracture areas. The results of topological measurement along the line PQ are shown in Fig. 2.33 in which three cleavage planes, A, B, and C, are indicated. Two cleavage planes, B and C, are parallel, indicating that these cleavage planes are in the same grain. Cleavage plane A, on the other hand, shows a different slope, indicating that it belongs to a different grain from that of planes B and C. Thus, the fibrous fracture surfaces between the cleavage planes A and B and between B and C may represent grain boundaries.

The fracture surface shown in Fig. 2.34 is a different area from the same specimen. A stereomicroscopic examination of the cleavage fracture

ORNL PHOTO 2899–81

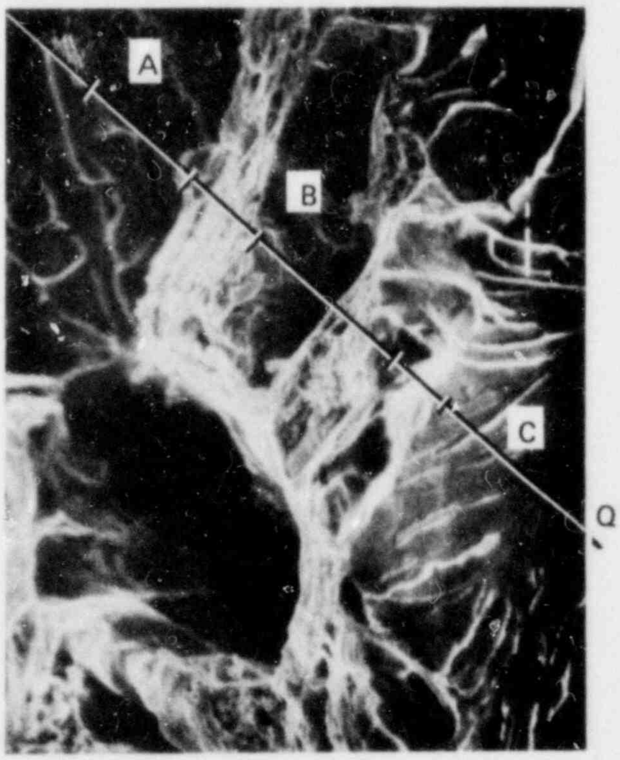

Fig. 2.32. Fibrous fracture area in cleavage dominant region.

ORNL–DWG 81–8063 ETD

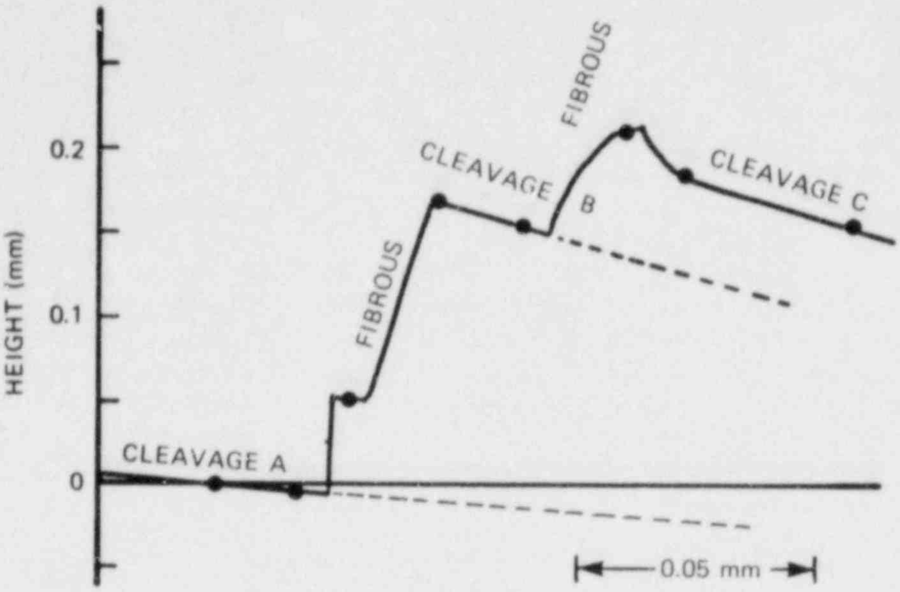

Fig. 2.33. Fracture surface contour along line PQ.

ORNL PHOTO 2900–81

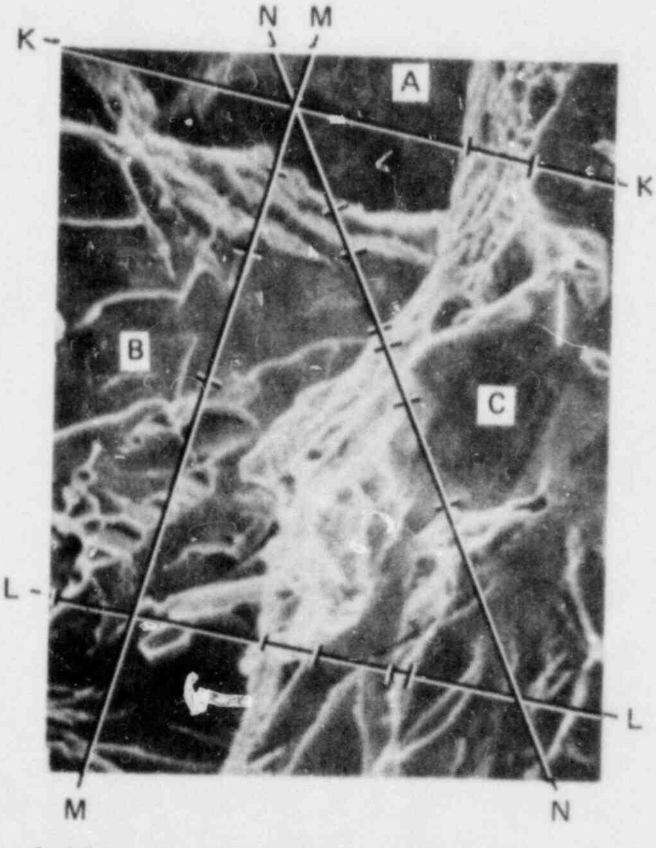

Fig. 2.34. Cleavage fracture dominant region.

revealed that it occurred at three different levels accompanied by cleavage undercuttings; that is, the cleavage fracture in plane B spread underneath plane C. The crack propagation directions in the two cleavage planes B and C are not consistent (Fig. 2.34), which indicates that the cleavage fracture process is self-stimulating.

The height measurement was made along lines K, L, M, and N, and the results are shown in Fig. 2.35. Apparently, the cleavage planes B and C are parallel, indicating that planes B and C may belong to the same grain. The fibrous fracture area between cleavage planes B and C is the result of cleavage undercutting and final shear failure of an unbroken ligament.

From the examples presented, the topological characterization of fracture surfaces apparently provides valuable information that is helpful in the analysis of fracture mechanisms. This approach will be used more extensively to study fibrous-cleavage transition work in the future.

Computational effort. The finite-element computer code developed at the University of Maryland has been used in the past to predict crack propagation and arrest in laboratory specimens.[33] The code SAMCR was shown to yield good correlation with observed crack jump distances as well

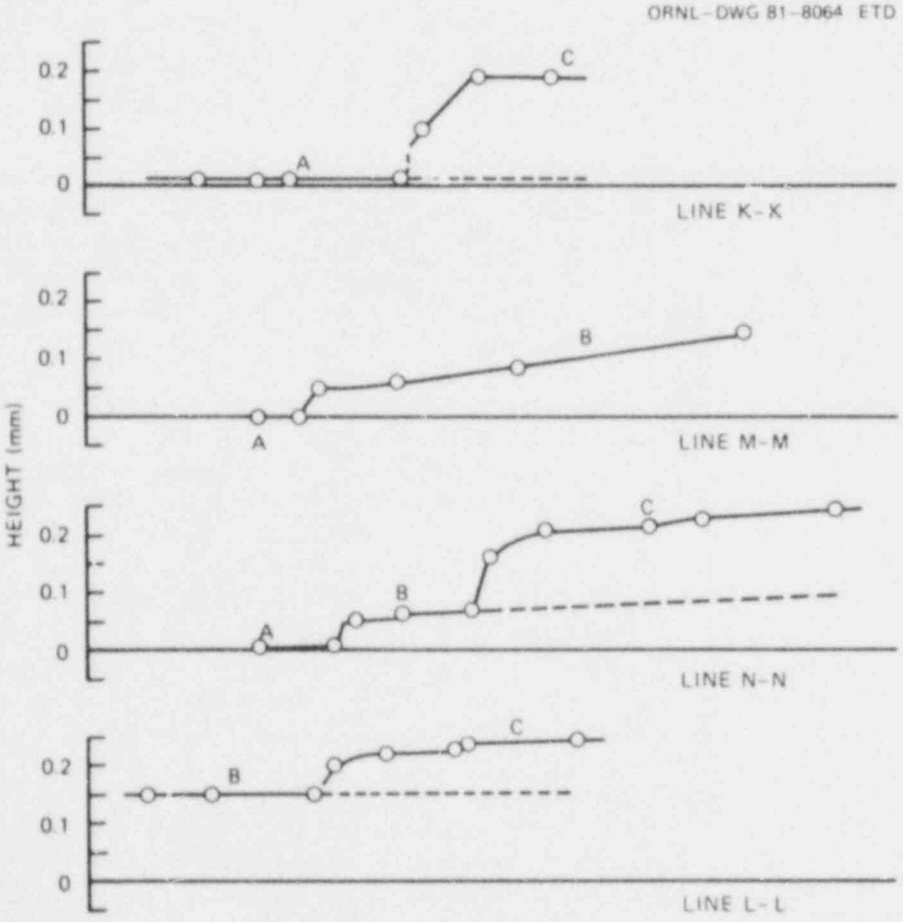

Fig. 2.35. Fracture surface contours along lines K, L, M, and N.

as instantaneous values of stress intensity for compact tension specimens of various sizes that were made of birefringent plastics. Valid results for crack jump distances were also obtained for standard and subsized compact samples made from 4340 steel. Computations have recently been completed with the code to predict crack jumps that occurred in the thermal shock experiment TSE-5 conducted at ORNL.

The biggest problems encountered in the attempts to perform the dynamic computer analyses were the lack of well-defined relationships for stress intensity K as a function of crack velocity $\dot{a}$ and $K_{Ia}$ as a function of crack-tip temperature T for the A508 material of the test cylinder. The SAMCR (Sam Crack) uses the $\dot{a}$-K relationship together with the computed crack-tip stress intensity to establish the incremental crack extension $\Delta a$ that will occur in any given time step $\Delta t$ during the computation.[33] Therefore, if any degree of confidence is to be placed in the predicted crack jumps that are obtained, the $\dot{a}$-K relationship must be known fairly accurately.

Of the three jumps that occurred in TSE-5, jump 2 (from $a/w = 0.2$ to $a/w = 0.63$) was selected for computational analysis because this best represented a dynamic crack-propagation event. The value of K at $\dot{a} = 0$ was taken to be the same as $K_{Ia}$. The temperature T varied through the wall of the cylinder, and thus the arrest toughness $K_{Ia}$ also varied with crack-tip position. The relationship for stress intensity as a function of temperature and crack velocity was assumed to be given by

$$K(\dot{a},T) = K_{Ia}(T) + \Delta K(\dot{a}) \; . \tag{2.28}$$

Based on work reported by BCL,[34,35] this relationship was selected for consistency with BCL, who previously used a finite-difference code to predict the crack jump events in TSE-5. No actual measurements of this relationship are available for steels similar to A508.

The relationship between $\Delta K$ and $\dot{a}$ (Fig. 2.36) was also taken from the Battelle work and represents the relationship that they used at room temperature.

A relationship for $K_{Ia}$ and temperature in the range of interest (−2.5 to 82°C) proved to be somewhat more of a problem. The posttest analyses of TSE-5 and laboratory tests at BCL[34] provide a total of eight data points for $K_{Ia}$ at different temperatures (Fig. 2.37). Notice that all of the data correspond to essentially two temperatures only and display considerable scatter. Two straight lines were passed through the data. Line 1 represents a least-squares fit to all of the data points, and line 2 is a least-squares fit through the five data points generated by BCL. The fact that the $K_{Ia}$ data were concentrated at two temperatures made obtaining other than a straight-line fit through the data points difficult. A third relationship between $K_{Ia}$ and T, with some curvature, was constructed in the following manner.

The lower bound of the $K_{Ic}$ data for TSE-5 (Fig. 4 3 in Ref. 36) was compared with the posttest-adjusted $K_{Ic}$ and $K_{Ia}$ curves for TSE-5A (Fig. 13 in Ref. 37). A parabolic $K_{Ia}$ vs T relationship for TSE-5 was formulated using the other three curves as a guide. The set of four curves is shown in Fig. 2.38. The $K_{Ia}$ curve for TSE-5 was constructed by a temperature shift of the $K_{Ic}$ curve for TSE-5; the shift amount corresponded to that

ORNL-DWG 81-8065 ETD

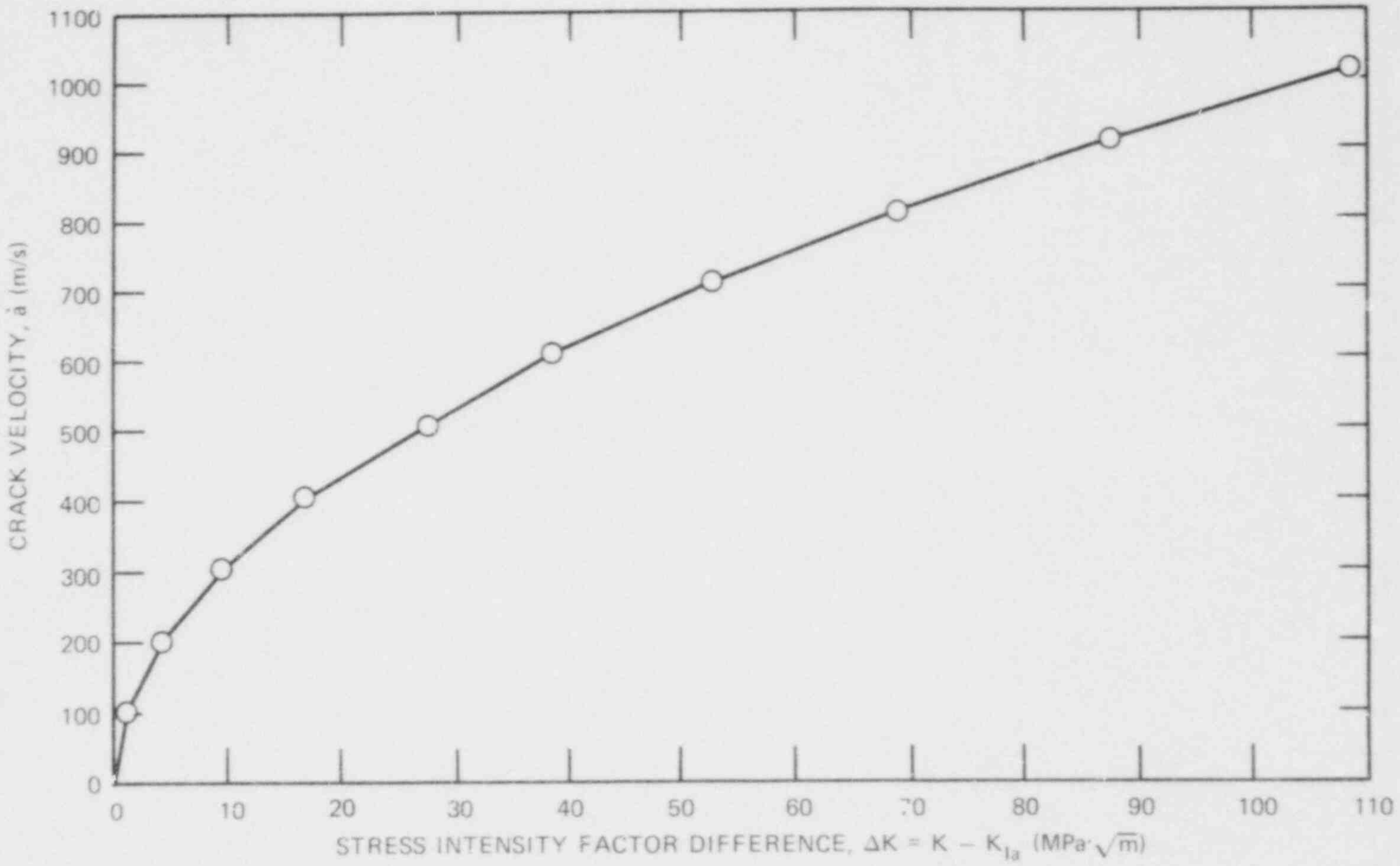

Fig. 2.36. Assumed relationship between crack velocity a and stress intensity factor difference ΔK.

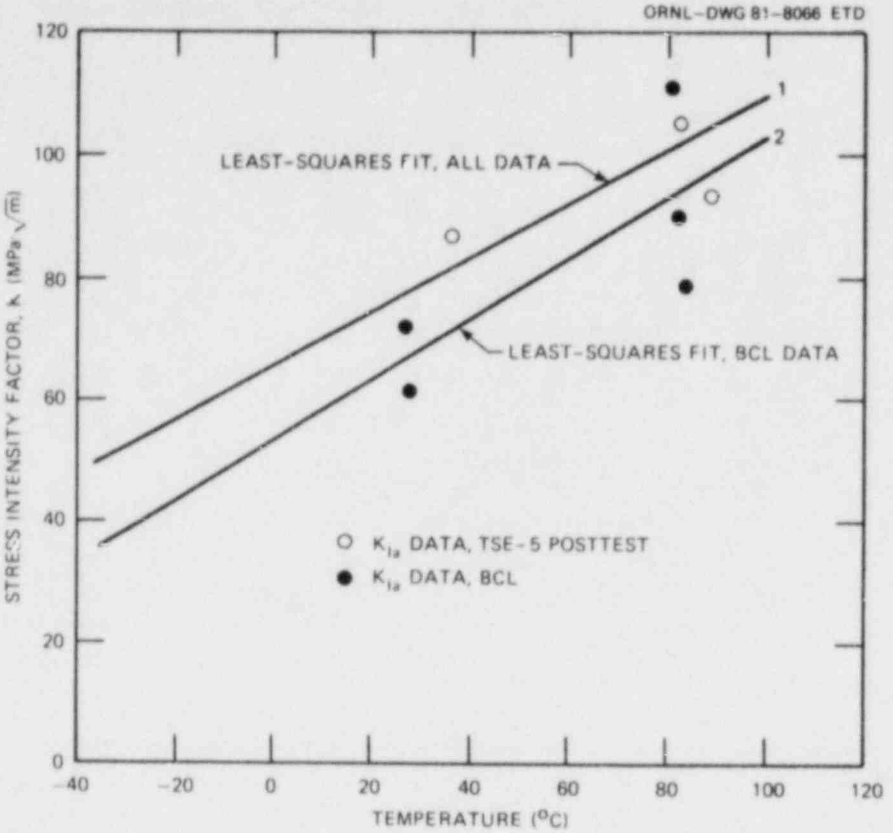

Fig. 2.37. Two possible straight-line relationships between $K_{Ia}$ and crack-tip temperature T.

observed between the two corresponding curves in TSE-5A. This temperature shift was computed for each stress-intensity level. Notice that this curve constructed in this manner (labeled curve 3 in Fig. 2.38) represents a fair estimate of a lower-bound curve for the available data for TSE-5.

A total of three possible $K_{Ia}$ vs T relations for TSE-5 were thus obtained, corresponding to straight lines 1 and 2 in Fig. 2.37 and curve 3 in Fig. 2.38. These three curves along with the $K_{Ia}$ data points are replotted in Fig. 2.39. Figure 2.40 compares the static finite-element values[34] of $K_I$ for the time and crack-depth range corresponding to crack jump 2 with the crack arrest toughness values corresponding to the temperatures existing at each crack depth at the same time, according to the three $K_{Ia}$ vs T curves shown in Fig. 2.39. Figure 2.40 also shows the experimentally observed initiation and arrest points, $a_0$ and $a_f$, for comparison. Note that all three relations would predict arrest (based on a purely static analysis) at a crack-tip position that is deeper in the cylinder wall than actually obtained.

Each of these three $K_{Ia}$ vs T relations was used as an input to SAMCR together with the $\dot{a}$ vs $\Delta K$ relation indicated earlier. The dynamic results for K vs crack-tip position a are shown in Figs. 2.41 through 2.43 (curves 1 through 3, respectively). Also shown on each figure, for comparison purposes, are the static K vs a and the $K_{Ia}$ vs a relations for that particular case. Note that in Figs. 2.41 and 2.43, the computer computations

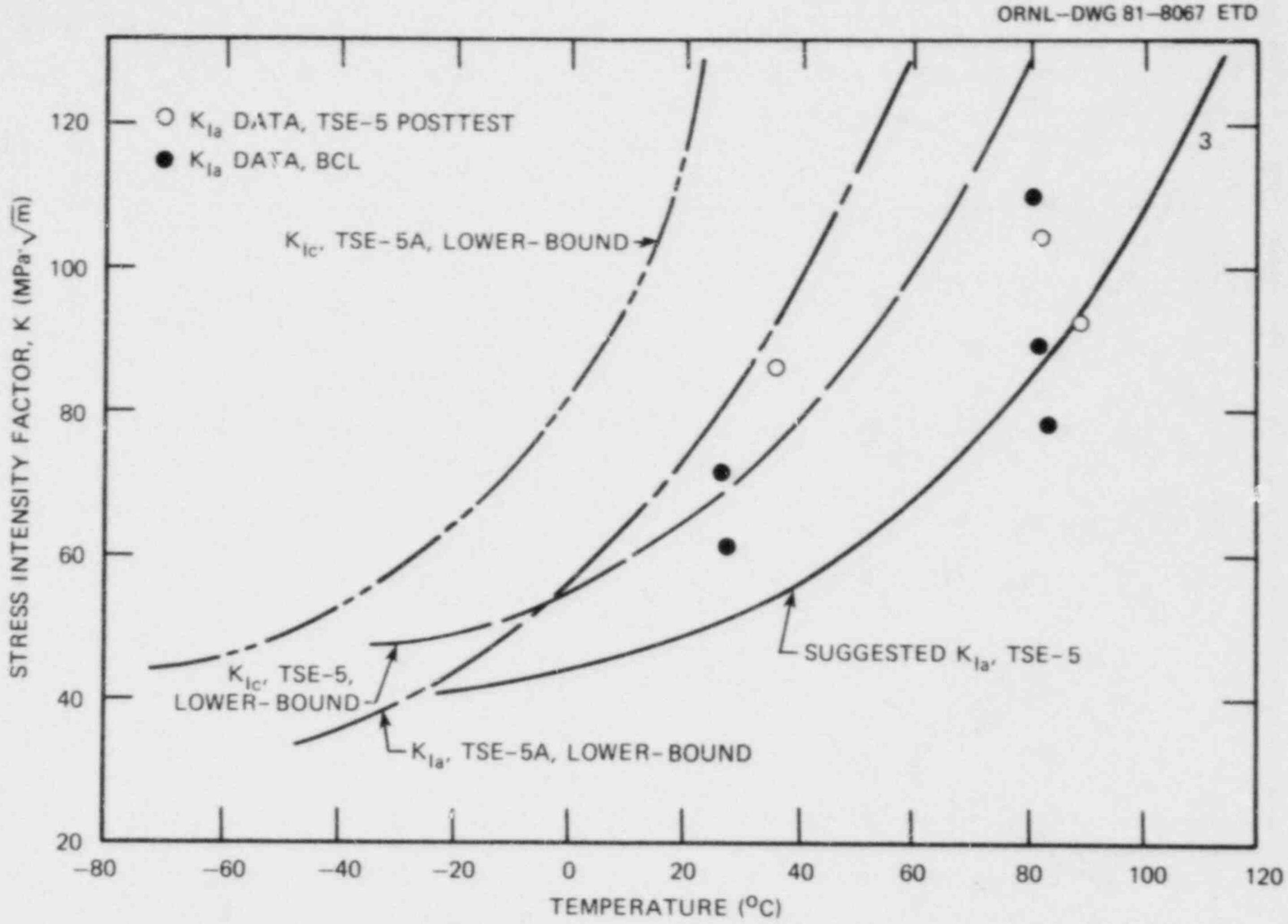

Fig. 2.38. Suggested $K_{Ia}$ vs T relationship for TSE-5, the established $K_{Ic}$ and $K_{Ia}$ curves for TSE-5A, and the $K_{Ic}$ curve for TSE-5.

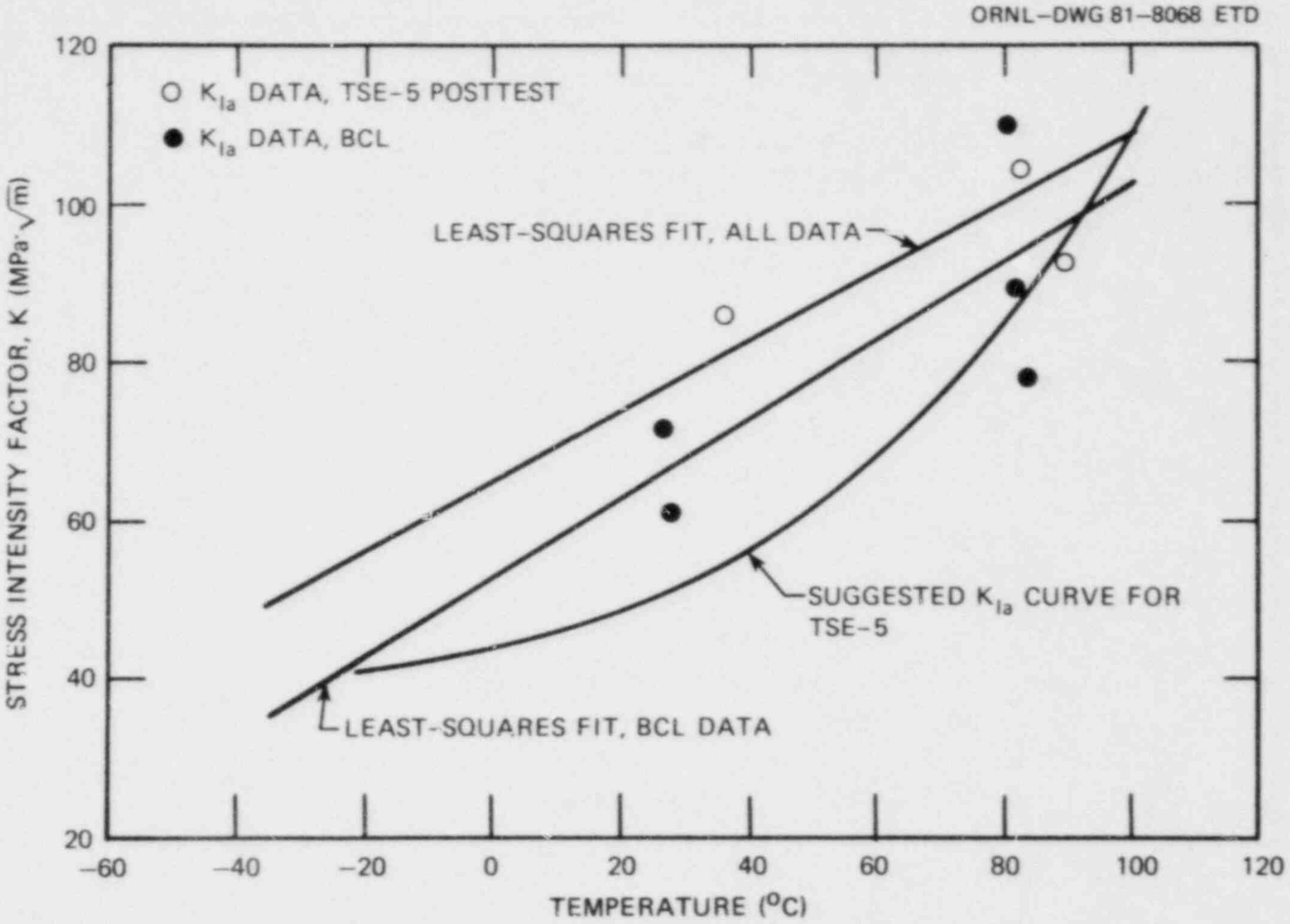

Fig. 2.39. Three relationships between $K_{Ia}$ and crack-tip temperature T that were investigated in the dynamic analysis of TSE-5.

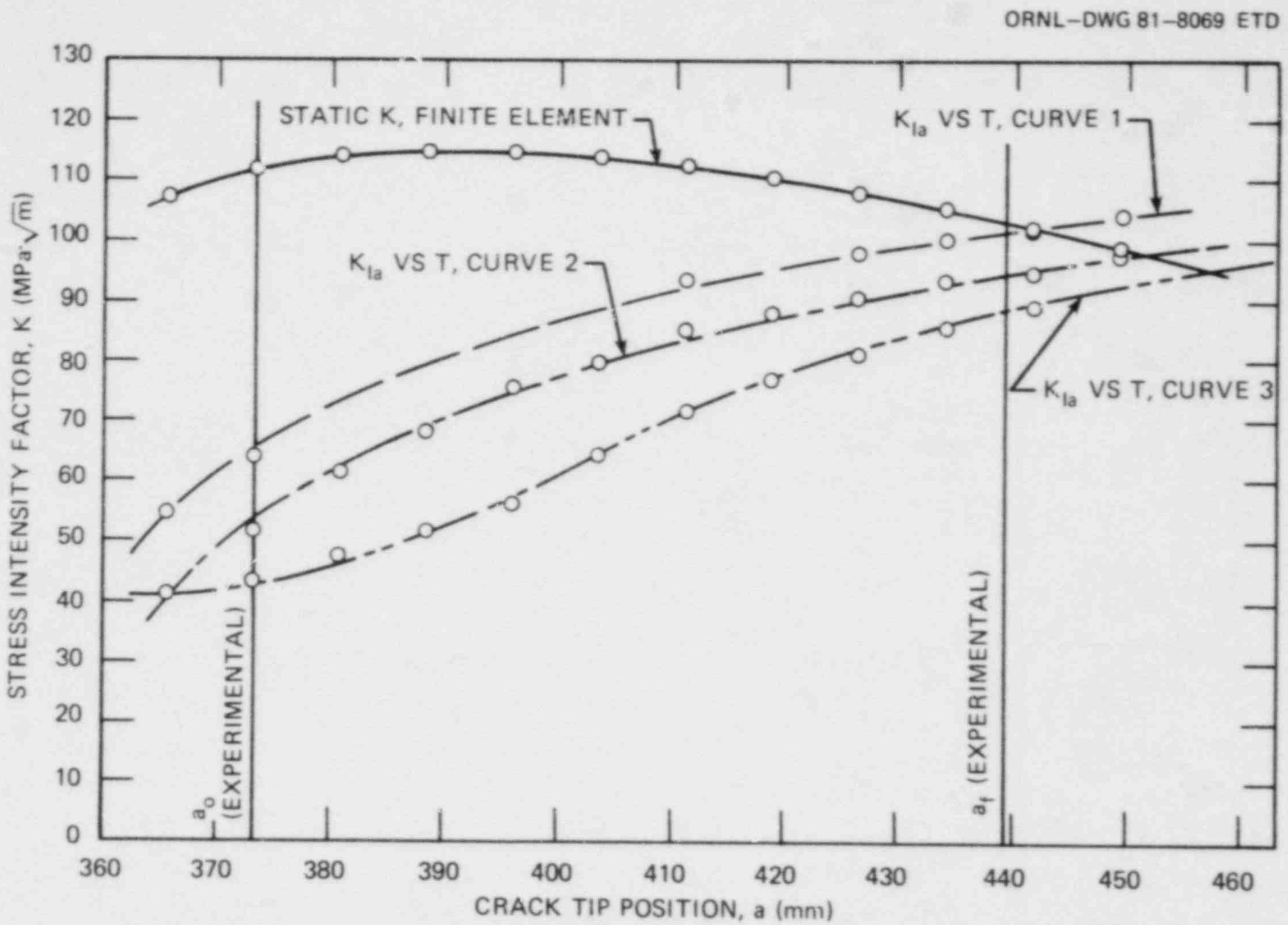

Fig. 2.40. Stress-intensity factor as a function of crack-tip position from static finite-element analysis and crack arrest toughness values by the three relationships investigated, corresponding to the temperatures at each crack depth at the time of crack jump 2 in TSE-5.

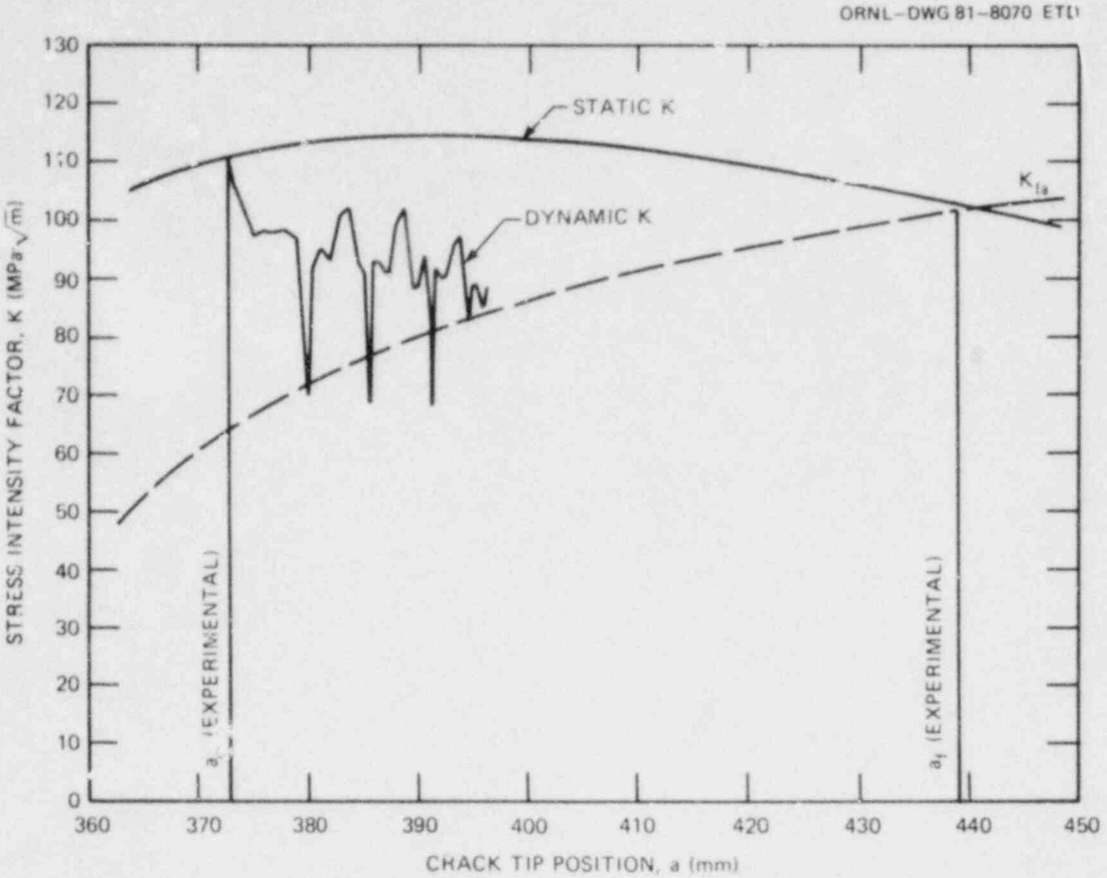

Fig. 2.41. Static and dynamic K-values as a function of crack-tip position using curve 1 to define $K_{Ia}$ as a function of T.

had not yet predicted a final arrest at the time that computations were halted. In the case of Fig. 2.42, a final arrest point was reached.

Figure 2.44 shows the instantaneous crack-tip position as a function of time, plotted every 5 Δts, as obtained from the use of the three different $K_{Ia}$ vs T relations. Notice that for Cases 1 and 3, the predicted crack extension history has been extended (using dashed lines) to indicate the anticipated arrest points, based on the results obtained for Case 2, where a computer prediction of final arrest was obtained before the end of the computations.

The results obtained demonstrate the extreme sensitivity of SAMCR to the specified $K_{Ia}$ vs T relationship. Because no better data are available for the TSE-5 material, at this time to obtain more accurate relationships than the ones used is not possible.

The result from SAMCR with the lower-bound $K_{Ia}$ curve that was formulated predicted the crack jump length quite accurately. However, anticipations were that SAMCR would overpredict the jump length because the program has no damping mechanism specifically incorporated into it.

The effect of ΔK vs $\dot{a}$ on predicted jump distances has not been examined but is of equal importance.

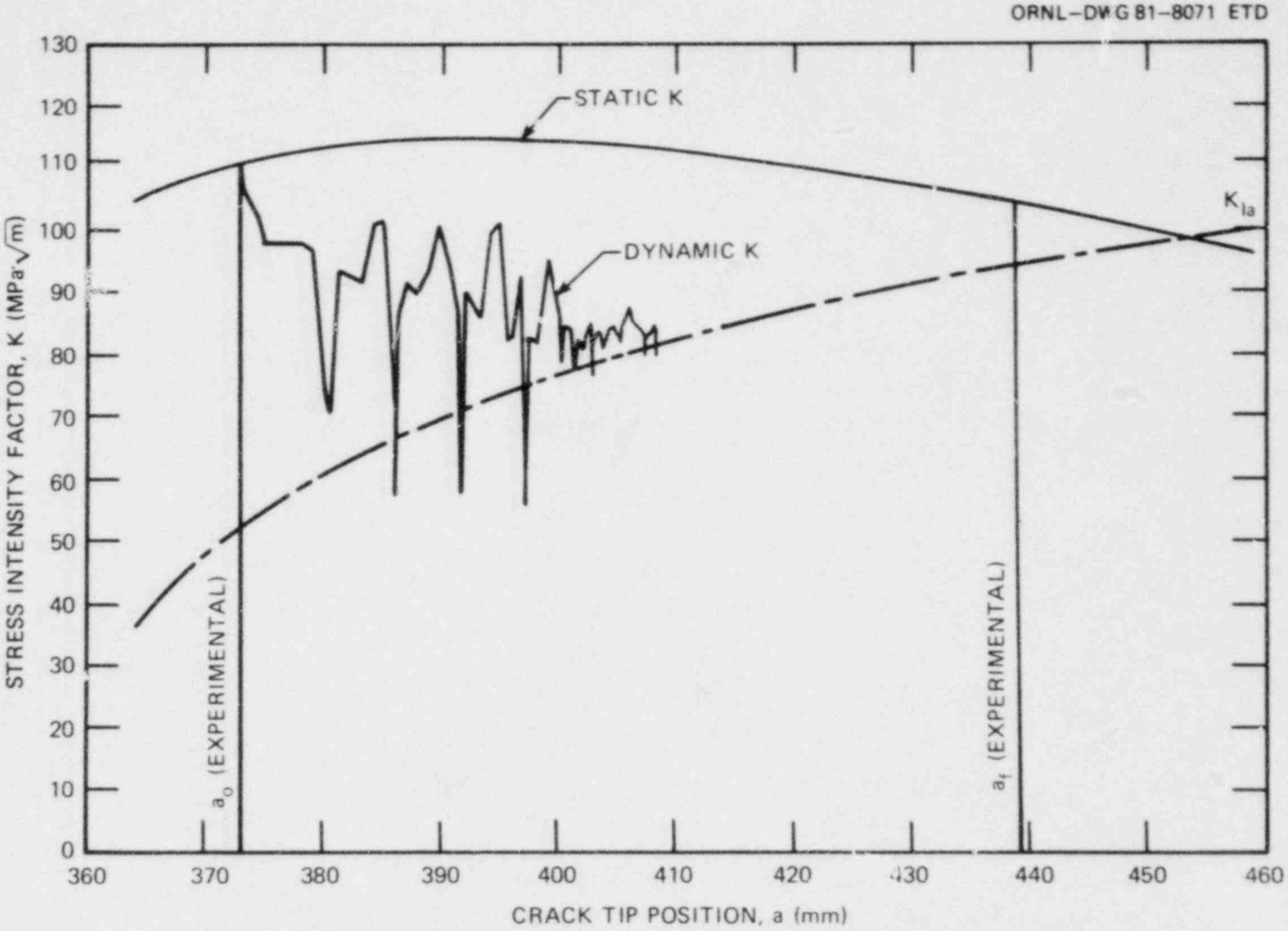

Fig. 2.42. Static and dynamic K-values as a function of crack-tip position using curve 2 to define $K_{Ia}$ as a function of T.

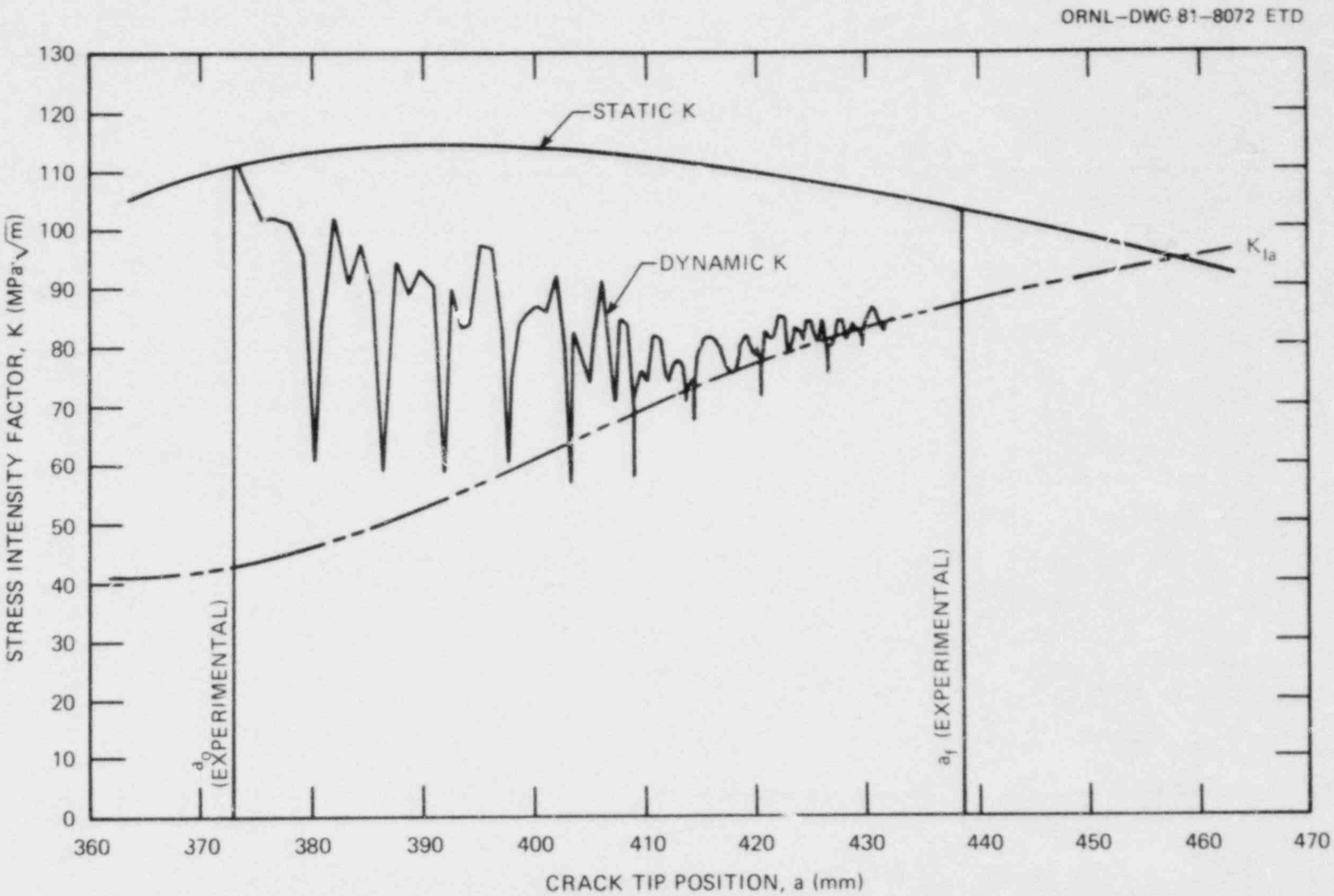

Fig. 2.43. Static and dynamic K-values as a function of crack-tip position using curve 3 to define $K_{Ia}$ as a function of T.

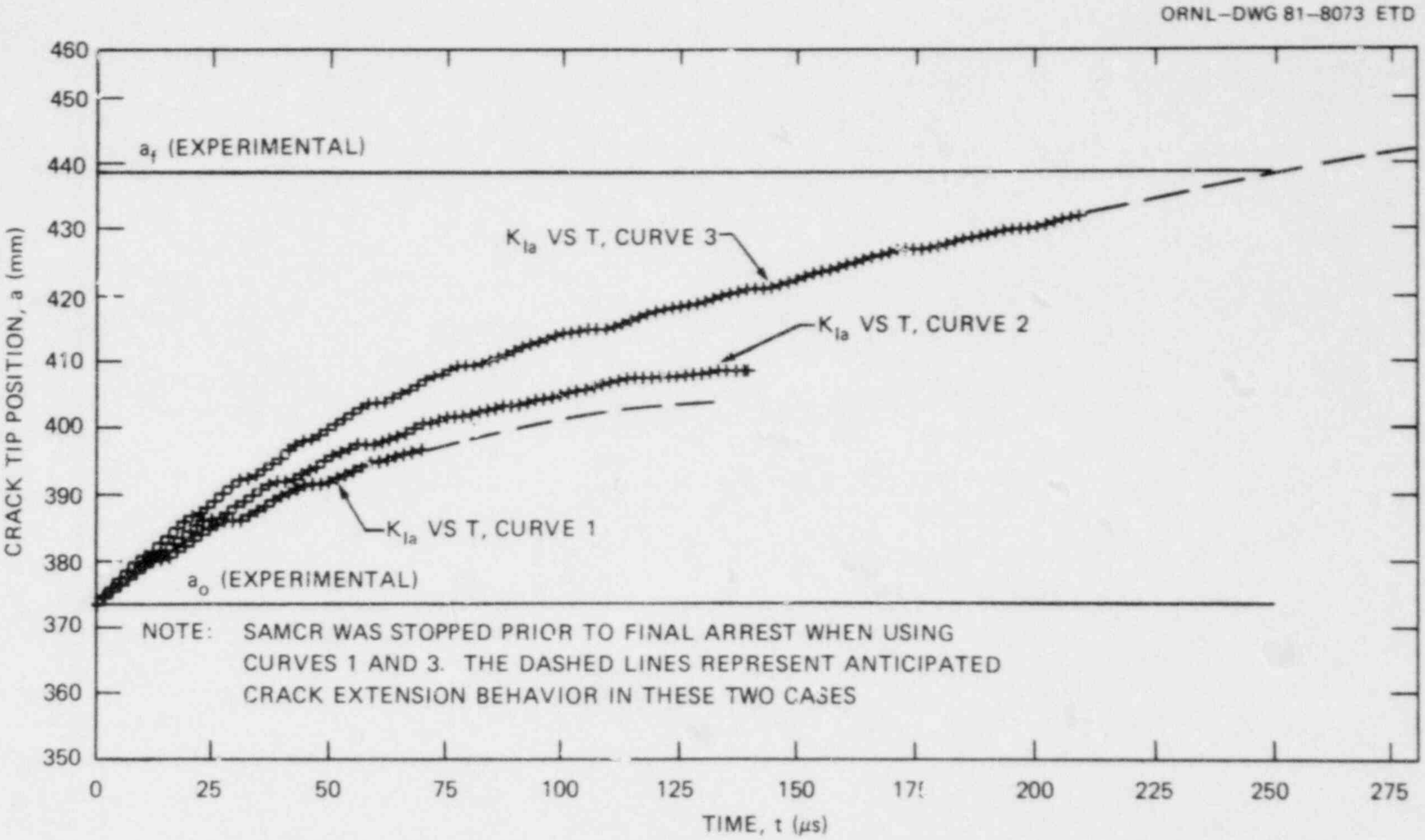

NOTE: SAMCR WAS STOPPED PRIOR TO FINAL ARREST WHEN USING CURVES 1 AND 3. THE DASHED LINES REPRESENT ANTICIPATED CRACK EXTENSION BEHAVIOR IN THESE TWO CASES

Fig. 2.44. Predicted crack extension behavior as a function of time from the three $K_{Ia}$ vs T relationships investigated.

## References

1. H. G. deLorenzi and C. F. Shih, "3-D Elastic-Plastic Investigation of Fracture Parameters in Side Grooved Compact Specimens," General Electric TIS Report 80CRD211 (1980).

2. J. R. Rice, "A Path Independent Integral and the Approximate Analysis of Strain Concentration by Notches and Cracks," *J. Appl. Mech.* 35, 379–86 (1968).

3. K. J. Bathe, "ADINA — A Finite Element Program for Automatic Dynamic Incremental Nonlinear Analysis," Massachusetts Institute of Technology Report 82448-1, (1975, revised 1978).

4. B. R. Bass and J. W. Bryson, "Computational Methods for Elastic-Plastic Fracture Mechanics," *Heavy-Section Steel Technology Program Quart. Prog. Rep. October–December 1980*, NUREG/CR-1941 (ORNL/NUREG/TM-437) pp. 8–11.

5. T. K. Hellen, "The Finite Element Calculations of Stress Intensity Factors Using Energy Techniques," paper G5/3, presented at Second International Conference on Structural Mechanics in Reactor Technology (SMiRT), Berlin, Germany, 1973.

6. D. M. Parks, "A Stiffness Derivative Finite Element Technique for Determination of Crack Tip Stress Intensity Factors," *Int. J. Fract.* 10(4), 487 (December 1974).

7. H. G. deLorenzi, "On the Energy Release Rate and the J-Integral for 3-D Crack Configurations," General Electric TIS Report 80CRD113 (1980).

8. H. G. deLorenzi, "3-D Elastic-Plastic Fracture Mechanics with ADINA," General Electric TIS Report No. 80CRD242 (1980).

9. R. S. Barsoum, "On the Use of Isoparametric Finite Elements in Linear Fracture Mechanics," *Int. J. Numer. Methods Eng.* 10, 25–37 (1976).

12. R. S. Barsoum, "Triangular Quarter-Point Elements as Elastic and Perfectly Plastic Crack Tip Elements," *Int. J. Numer. Methods Eng.* 11, 85–98 (1977).

11. J. C. Newman, "Stress Analysis of the Compact Specimen Including the Effect of Pin Loading," *Fracture Analysis*, ASTM STP 560, American Society for Testing and Materials, p. 105, 1974.

12. S. N. Atluri and M. Nakagaki, "J-Integral Estimates for Strain-Hardening Materials in Ductile Fracture Problems," *AIAA J.* 15(7), 923–31 (July 1977).

13. R. J. Bucci, P. C. Paris, J. D. Landes, and J. R. Rice, "J-Integral Estimation Procedures," *Fracture Toughness*, American Society Testing and Materials, ASTM/STP/514, pp. 40–70, 1972.

14. J. A. Begley and J. D. Landes, "The J-Integral as a Fracture Criterion," *Fracture Toughness*, American Society for Testing and Materials, ASTM/STP/514, pp. 1–20, 1972.

15. Klau-Jürgen Bathe and Edward L. Wilson, *Numerical Methods in Finite Element Analysis*, Prentice-Hall, Inc., Englewood Cliff, New Jersey, 1976.

16. Roshay S. Barsoum, "On the Use of Isoparametric Finite Elements in Linear Fracture Mechanics," *Int. J. Numer. Methods Eng.* 10, 25–87 (1976).

17. H. D. Biu, "Stress and Crack-Displacement Intensity Factor in Elastodynamics," *Advances in Research on the Strength and Fracture of Materials*, D. M. R. Taplin (Ed.), Vol. 3A, Pergamon Press, Elmsford, N.Y., pp. 91–5, 1977.

18. R. D. Cheverton, *HSST Thermal Shock Program Quick-Look Report for TSE-5A*, ORNL (October 1980).

19. A. R. Rosenfield et al., *Critical Experiments, Measurements and Analyses to Establish a Crack Arrest Methodology for Nuclear Pressure Vessel Steels*, NUREG/CR-1887 (1981).

20. A. R. Rosenfield and D. K. Shetty, "Lower-Bound Fracture Toughness of a Reactor-Pressure Vessel Steel," *Eng. Fract. Mech.* (to be published).

21. W. Seidl, "Specimen Size Effects on the Determination of $K_{IC}$-Values in the Range of Elastic-Plastic Material Behavior," *Eng. Fract. Mech.* 12, 581–97 (1979).

22. F. J. Witt, "The Equivalent Energy Method: An Engineering Approach to Fracture," *Eng. Fract. Mech.* 14, 171–87 (1981).

23. J. E. Srawley, "Wide Range Stress Intensity Factor Expressions for ASTM E 399 Standard Fracture Toughness Specimens," *Int. J. Fract.* 12, 475–6 (1976).

24. J. P. Gudas and J. A. Joyce, "Validation of Tearing Instability on Degraded LWR Piping," presented at Nuclear Regulatory Commission Eighth Water Reactor Safety Research Information Meeting, Gaithersburg, Maryland, Oct. 27–31, 1980.

25. D. P. Clausing, "Crack Stability in Linear Elastic Fracture Mechanics," *Int. J. Fract.* 5, 211–27 (1969).

26. J. C. Newman, "Stress Analysis of the Compact Specimen Including the Effects of Pin Loading," ASTM-STP 560, pp. 105–21, 1974.

27. W. Weibull, "A Statistical Theory of the Strength of Materials," *Ingeniorsvetenskapsakademiens Vetenskapsakademiens Handelgelar*, 151 (1939).

28. H. Kotilainen, "The Micromechanisms of Cleavage Fracture and Their Relationship to Fracture Toughness in a Bainitic Low Alloy Steel," *Materials and Processing Technology*, Publication 23, Technical Research Center of Finland, 1980.

29. G. T. Hahn, R. G. Hoagland, and A. R. Rosenfield, "The Variation of $K_{IC}$ with Temperature and Loading Rate," *Metall. Trans.* 2, 537–41 (1971).

30. R. O. Ritchie, W. L. Server, and R. A. Wullaert, "Critical Fracture Stress and Fracture Strain Models for the Prediction of Lower and Upper Shelf Toughness in Nuclear Pressure Vessel Steels," *Metall. Trans.* 10A, 1557–70 (1979).

31. Battelle Columbus Laboratories, "The Economic Aspects of Fracture in the U.S. Economy," unnumbered report to National Bureau of Standards, Dec. 31, 1980.

32. W. L. Fourney, "Investigation of Damping and of Cleavage-Fibrous Transition in Reactor-Grade Steel," *Heavy-Section Steel Technology Program Quart. Prog. Rep. October–December 1980*, NUREG/CR-1941 (ORNL/NUREG/TM-437), pp. 11–34.

33. G. R. Irwin et al., *Photoelastic Studies of Damping, Crack Propagation and Arrest in Polymers and 4340 Steel*, NUREG/CR-1455, Washington, D.C. (May 1980).

34. A. R. Rosenfield et al., *Critical Experiments, Measurements, and Analyses to Establish a Crack-Arrest Methodology for Nuclear-Pressure-Vessel Steels Prog. Rep. June–December 1979*, NUREG/CR-1555, Washington, D.C. (June 1980).

35. A. R. Rosenfield et al., *Critical Experiments, Measurements, and Analyses to Establish a Crack-Arrest Methodology for Nuclear-Pressure-Vessel Steels Prog. Rep. January–March 1980*, NUREG/CR-1601, Washington, D.C. (July 1980).

36. R. D. Cheverton, *Heavy-Section Steel Technology Program Quart. Prog. Rep. January–March 1980*, ORNL/NUREG/TM-393, p. 20 (July 1980).

37. R. D. Cheverton, *HSST Thermal Shock Program Quick-Look Report for TSE-5A*, ORNL, p. 23 (October 1980).

# 3. INVESTIGATION OF IRRADIATED MATERIALS

## Fourth HSST Irradiation Series

R. G. Berggren D. A. Canonico
T. N. Jones J. W. Woods

Approximately one-half the CVN specimens of A-533 grade B class 1 (HSST-02) steel from the first capsule, capsule A, were impact tested. The test results are presented in Fig. 3.1. The specimens were irradiated at 288°C to estimated fast neutron fluences of $8 \times 10^{18}$ to $2 \times 10^{19}$ neutrons/cm$^2$ (E > 1 MeV). Final results from neutron dosimeters included in this capsule are not yet available. The transition temperature shift for specimens irradiated to an estimated fluence of $2 \times 10^{19}$ neutrons/cm$^2$ was close to that predicted by *Regulatory Guide 1.99* (Ref. 1), but the upper-shelf energy loss was only one-third of that predicted by the Guide.

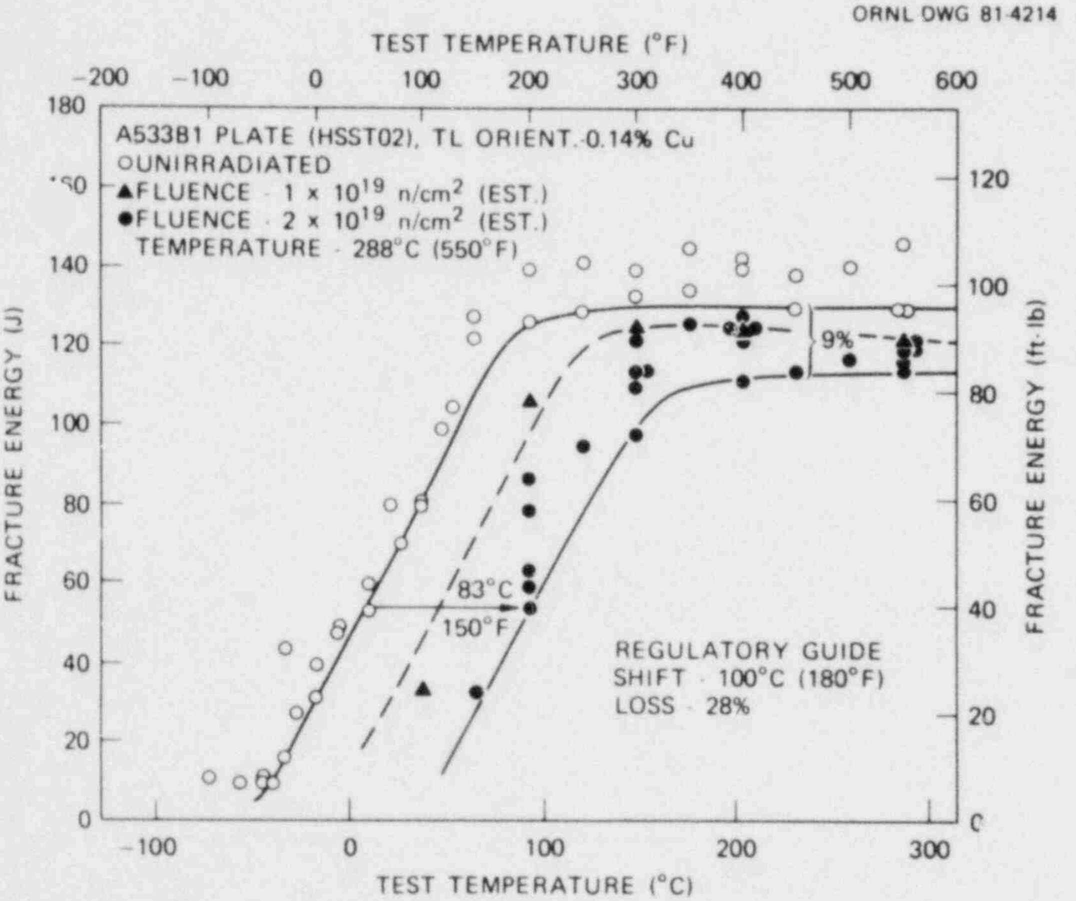

Fig. 3.1. Charpy V-notch impact test results for specimens from the Fourth HSST Irradiation Series, capsule A.

The second capsule of this series contains specimens of two submerged-arc welds with copper contents of 0.04 and 0.12%. The irradiation was completed March 6, 1981, after 4330 h of exposure at 288°C. The major portions of the specimens received an estimated fast neutron fluence of $2 \times 10^{19}$ neutrons/cm$^2$ ($E > 1$ MeV).

Assembly of the third capsule, capsule C, of this series was completed, and the capsule was installed in the Bulk Shielding Reactor (BSR) facility. Irradiation should begin in April 1981. This capsule contains specimens of "current practice" submerged-arc welds with copper contents of 0.046 and 0.056%.

Assembly of the fourth capsule, capsule D, of this series is expected to start in June 1981. The specimens for this capsule are being provided by the Federal Republic of Germany.

## Reference

1. U.S. Nuclear Regulatory Commission, "Effects of Residual Elements on Predicted Radiation Damage to Reactor Vessel Materials," *Regulatory Guide 1.99*, Rev. 1 (Sept. 16, 1976).

# 4. THERMAL SHOCK INVESTIGATIONS

R. D. Cheverton    S. K. Iskander

During this report period for the thermal shock program, the computer program OCA-I and a final draft of a report describing OCA-I were completed, OCA-I was used to perform a parametric analysis for a hypothetical overcooling accident involving both temperature and pressure transients, a proposal for TSE-6 was prepared and accepted, and possible reasons for the large scatter in lab $K_J$ data were examined.

## 4.1 The OCA-I Code

### 4.1.1 General description of OCA-I

The computer code OCA-I (previously referred to as OCA[1]) performs the thermal, stress, and fracture mechanics analyses for a pressurized-water reactor (PWR) pressure vessel that is subjected to transient thermal and pressure-loading conditions. The code was written to minimize time and cost associated with performing parametric-type analyses for an anticipated large number of hypothesized overcooling accidents. The present version of OCA-I calculates stress-intensity factors ($K_I$) for a long (2-D) axial flaw on the inner surface of a 4.80-m-OD by 4.37-m-ID cylinder that is subjected to internal pressure and cooling of the inner surface.

A general description of OCA-I is presented in the form of a block diagram in Fig. 4.1. Minimum input to the code related to the vessel and the thermal and pressure transients consists of the coolant temperature and pressure as functions of time [$T_B$, $p = f(t)$], the initial temperature of the vessel wall ($T_0$), the coolant-film heat transfer coefficient ($h$), the material preservice reference temperature ($RT_{NDT0}$), the fast neutron fluence at the inner surface ($F_0$), and the concentrations of copper and phosphorus (Cu, P). With this information available, OCA-I performs six basic calculations and as an end result produces a set of critical-crack-depth curves indicating the behavior of a long (2-D) axial flaw during the transient.

The six basic calculations performed by OCA-I consist of

1. a thermal analysis that provides the temperature distribution through the wall as a function of time (hereafter referred to as the temperature history);
2. a stress analysis that provides the circumferential stresses for the uncracked cylinder, considering both thermal and pressure loadings;
3. computations of $K_{Ic}$ and $K_{Ia}$ as functions of crack depth and time, based on the material property data included in the code and the temperature histories from 1;
4. a fracture mechanics analysis that provides $K_I$ for a long axial crack as a function of crack depth and time, using the stresses from 2;

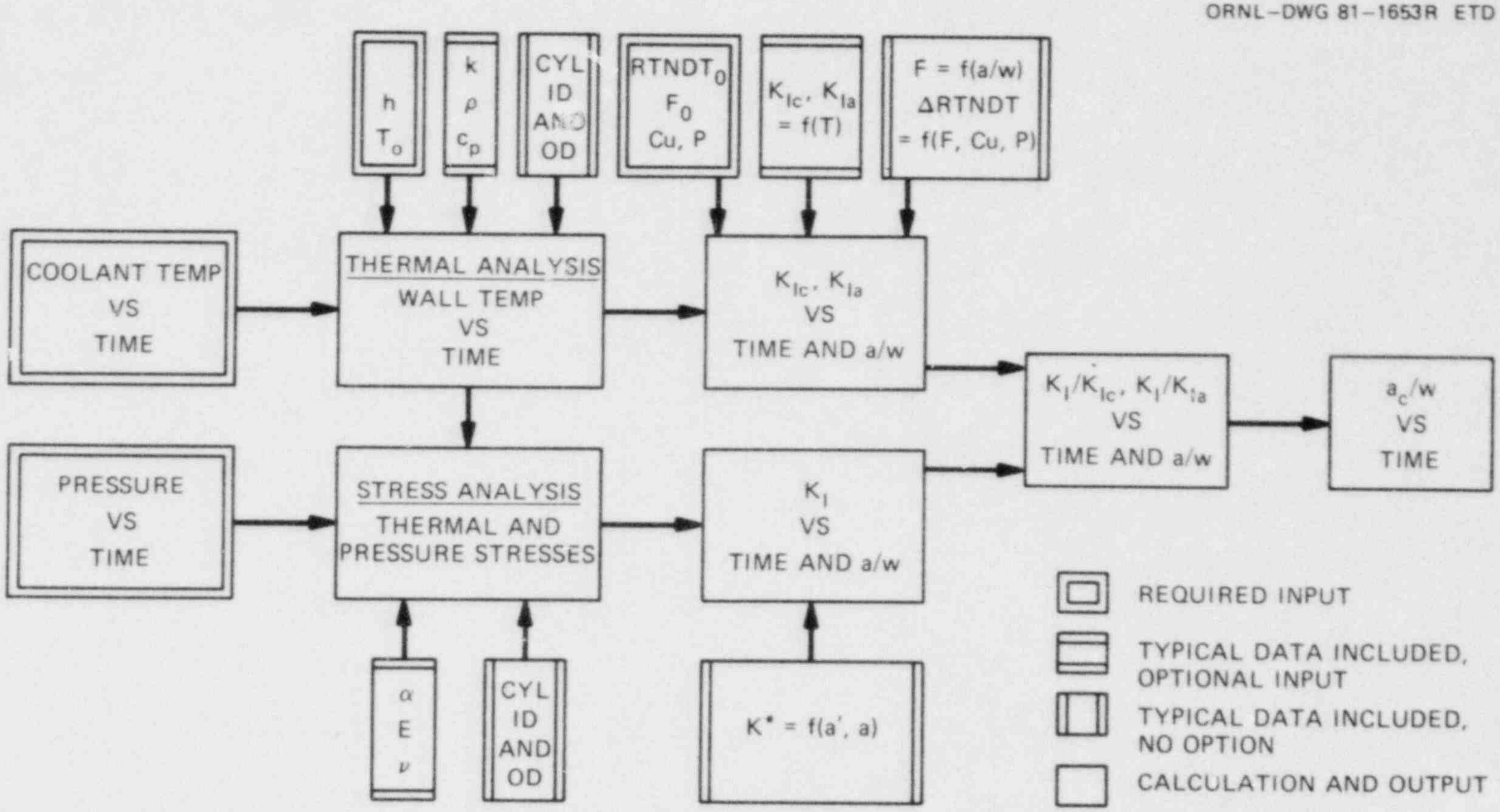

Fig. 4.1. Block-diagram description of OCA-I, indicating basic input, calculations and output.

5. a computation of the K ratios, $K_I/K_{Ic}$ and $K_I/K_{Ia}$, as a function of crack depth and time, based on the information from 3 and 4; and
6. an interpolation of the data in 5 to find the times for each of the different crack depths at which $K_I = K_{Ic}$ and $K_I = K_{Ia}$, the information that is used to construct the critical-crack-depth curves.

The OCA-I code is composed of two separate codes. One of those codes, 1-R, performs the heat transfer analysis referred to in item 1, and the other, FM, performs the remaining calculations (items 2 through 6), which constitute the fracture mechanics analysis. The OCA-I code is separated in this fashion for three reasons: (1) an examination of the temperature history for accuracy before proceeding with the fracture mechanics analysis is prudent, (2) the size of the computer memory required is nearly halved by breaking OCA-I down in this fashion, and (3) the use of the same temperature history for several fracture mechanics problems involving differences in fracture-mechanics-related input only (parametric-type analyses) may be desirable.

To further facilitate the parametric-type FM analysis, OCA-I was designed to accept several sets of fracture-mechanics-related input data and to automatically repeat the FM analysis for each set.

Immediate prospective users of OCA-I requested that the code be written in English units, and with the exception of the fast-neutron fluence (neutrons/cm$^2$), this was done. Thus, the following discussion of calculations and data used in OCA-I will make reference to English units where appropriate.

### 4.1.2 Thermal analysis

The temperature history for the cylinder is determined by modeling of the reactor vessel as an axisymmetric one-dimensional (1-D) structure, and temperatures are calculated as a function of the radial distance r. The 1-D axisymmetric heat conduction equation[2] that must be solved is

$$\rho c_p(\partial T/\partial t) = (1/r)(\partial/\partial r)[kr(\partial T/\partial r)] + Q , \quad (4.1)$$

where

$c_p$ = specific heat,
$k$ = thermal conductivity,
$\rho$ = density,
$Q$ = heat generation rate per unit volume,
$r$ = radius,
$T$ = $T(r,t)$, temperature in the wall,
$t$ = time,

and at the inner and outer surfaces

$$q = h(T_B - T_{c,d}) , \quad (4.2)$$

where

$h$ = surface heat transfer coefficient,
$q$ = surface heat flux,
$T_B$ = $T_B(t)$, bulk coolant temperature as a function of time,
$T_{c,d}$ = the temperature of the surface ($r = c,d$) in contact with the coolant,
$c,d$ = inner and outer radii of the cylinder.

The heat transfer code, I-R, which was specifically written for OCA-I to solve the thermal-transient problem encountered in light-water reactor (LWR) overcooling accidents, uses the finite-element method to solve Eq. (4.1). The particular finite-element technique employed utilizes an axisymmetric three-noded isoparametric element and interpolates the temperatures between nodes by means of a quadratic polynomial. A mesh spacing and a time step that are adequate for a broad range of overcooling accidents have been incorporated into the code; however, alternative values may be inputted.

In its present form I-R has the following features regarding modeling: (1) the thermal properties ($k$, $\rho$, $c_p$) and the heat transfer coefficient ($h$) are independent of time and temperature; (2) the initial temperature in the wall of the cylinder is uniform; (3) the cylinder can be modeled with any number of different materials; and (4) the coolant temperature [the boundary temperature $T_B$ in Eq. (4.2)] can be an arbitrary function of time.

### 4.1.3 Stress analysis

The calculation of $K_I$ requires a knowledge of the stress distributions in the cylinder wall caused by thermal and pressure loads, and as explained in Sect. 4.1.5, the stresses required are the circumferential stresses in the uncracked cylinder. The method used for calculating $K_I$ properly accounts for the redistribution of the stresses caused by the presence of the crack.

The circumferential thermal stresses, $\sigma_T$, in a long cylinder that is subjected to a radial temperature distribution are given by (Ref. 3)

$$\sigma_T = \frac{\alpha E}{(1 - \nu)} \frac{1}{r^2} \left[\left(\frac{r^2 + c^2}{d^2 - c^2}\right)\int_c^d Trdr + \int_c^r Trdr - Tr^2\right] , \qquad (4.3)$$

where

$\alpha$ = coefficient of thermal expansion,
$E$ = Young's modulus,
$\nu$ = Poisson's ratio,
$c,d$ = inner and outer radii of the cylinder,
$r$ = radial distance,
$T$ = temperature in wall at $r$.

The evaluation of the integrals in Eq. (4.3) is performed numerically because the temperature distribution T = f(r,t) is arbitrary. The distribution T = f(r,t) is obtained from the thermal analysis (Sect. 4.1.2).

The circumferential stresses caused by the internal pressure p are given by (Ref. 3)

$$\sigma_p = [c^2p/(d^2 - c^2)][1 + (d^2/r^2)] \ . \tag{4.4}$$

The equation p = f(t) is input to OCA-I.

The problem solved is assumed to be linear; thus, the total circumferential stresses are equal to $\sigma_T + \sigma_p = f(r,t)$.

### 4.1.4 Calculation of $K_{Ic}$ and $K_{Ia}$

The material toughness properties $K_{Ic}$ and $K_{Ia}$ must be calculated for all crack depths for each of the time steps in the transient analysis. This calculation requires a knowledge of (1) the material property data $K_{Ic}$ and $K_{Ia} = f(T)$; (2) the reference transition temperature for the material in an unirradiated condition, $RT_{NDT0}$, which is input to the code; and (3) the change in $RT_{NDT}$ as a result of radiation damage, which is a function of the fast neutron fluence and the copper and phosphorus concentrations. Also required is the temperature distribution in the wall of the cylinder as a function of time. This latter information is obtained from the thermal analysis (Sect. 4.1.2).

The users of OCA-I may input the $K_{Ic}$ and $K_{Ia} = f(T)$ data. However, OCA-I contains the ASME Section XI (Appendix A) curves for $K_{Ic}$ and $K_{Ia}$ vs $(T - RT_{NDT})$. These curves are shown in Fig. 4.2 and as indicated in Ref. 4 are represented by the following equations:

$$K_{Ic}\ (T') = 33.2 + 2.806 \exp\ [0.020\ (T' + 100)]\ ,\ (\mathrm{ksi}\sqrt{\mathrm{in.}})\ , \tag{4.5}$$

$$K_{Ia}\ (T') = 26.8 + 1.223 \exp\ [0.0145\ (T' + 160)]\ , \tag{4.6}$$

where

$T' = T - RT_{NDT0} - \Delta RT_{NDT}$ (°F),
T = actual temperature from thermal analysis (°F),
$RT_{NDT0}$ = reference temperature for unirradiated material (°F),
$\Delta RT_{NDT}$ = change in $RT_{NDT}$ caused by radiation damage (°F).

The ASME Code does not specify an upper shelf for the toughness curves [Eqs. (4.5) and (4.6)], but provisions have been made in OCA-I to include upper-shelf toughness values for both $K_{Ic}$ and $K_{Ia}$. If upper-shelf values are to be used, they must be specified by the user, otherwise an effectively infinite value is used by the code.

The relationship between $\Delta RT_{NDT}$, the fast neutron fluence (F) and the copper and phosphorus concentrations (Cu, P) proposed in *Regulatory Guide 1.99* (Ref. 5), is included in OCA-I and is shown graphically in Fig. 4.3

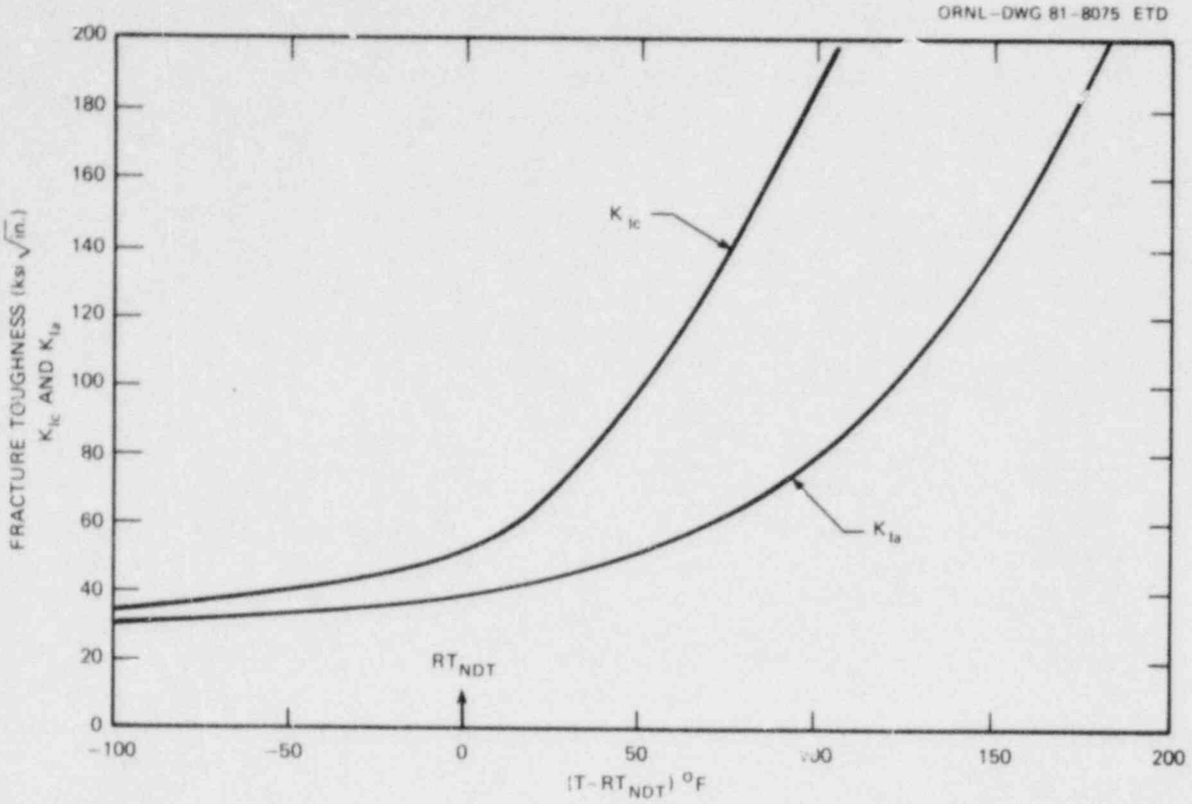

Fig. 4.2. $K_{Ic}$ and $K_{Ia}$ vs $(T - RT_{NDT})$ from ASME Section XI (Appendix A).

and in equation form as follows:

$$\Delta RT_{NDT} = [40 + 1000\ (\%\ Cu - 0.08) + 5000\ (\%\ P - 0.008)] \times (F \times 10^{-19})^{1/2} \quad (4.7)$$

or

$$\Delta RT_{NDT} = 283\ (F \times 10^{-19})^{0.194}\ ,\ ^\circ F\ . \quad (4.8)$$

The lesser of these two values is used (Fig. 4.3). Note in Fig. 4.3 that an upper limit exists on Cu of 0.35%.

The fast neutron fluence (F) is attenuated through the wall of the vessel, and OCA-I includes the following relation between F and radial distance into the wall (a):

$$F = F_0 \exp\ (-0.33a)\ , \quad (4.9)$$

ORNL-DWG 81-[illegible]074 ETD

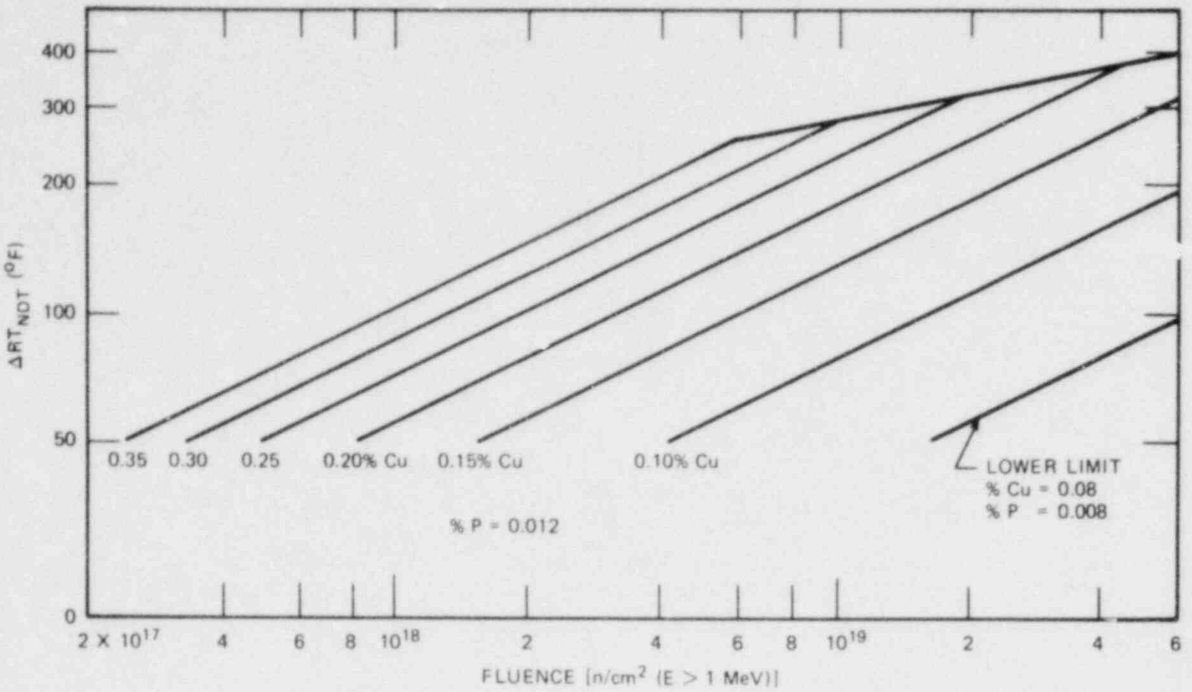

Fig. 4.3. $\Delta RT_{NDT}$ vs F. Data taken from *NRC Regulatory Guide 1.99*, Rev. 1 (September 1976).

where

$F$ = fast neutron fluence, $E \geq 1$ MeV (neutrons/cm$^2$),
$F_0$ = fluence at inner surface of wall,
$a$ = radial distance from inner surface of cylinder (in.),
$E$ = neutron energy.

Note that T, $\Delta RT_{NDT}$ and F correspond to conditions at the crack tip, a; thus, so do the values of $K_{Ic}$ and $K_{Ia}$ calculated from Eqs. (4.5) and (4.6).

### 4.1.5 Calculation of $K_I$

The stress intensity factor $K_I$ is calculated by a technique proposed by Bueckner.[6] Instead of calculating the cracked structure using the actual loads, this technique utilizes a distributed pressure applied to the crack surfaces only. This pressure is opposite in sign but equal in magnitude and distribution to the stresses along the crack line calculated for the uncracked structure with the actual loads applied.

The application of and justification for the above technique are discussed with the aid of Fig. 4.4. Figure 4.4(a) is an example problem to be solved, and Fig. 4.4(b) is the proposed method of solution; that is, the distributed pressure applied to the crack surface in Fig. 4.4(b) is

ORNL–DWG 81–8076 ETD

†FORCES SHOWN APPLIED TO UPPER SURFACE, OPPOSITE IN SIGN APPLIED TO LOWER SURFACE

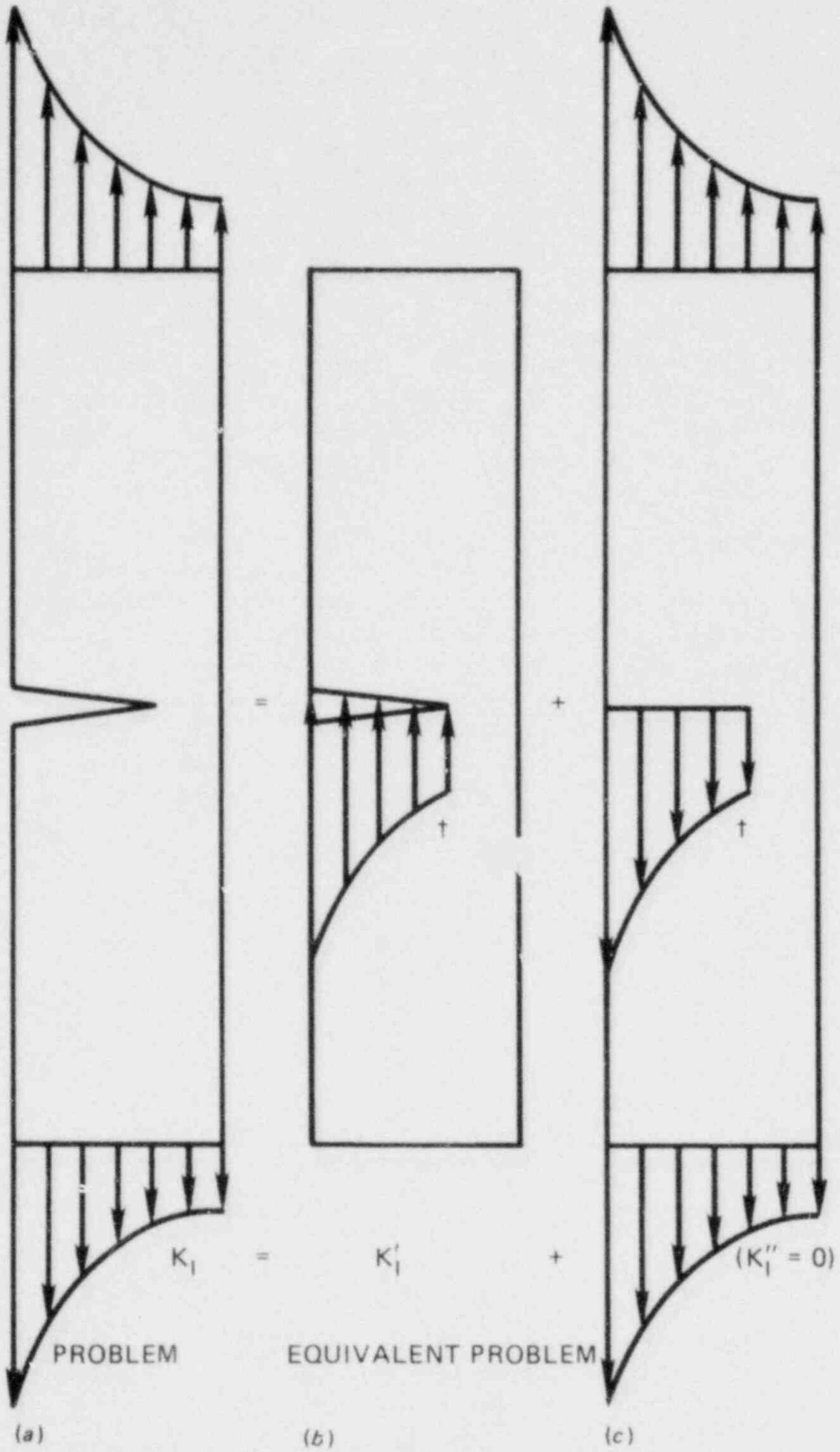

Fig. 4.4. Graphical representation of method proposed by Bueckner for calculating $K_I$ using equivalent problem.

equal in magnitude and distribution but opposite in sign to the stresses in the bar in Fig. 4.4(a) remote from the crack (those that would exist on the crack line if there were no crack). Figure 4.4(c) represents the same bar with the same end loads but with tractions applied to the crack surfaces, so that the crack is exactly closed. The tractions required to close the crack exactly are equal to the stresses on the end of the bar, because in the absence of the crack the stresses across the bar are equal to the stresses on the ends. This fact is sufficient proof that the scheme proposed by Bueckner works, because the tractions would have to rotate the crack surfaces through the same angle to close the crack as would occur when the tractions are removed and Fig. 4.4(a) is created. However, the proof can be extended as follows: suppose that the external loads in Figs. 4.4(b) and 4.4(c) are added, which can be done if we assume linearity. When these are added, the pressures and tractions on the crack surfaces will exactly cancel, and once again Fig. 4.4(a) is created. Thus the sum of the $K_I$ values calculated for Figs. 4.4(b) and 4.4(c) must be equal to the $K_I$ value for Fig. 4.4(a). Because the $K_I$ value for Fig. 4.4(c) is zero, the $K_I$ value for Fig. 4.4(b) must be equal to that for Fig. 4.4(a). Therefore, in determination of $K_I$ values, Fig. 4.4(b) is the equivalent of Fig. 4.4(a).

The advantage of the equivalent problem is that it can be solved relatively easily by superposition. The technique used for OCA-I calculates $K_I$ values separately for each of several unit loads applied at specified points along a crack surface, which is done for all crack depths of interest and needs to be done only once for a given set of cylinder dimensions. When applied to an actual problem, the unit-load $K_I$ values ($K^*$) for a selected crack depth are weighted in accordance with the crack-free stress distribution associated with the equivalent problem. Then the actual $K_I$ value is obtained by superposition, that is, by summing the weighted $K^*$ values. The procedure is summarized as follows:

$$K_I(a) = \sum_{i=1}^{n} \sigma_i \Delta a_i K_i^*(a_i',a) \;, \qquad (4.10)$$

where

$\Delta a_i$ = an increment of a about a',

$\sum_{i=1}^{n} \Delta a_i = a$,

$a_i'$ = radial distance from open end of crack (cylinder surface) to point of application of unit load,

$\sigma_i$ = average stress over $\Delta a_i$ for equivalent problem,

$K_i^*$ = stress intensity factor per unit load applied at $a_i'$ per unit length of cylinder,

n = number of points along length of crack for which $K^*$ values are available.

The various parameters are defined graphically in Fig. 4.5.

ORNL-DWG 81-8077 ETD

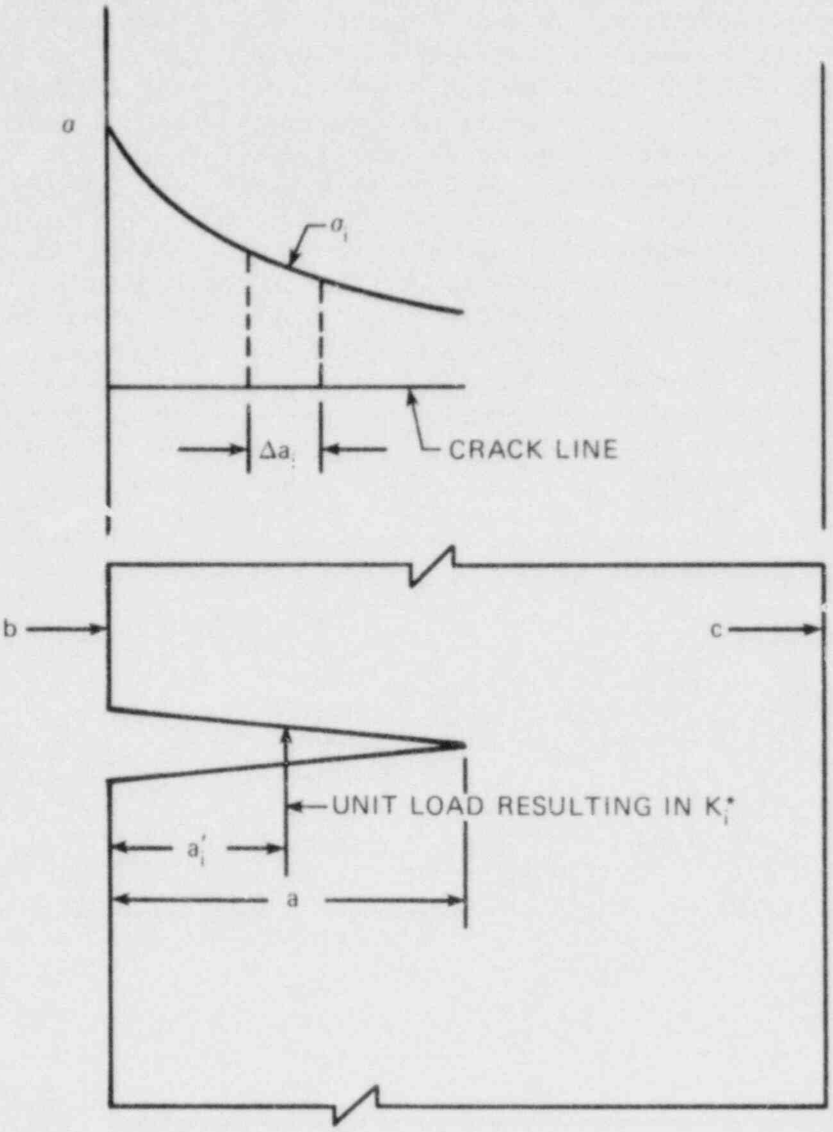

$$K_I(a) = \sum_{i=1}^{n} \sigma_i \, \Delta a_i \, K_i^*(a', a)$$

Fig. 4.5. Illustration of stresses along crack line in uncracked cylinder and application of unit load to crack face.

The $K^*$ values included in OCA-I were calculated with the finite-element code FMECH[7] for 15 different crack depths in a cylinder that has typical dimensions for a 1000-MW(e) PWR (172 in. ID by 189 in. OD). Details pertaining to actual crack depths and number of $K^*$ values along each crack face are discussed in Sect. 4.1.9.

### 4.1.6 Calculation of $K_I/K_{Ic}$ and $K_I/K_{Ia}$

The calculation of $K_I/K_{Ic}$ and $K_I/K_{Ia}$ as a function of crack depth and time in the transient is a simple operation using the $K_I$, $K_{Ic}$, and $K_{Ia} = f(a/w,t)$ data from Sects. 4.1.4 and 4.1.5.

### 4.1.7 Construction of the critical-crack-depth curves ($a_c/w$ vs time)

The critical-crack-depth curves are obtained by plotting the crack depths corresponding to the initiation and arrest events ($K_I = K_{Ic}$ and $K_I = K_{Ia}$) as a function of the times at which these events occur. The code finds these critical crack depths and the corresponding times by interpolation of the $K_I/K_{Ic}$ and $K_I/K_{Ia} = f(a/w,t)$ data from Sect. 4.1.6. The warm prestressing (WPS) curve $[K_I = (K_I)_{max}]$ is not provided by OCA-I but can be constructed easily afterward with the aid of the $K_I = f(t,a/w)$ data available as output.

### 4.1.8 OCA-I output

The OCA-I code provides output from each of the six basic calculations in tabular form. Plots of the output can also be obtained if specific plotting software is available to the user.

Tabulated results for 1-R consist of wall temperature (T) vs radial position in the wall (r) for each time specified. Tabulated results for the FM code consist of T, $\sigma_T + \sigma_p$, $K_I$, $K_{Ic}$, $K_I/K_{Ic}$, $K_{Ia}$, $K_I/K_{Ia}$ — all vs r; a = r — c, a/w, for all specified times; and a table of critical-crack-depth data ($a_c/w$ vs t) is also included.

### 4.1.9 Input considerations

As indicated in Fig. 4.1, three categories of input for OCA-I exist: mandatory, optional, and fixed. The mandatory input includes $T_B$ vs t, $T_0$, p vs t, h, $RT_{NDT0}$, $F_0$, Cu, P, and the time intervals for output. Optional input is optional in the sense that values are already included in the code, but other values may be inputted by the user. This category includes $K_{Ic}$ and $K_{Ia}$ vs temperature, $(k, \rho, c_p, \alpha, E, \nu) \neq f(T)$, and mesh spacing and time step for the thermal analysis. The category referred to as fixed includes the radial dimensions of the cylinder (c and d), fractional crack depths (a/w) for which $K_I$ calculations are made, $F = f(a/w)$ and $\Delta RT_{NDT} = f(F, Cu, P)$. With some minor modifications to the code, even these parameters can be changed, but changing the vessel dimensions and/or the a/w's requires the calculation of a new set of $K^*$ values.

The material properties and the fluence attenuation included in the code are typical for a PWR vessel, and the omission of temperature dependence for those properties indicated does not substantially affect the results of the analysis. Thus, one should be able to use these data with confidence for most cases. The toughness properties and the attenuation of the fluence included in the code are discussed in Sect. 4.1.4; the other material properties are given in Table 4.1. The number and depth of cracks and the number of $K^*$ values provided for each crack depth are presented in Table 4.2.

The mesh spacing included in 1-R includes 21 nodes (10 elements) with a geometric progression factor of 1.13; the time step is 0.15 s.

Table 4.1. Pressure-vessel material property data included in OCA-I as optional input

| Property | Input |
|---|---|
| Thermal conductivity, Btu/h·ft·°F | 24 |
| Density, $lb/ft^3$ | 489 |
| Specific heat, Btu/lb·°F | 0.120 |
| Linear coefficient of thermal expansion, $°F^{-1}$ | $6.5 \times 10^{-6}$ |
| Modulus of elasticity, $lb/in.^2$ | $28 \times 10^6$ |
| Poisson's ratio | 0.3 |

Table 4.2. Fractional crack depths and number of $K^*$ values (for each crack depth) used by OCA-I in the FM code[a]

| Crack-depth ID No. (used internally by OCA-I) | Fractional crack depth, a/w | Number of $K^*$ values |
|---|---|---|
| 1 | 0 | 0 |
| 2 | 0.02647 | 6 |
| 3 | .5588 | 11 |
| 4 | 0.07641 | 14 |
| 5 | 0.10147 | 16 |
| 6 | 0.1500 | 17 |
| 7 | 0.20147 | 19 |
| 8 | 0.2500 | 21 |
| 9 | 0.3011 | 23 |
| 10 | 0.40147 | 25 |
| 11 | 0.5000 | 27 |
| 12 | 0.60012 | 31 |
| 13[b] | | |
| 14 | 0.70735 | 34 |
| 15 | 0.8000 | 37 |
| 16 | 0.8500 | 37 |
| 17 | 0.9000 | 37 |

[a] Cylinder dimensions: 172 in. ID and 189 in. OD.

[b] Not used.

The accuracy of these values is discussed in Sect. 4.1.10. If a different mesh is to be used, the inner and outer radii (c and d) of the vessel must remain exactly the same as they are (c = 86.00 in., d = 94.50 in.), because the $K^*$ values included in the code are based on these dimensions.

### 4.1.10 Accuracy checks for OCA-I

In the process of developing OCA-I, accuracy checks were made on numerical analysis and the superposition technique used for calculating $K_I$ values.

The transient thermal analysis, which is performed with the 1-R code, requires a mesh spacing and time step. Those selected for normal use include 21 nodes (10 elements) with a geometric progression factor of 1.13 and a constant time step of 0.15 s. The mesh spacing was declared acceptable after an accuracy check was performed using this mesh and a coarser mesh consisting of 11 nodes (5 elements) with a geometric progression factor of 1.40. The particular thermal transient calculated was that corresponding to a PWR loss-of-coolant accident (LOCA), which is probably as severe a thermal transient as will be encountered. The results of the two cases were essentially identical, and for the purpose of adding some conservatism with regard to mesh size, the finer mesh was included as part of the optional input to 1-R. Similar tests were conducted using different time steps, and the results indicated that 0.15 s was adequate.

Aside from mesh and time-step considerations, the accuracy of 1-R was checked by comparing the temperatures calculated with 1-R to those calculated using the well-established HEATING5 computer code.[8] The agreement was excellent.

A comparison of results from 1-R and HEATING5 is shown in Fig. 4.6 for the 11-node 1-R case and in Fig. 4.7 for the 21-node 1-R case. The HEATING5 curve is the same in both figures and was obtained with a mesh and time step that had previously been found adequate. As indicated, the agreement between codes and meshes is very good (a more precise comparison indicates differences to be <1%).

The method that OCA-I uses for calculating $K_I$ (Sect. 4.1.5) was checked by comparison of the results from OCA-I with those from our conventional finite-element analysis method (FMECH[7] code). The FMECH code has been used for many previous $K_I$ calculations and has been thoroughly checked against other finite-element codes and for mesh convergence.[7,9] It was also used for calculation of the $K^*$ values included in OCA-I.

The above comparisons of OCA-I and FMECH were conducted for a PWR accident that involved both severe temperature and pressure transients and also for the PWR-LOCA, which has an even more severe thermal transient and an effectively zero pressure differential. A comparison of results for the PWR-LOCA at a time in the transient when $K_I$ values are nearly maximum for all crack depths is presented in Table 4.3. The agreement is observed to be within <1% for all crack depths included in OCA-I ($0.02 \leq a/w \leq 0.90$). This same good comparison was obtained for all other cases as well. Thus, the OCA-I technique for calculating $K_I$, including the particular mesh spacing used and the number of $K^*$ values provided for each crack depth (Table 4.2), is considered adequate for its intended purpose.

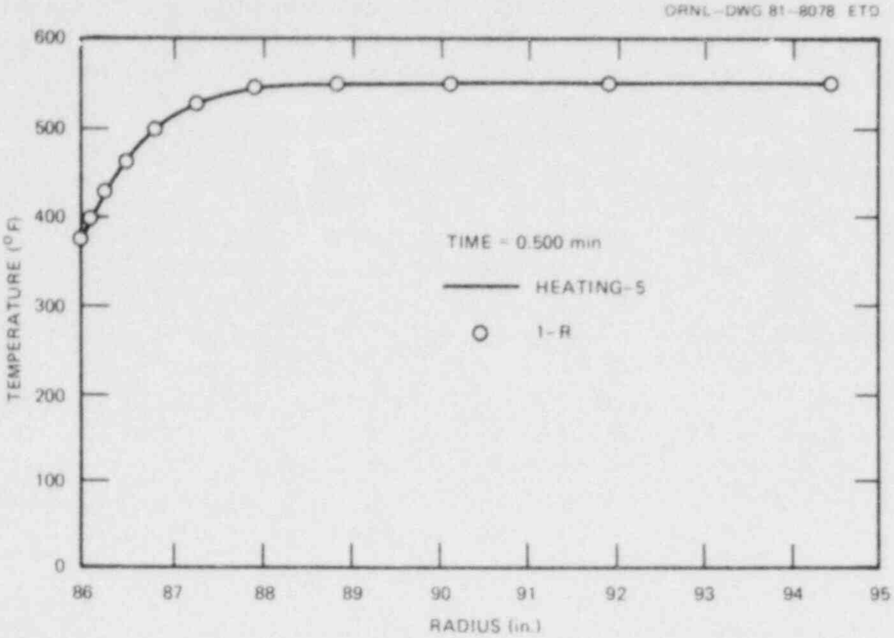

Fig. 4.6. Comparison of results from HEATING5 and 1-R for PWR-LOCA conditions, using 11 mesh points for 1-R.

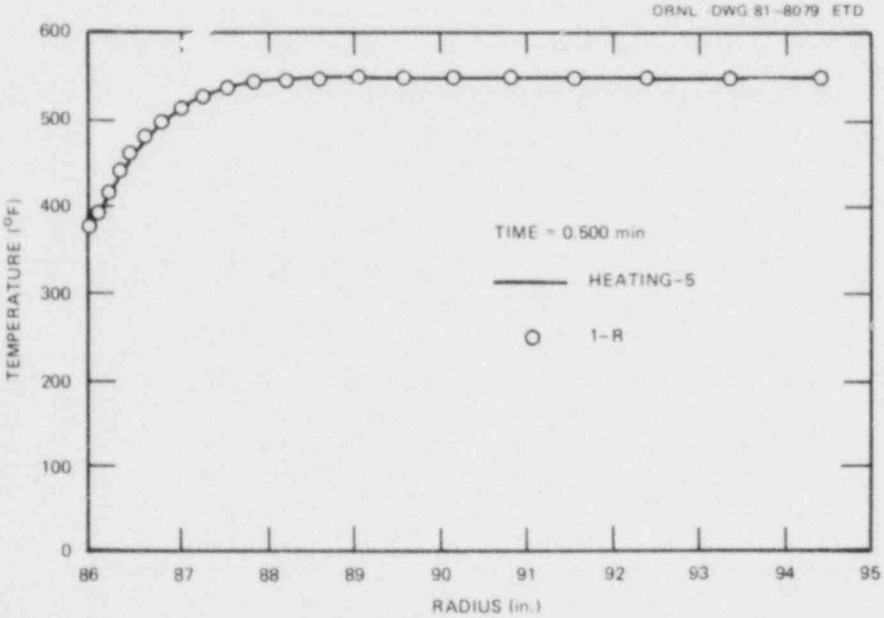

Fig. 4.7. Comparison of results from HEATING5 and 1-R for PWR-LOCA conditions, using 21 mesh points for 1-R.

Table 4.3. Comparison[a] of $K_I$ values at t = 10 min calculated with OCA-I and FMECH for the PWR-LOCA

| Crack depth, a/w | $K_I$ values ($\text{ksi}\cdot\sqrt{\text{in.}}$) | |
|---|---|---|
| | FMECH | OCA-I |
| 0.02 | 50.27 | 50.10 |
| 0.05 | 69.68 | 69.41 |
| 0.07 | 80.14 | 79.99 |
| 0.10 | 89.82 | 89.62 |
| 0.15 | 104.76 | 104.58 |
| 0.20 | 117.86 | 117.76 |
| 0.25 | 130.81 | 130.82 |
| 0.30 | 140.55 | 140.49 |
| 0.40 | 165.18 | 165.17 |
| 0.50 | 197.74 | 197.76 |
| 0.60 | 235.80 | 235.80 |
| 0.70 | 290.71 | 290.22 |
| 0.80 | 335.95 | 335.94 |
| 0.85 | 340.34 | 340.30 |
| 0.90 | 316.80 | 316.60 |

[a] These calculations were made with k = 26 Btu/h·ft·°F and $c_p$ = 0.124 Btu/lb·°F. Present OCA-I default values are 24 and 0.120.

## 4.2 Parametric Analysis of a PWR Overcooling Accident

A PWR hypothetical overcooling accident was analyzed that involved both temperature and pressure transients. A parametric-type analysis was performed using OCA-I; the parameters varied and their values are shown in Table 4.4. Two complete sets of calculations were made: one for the case of no upper shelf toughness and the other for a $K_{Ic}$ and $K_{Ia}$ upper shelf of $440\ \text{MPa}\cdot\sqrt{\text{m}}$, which was not necessarily intended to represent a realistic upper shelf but rather to indicate the general effect of including an upper shelf.

The single set of temperature and pressure transients considered for the study is described in Fig. 4.8. The fluid-film heat transfer coefficient was $1.87 \times 10^3\ \text{W/m}^2\cdot{}^\circ\text{C}$, and the initial temperature of the vessel wall was 299°C. All other input was that included in OCA-I.

Results of the analysis in the form of $K_I = f(t, a/w)$ curves (Fig. 4.9) indicate that WPS may be effective in limiting crack growth; that

Table 4.4. Parameters varied in the overcooling-accident analysis and their values

| Parameter | Value |
|---|---|
| $RT_{NDT0}$, °C | −6.7, 4.4 |
| Copper, % | 0.1, 0.25, 0.35 |
| $F_0$, $10^{19}$ neutrons/$cm^2$ | 0.6, 0.8, 1.0, 2.0, 3.0, 4.0 |

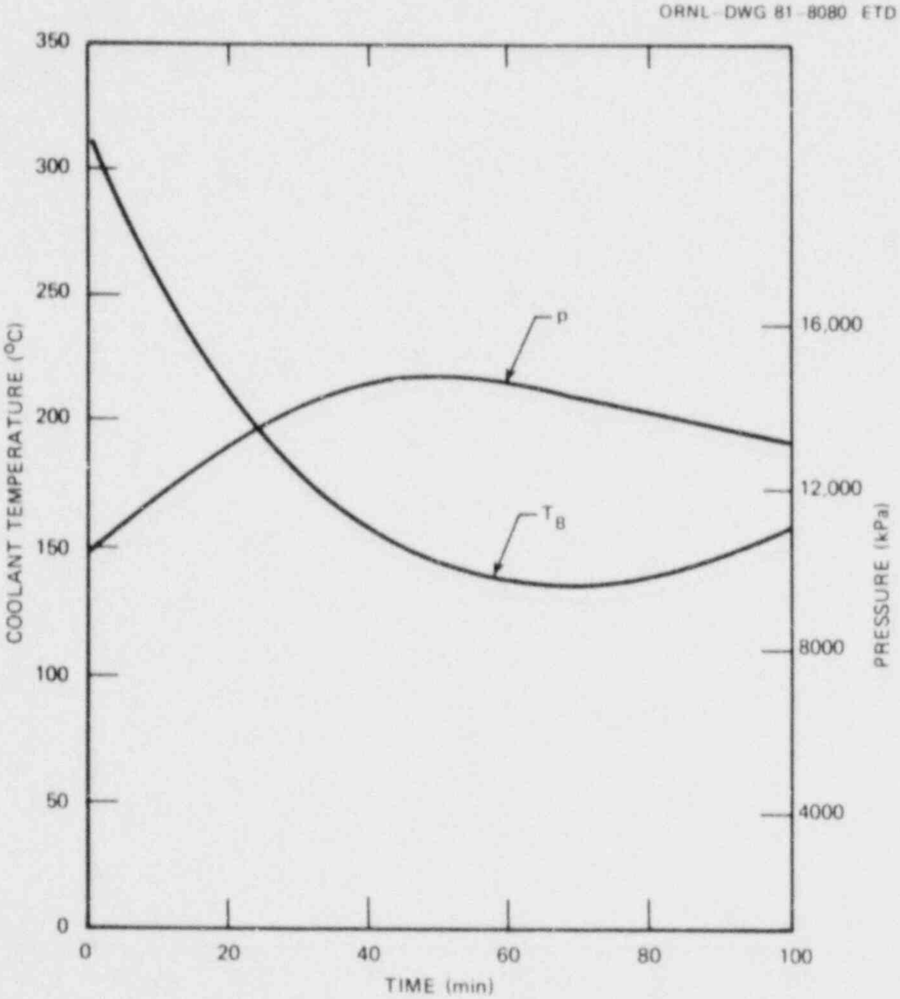

Fig. 4.8. Temperature and pressure transients used in OCA-I.

ORNL-DWG 81-8081 ETD

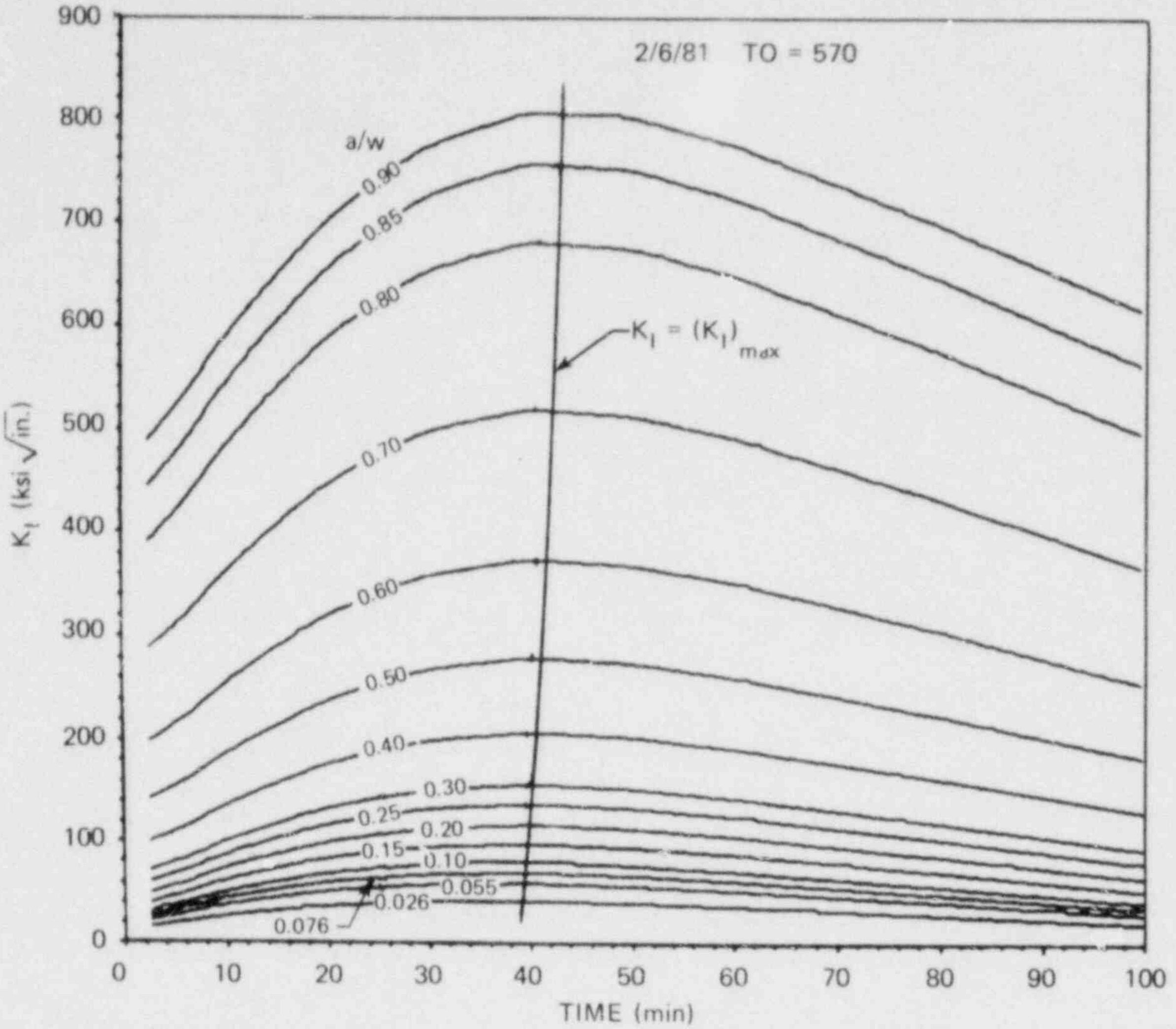

Fig. 4.9. $K_I$ vs t and a/w for PWR T-p transient.

is, for all crack depths (a/w) the stress intensity factor ($K_I$) first increases with time and then decreases. A set of critical-crack-depth curves (Fig. 4.10) for the most severe case analyzed ($RT_{NDT0} = 4°C$, $F_0 = 4 \times 10^{19}$ neutrons/cm$^2$, Cu = 0.35%) indicates that if WPS is ignored, crack depths (a/w) ranging from 0.03 to >0.9 will result in penetrations >0.90. If WPS is considered, the range of crack depths that will initiate is reduced to 0.03 to 0.43, and not all crack depths in this range will result in 90% wall penetration.

The effect of including an upper shelf for the toughness curves is shown for the same case in Fig. 4.11. The upper shelf affects only the deeper flaws (a/w > 0.6), for which the $K_I$ values at initiation tend to be higher than those for shallower cracks. A better illustration of this effect is shown in Fig. 4.12, which corresponds to the same case with the

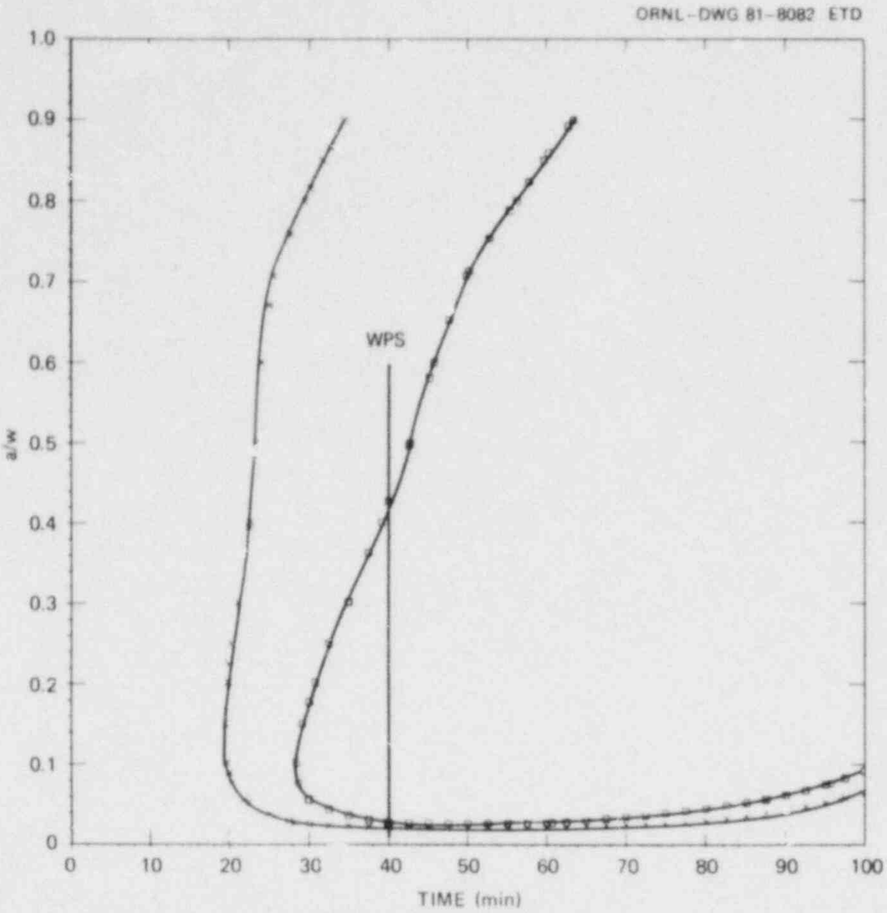

Fig. 4.10. Critical-crack-depth curves for PWR T-p transient: no upper shelf, $F_0 = 4 \times 10^{19}$ neutrons/cm$^2$.

exception that $F_0 = 0.8 \times 10^{19}$ neutrons/cm$^2$. As indicated, at this earlier time in the life of the vessel only a small range in crack depth (0.08 to 0.5) corresponds to crack initiation, if the upper shelf is ignored. Otherwise, much deeper flaws ($a/w \geq 0.6$) can initiate (tear) as well and at any time during the transient. Because such deep cracks are not likely to exist as initial flaws, inclusion of the upper shelf does not have a significant effect on the calculated integrity of the vessel.

Results of the parametric analysis for the case of no upper shelf are summarized in Table 4.5, and for this summary two conditions were considered: one excludes the effects of WPS and the other includes WPS.

The inclusion of WPS has the effect of increasing the threshold fluence for crack initiation; that is, the life of the vessel is prolonged. For instance, for the case mentioned previously ($RT_{NDT0} = 4°C$, Cu = 0.35%), if WPS is ignored, the threshold fluence is $0.75 \times 10^{19}$, but if WPS is included, the threshold fluence is $1.70 \times 10^{19}$. If we assume eight full-power years per $1 \times 10^{19}$ neutrons/cm$^2$, the corresponding lifetimes for the vessel are 6.0 and 13.6 full-power years, respectively.

Table 4.5. Overcooling-accident critical crack depths for initiation and arrest, assuming no upper shelf for toughness curves

| $F_0$ ($10^{19}$ neutrons/cm$^2$) | Approximate full-power time (years) | Neglecting WPS | | Including WPS | | Neglecting WPS | | Including WPS | |
|---|---|---|---|---|---|---|---|---|---|
| | | $(a_c/w)_i$ | $(a_c/w)_a$ | $(a_c/w)_i$ | $(a_c/w)_a$ | $(a_c/w)_i$ | $(a_c/w)_a$ | $(a_c/w)_i$ | $(a_c/w)_a$ |
| | | $RT_{NDT0}$ = –6.7°C, Cu = 0.10% | | | | $RT_{NDT0}$ = 4.4°C, Cu = 0.10% | | | |
| 0.6 | 4.8 | [a] | | | | [a] | | | |
| 0.8 | 6.4 | [a] | | | | [a] | | | |
| 1.0 | 8 | [a] | | | | [a] | | | |
| 2.0 | 16 | [a] | | | | [a] | | | |
| 3.0 | 24 | [a] | | | | [a] | | | |
| 4.0 | 32 | [a] | | | | [a] | | | |
| | | $RT_{NDT0}$ = –6.7°C, Cu = 0.25% | | | | $RT_{NDT0}$ = 4.4°C, Cu = 0.25% | | | |
| 0.6 | 4.8 | [a] | [a] | [a] | [a] | [a] | [a] | [a] | [a] |
| 0.8 | 6.4 | [a] | [a] | [a] | [a] | [a] | [a] | [a] | [a] |
| 1.0 | 8 | [a] | [a] | [a] | [a] | [a] | [a] | [a] | [a] |
| 1.50 | | | | | | [b] | | | |
| 1.80 | | [b] | | | | | | | |
| 2.0 | 16 | 0.06–0.18 | 0.38–>0.9 | [a] | [a] | 0.04–0.30 | 0.34–>0.9 | | |
| 2.25 | | | | | | | | [b] | |
| 2.85 | | | | [b] | | | | | |
| 3.0 | 24 | 0.04–0.44 | 0.33–>0.9 | 0.05–0.18 | 0.33–0.38 | 0.[illegible]–0.66 | 0.33–>0.9 | 0.04–0.23 | 0.33–0.47 |
| 4.0 | 32 | 0.03–0.72 | 0.39–>0.9 | 0.04–0.29 | 0.39–0.52 | 0.03–>0.9 | 0.38–>0.9 | 0.03–0.34 | 0.38–0.64 |
| | | $RT_{NDT0}$ = –6.7°C, Cu = 0.35% | | | | $RT_{NDT0}$ = 4.4°C, Cu = 0.35% | | | |
| 0.6 | 4.8 | [a] | [a] | [a] | [a] | [a] | [a] | [a] | [a] |
| 0.75 | | | | | | [b] | | | |
| 0.8 | 6.4 | [a] | [a] | [a] | [a] | 0.08–0.15 | 0.5–>0.9 | [a] | [a] |
| 1.0 | 8 | [a] | [a] | [a] | [a] | 0.06–0.32 | 0.5–>0.9 | [a] | [a] |
| 1.20 | | [b] | | | | | | | |
| 1.70 | | | | | | | | [b] | |
| 2.0 | 16 | 0.05–>0.9 | 0.59–>0.9 | [a] | [a] | 0.04–>0.9 | 0.6–>0.9 | 0.06–0.20 | 0.6–0.65 |
| 2.50 | | | | [b] | | | | | |
| 3.0 | 24 | 0.04–>0.9 | 0.68–>0.9 | 0.05–0.23 | 0.68–0.80 | 0.03–>0.9 | 0.7–>0.9 | 0.03–0.35 | 0.7–0.90 |
| 4.0 | 32 | 0.03–>0.9 | 0.78–>0.9 | 0.04–0.33 | 0.78–>0.9 | 0.03–>0.9 | 0.8–>0.9 | 0.03–0.5 | 0.8–>0.9 |

[a] No initiation.

[b] Threshold.

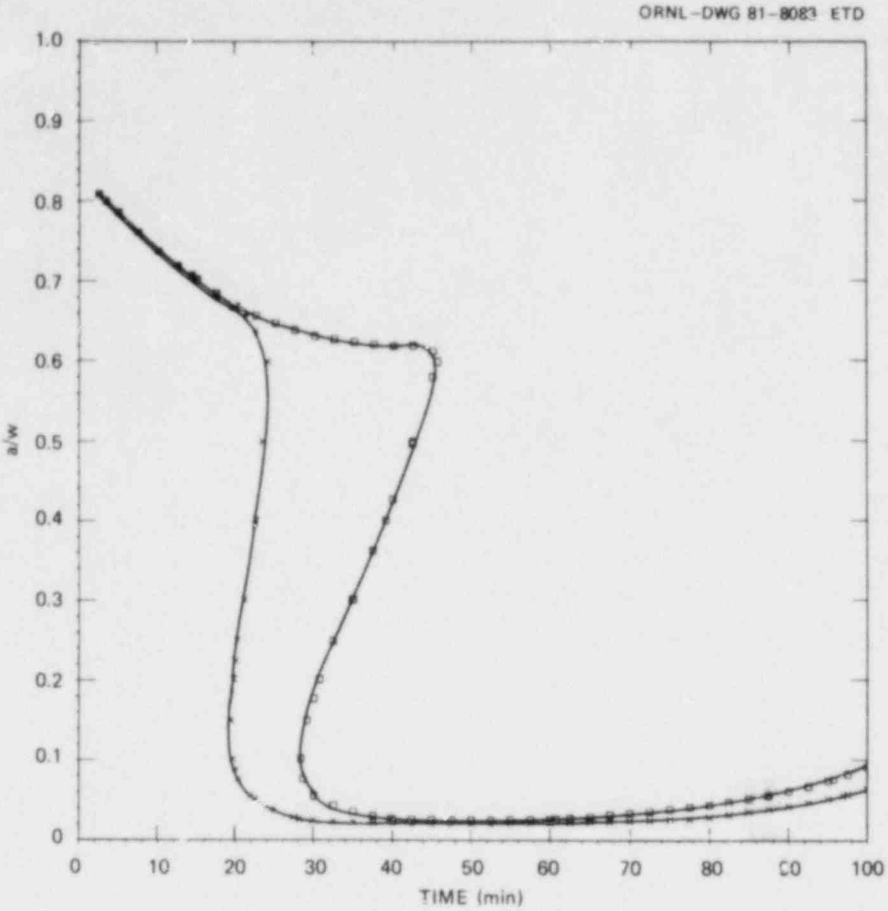

Fig. 4.11. Critical-crack-depth curves for PWR T-p transient: upper shelf, $F_0 = 4 \times 10^{19}$ neutrons/cm$^2$.

The summary in Table 4.5 indicates that in some cases for which WPS is included the final arrested crack depth will be $\leq 0.9$. This fact implies that the vessel would not fail. However, if the crack is deeper than $\sim 0.7$ and full operating pressure is applied, the vessel will burst because the remaining uncracked ligament is not strong enough to support the pressure. Furthermore, when a reasonable upper-shelf toughness is included, stable tearing would probably be predicted for $a/w \gtrsim 0.7$.

For the purpose of this study, two limiting conditions with regard to vessel permissible lifetime were considered: (1) the operating time required to achieve incipient crack initiation and (2) the operating time required for crack initiation to result in a calculated final crack depth equal to 0.7. These operating times are summarized in Table 4.6.

Results of the calculations that included an upper-shelf toughness of $440\ \mathrm{MPa}\cdot\sqrt{\mathrm{m}}$ indicate, as mentioned above, that $K_I$ values equal to the upper shelf will be achieved for $a/w \gtrsim 0.6$. Once this crack depth is reached as a result of propagation of initially shallower flaws, the vessel will probably fail as a result of tearing and finally bursting. If the upper-shelf value used is realistic or too high, the vessel lifetimes

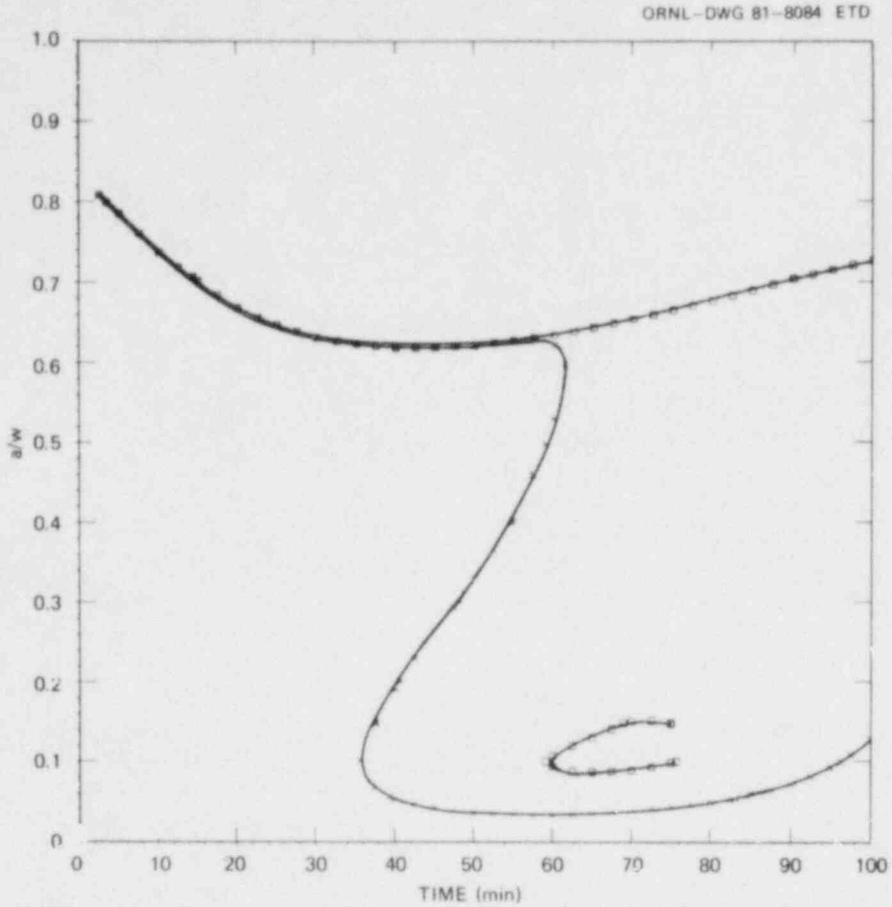

Fig. 4.12. Critical-crack-depth curves for PWR T-p transie [illegible] upper shelf, $F_0 = 0.8 \times 10^{19}$ neutrons/cm$^2$.

Table 4.6. Operating times required to achieve incipient crack initiation and a final arrested crack depth (a/w) of 0.7 (full-power years)

| Cu (%) | $RT_{NDT0} = -7°C$ | | | | $RT_{NDT0} = 4°C$ | | | |
|---|---|---|---|---|---|---|---|---|
| | WPS | | Without WPS | | WPS | | Without WPS | |
| | ICI | $(a_c/w)_a = 0.7$ | ICI | $(a_c/w)_a = 0.7$ | ICI | $(a_c/w)_a = 0.7$ | ICI | $(a_c/w)_a = 0.7$ |
| 0.1 | >32 | >32 | >32 | >32 | >32 | >32 | >32 | >32 |
| 0.25 | >32 | 23 | 14 | 14 | >32 | 18 | 12 | 12 |
| 0.35 | 20 | 20 | 10 | 10 | 14 | 14 | 6 | 6 |

based on final crack depth will be less than those indicated in Table 4.6 but not less than the incipient crack initiation (ICI) values, because $K_I$ values corresponding to ICI are very low ($\leq 100$ MPa$\cdot\sqrt{m}$).

## 4.3 Proposal for TSE-6

Thermal shock experiment[6] TSE-6 will be the seventh in a series of experiments conducted for the purpose of investigating the behavior of surface flaws in thick-walled steel cylinders subjected to severe thermal shock. Results of the first six experiments (TSE-1, 2, 3, 4, 5, 5A) indicate that (1) linear-elastic fracture mechanics is valid for both shallow ($a/w < 0.2$) and deep ($0.2 \leq a/w \leq 0.8$) flaws, although there remains a question regarding a practical means for measuring with lab specimens an appropriate lower-bound toughness; (2) crack initiation will not take place while $K_I$ is decreasing with time even though, as a result of a continuously decreasing temperature, $K_I \gg K_{Ic}$ (a WPS phenomenon); and (3) crack arrest will take place with $K_I$ increasing with crack depth in accordance with $K_{Ia}$ values measured in the lab with $K_I$ decreasing with crack depth. Furthermore, for the particular test conditions, which included a rather long crack jump [$\Delta a/w \approx 0.43$ ( $a = 66$ mm)], (1) crack arrest took place in accordance with the static method of analysis and (2) a very short flaw extended to become a long flaw. Although the data are not absolutely conclusive because of a lack of generality imposed by the specific test conditions, the latter two test results indicate that dynamic effects at arrest may be negligible for present-generation reactor vessels and that we must continue to be concerned with the behavior of long flaws, even though such flaws presumably have much less probability of existing than do short flaws prior to the advent of a severe thermal shock.

An LEFM analysis of the PWR-LOCA indicates that if WPS were not effective, a 2-D long axial flaw in a high-copper vessel would penetrate very deeply ($a/w > 0.9$), but we suspect that the flaw could not actually penetrate the remaining plastic ligament. This possibility was discussed at NRC Thermal Shock Review meetings several years ago, and as a result, two beam experiments were conducted. In both cases the displacement of the beam while under load was limited so that the final crack-opening angle would be the same as that calculated for a long axial flaw that extended all the way through a PWR vessel during an LOCA. Gray, Sica, and Loss[10] conducted one experiment using quenched and tempered A533 at 93°C. A similar experiment was conducted at ORNL using a quench-only heat treatment and testing at room temperature. The latter test was started with a shallow flaw, and a long crack jump was achieved with arrest taking place very close to the back surface. Gray et al. started with a deep flaw, and only a small amount of stable tearing took place. Because of the much lower toughness involved, the ORNL experiment constituted a much more severe test of the inability of the plastic ligament to be penetrated. At any rate, both experiments demonstrated this inability. An ORNL attempt to demonstrate the same inability in a thick-walled cylinder under severe thermal shock loading conditions has recently been requested.

If we assume that WPS may not be effective, the possibility exists during a PWR-LOCA of a very long crack jump that arrests close to the back surface. The long crack jump might increase the chances of a flaw penetrating the small plastic ligament; thus, if possible, an experiment designed to reveal the behavior of a very deep flaw should include a long crack jump as the mechanism for creating the very deep flaw. In accordance with agreements reached with NRC on December 17, 1980, a thermal shock experiment, designated TSE-6, will be conducted for the purpose of investigating the behavior of a flaw that jumps very deeply ($a/w > 0.8$) into the wall of a test cylinder as a result of a severe thermal shock.

Three different ways of achieving a long crack jump were considered previously,[12] and they involve a very shallow initial flaw, a blunted crack tip of just the right degree of bluntness, and a negative gradient in toughness at the inner surface. In principle these techniques can be applied; however, neither seems very practical at this time.

Another possibility for obtaining a long crack jump is to design the experiment in such a way as to achieve a negative slope for the left hand portion of the initiation and arrest critical-crack-depth curves, as illustrated in Fig. 4.13. To achieve the negative slope, $K_I/K_{Ic}$ must increase with increasing crack depth at a particular time within a time span of interest. Decreasing the wall thickness tends to increase $K_I$ with increasing crack depth and tends to reduce the increase in $K_{Ic}$ with increasing crack depth. The accompanying decrease in the severity of the thermal shock can be compensated for by increasing the $RT_{NDT}$ of the material, and this also tends to decrease $dK_{Ic}/d(a/w)$.

Figure 4.13 corresponds to imposed thermal shock conditions similar to those for TSE-5A (Ref. 12), to the heat treatment used for TSE-5 (temper at 613°C) (Ref. 13), and to a wall thickness of 76 mm. This combination of conditions can be achieved for TSE-6, and the desired calculated crack behavior for TSE-6 is apparently obtainable for this set of conditions. Starting with an initial flaw depth of ~8 mm ($a/w = 0.1$), crack initiation would take place at a time of ~1.7 min, and the crack would jump in a single event to a depth of ~72 mm ($a/w = 0.95$), leaving an uncracked ligament of only 4 mm. Warm prestressing or a $K_I$ value less than $K_{Ic}$ would prevent a second initiation event.

This calculated behavior of the very deep flaw is based on the assumption that LEFM is applicable for the deep flaw, and that is not likely to be the case. Of course, this is what TSE-6 is all about.

As shown in Fig. 4.13 by the values of $K_I/K_{Ic}$ listed along the WPS curve, the effective maximum values of $K_I/K_{Ic}$ are not very large; that is, little margin for uncertainty exists in the experiment for achieving initiation. For this reason a thicker wall (102 mm) was also considered so as to achieve a more severe thermal shock. The corresponding critical-crack-depth curves are shown in Fig. 4.14. As indicated, $K_I/K_{Ic}$ at the WPS line for a crack depth ($a/w$) of 0.1 is considerably larger than for the 76-mm wall (1.87 compared with 1.36). However, the arrest depth is less ($a/w = 0.85$ compared with 0.95), and the probability of arrest at a much shallower depth is greater ($K_I/K_{Ic} < 1$ while the crack is running). In other words, less margin for error exists for crack-jump distance, and the margin for the 76-mm wall is none too great. We concluded that the 76-mm wall would provide a better chance for a successful experiment.

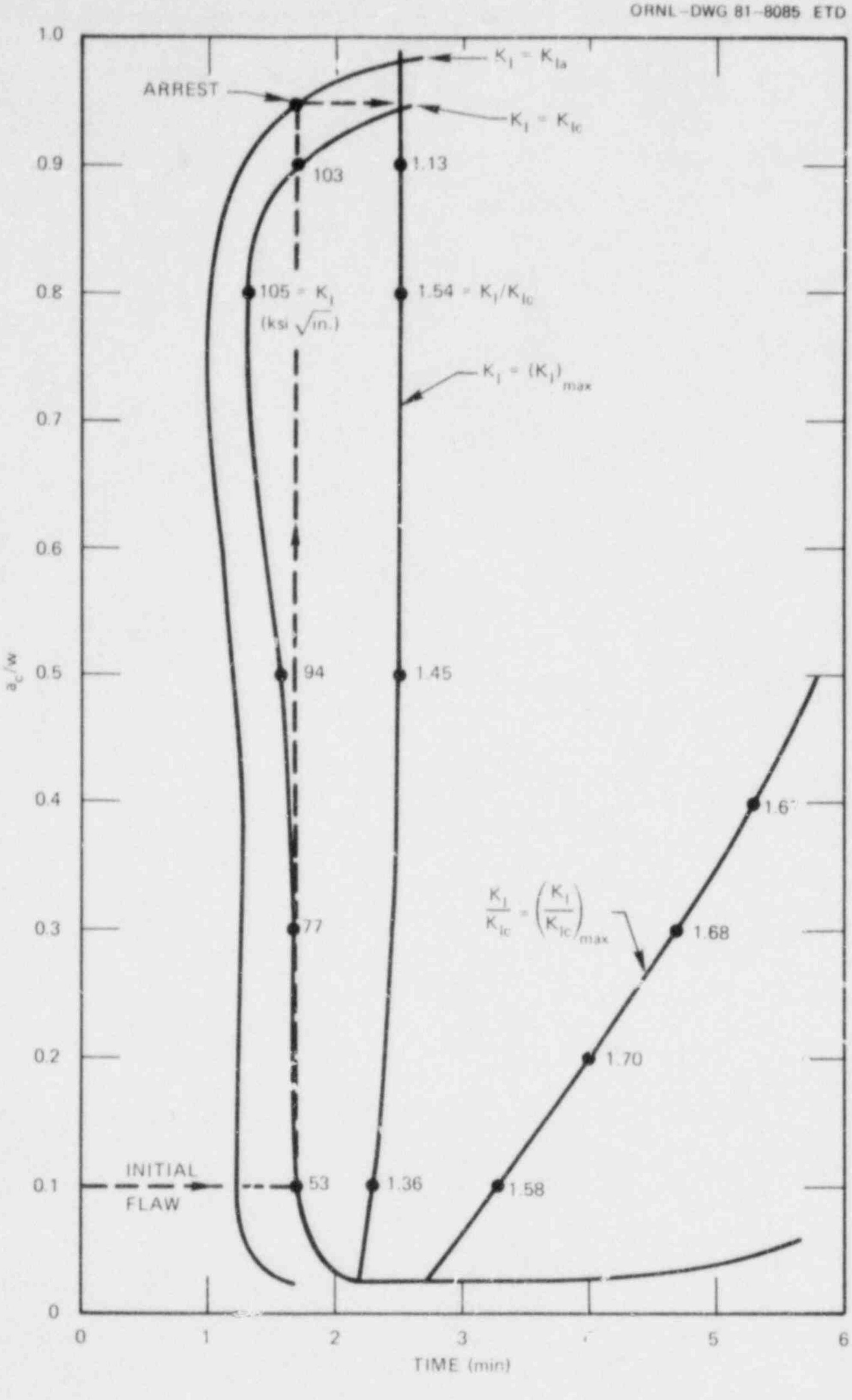

Fig. 4.13. Critical-crack-depth curves for TSE-6 with 76-mm wall.

ORNL-DWG 81-8086 ETD

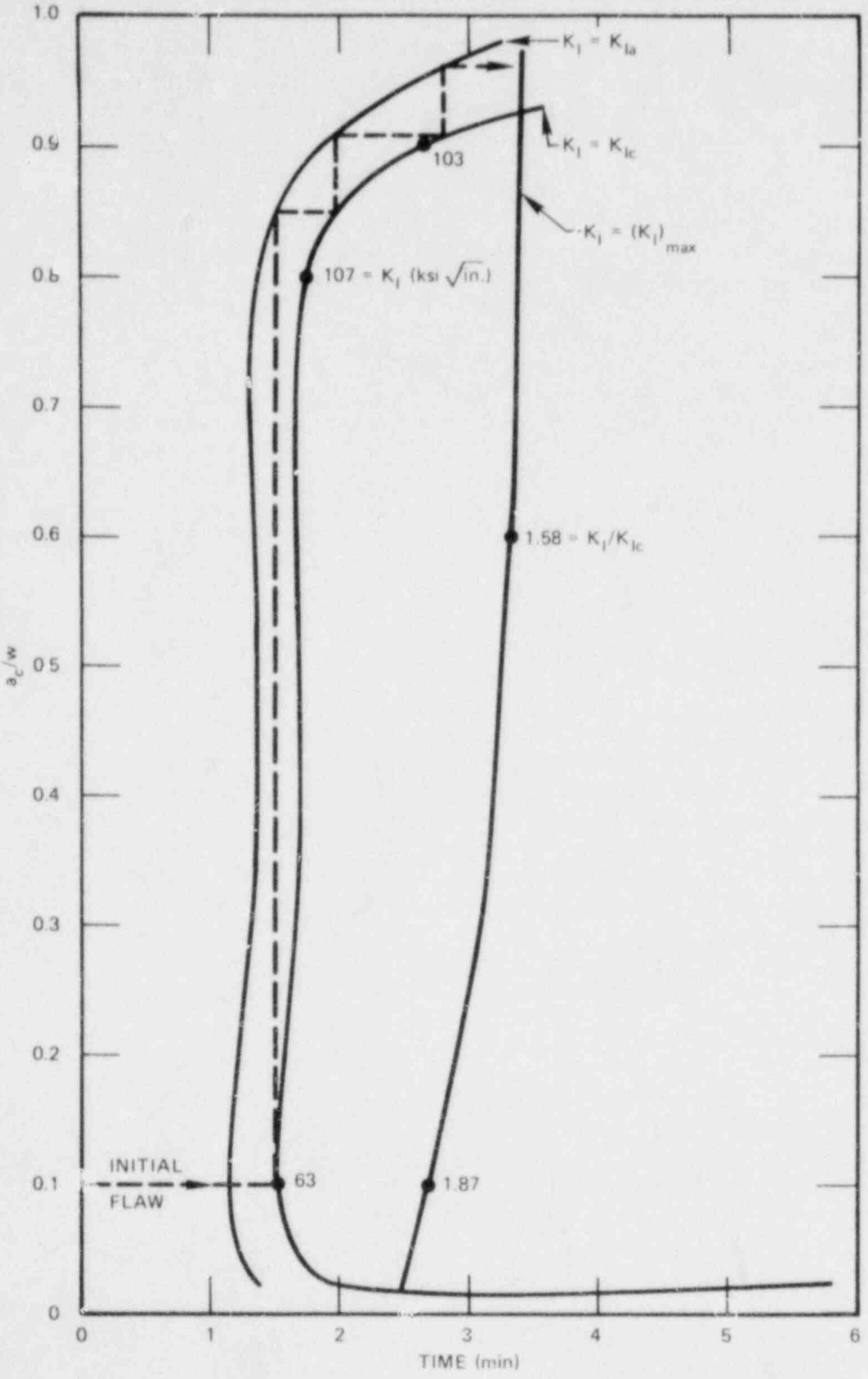

Fig. 4.14. Critical-crack-depth curves for TSE-6 with 102-mm wall.

## 4.4 Effect of Testing-System Compliance on Measured $K_J$

The results of TSE-5 (Ref. 14) and 5A (Ref. 1) and material characterization studies associated therewith indicated that large scatter (±50%) occurred in the lab 1T and 2T-CT $K_J$ data and that the long flaws in the thermal shock test cylinders behaved in accordance with the lower bound of the lab data. Generally speaking, the large scatter in $K_J$ was accompanied by variations in the amount of stable tearing prior to brittle fracture; the greater the amount of stable tearing the larger $K_J$, and the lowest values of $K_J$ were essentially valid and were associated with effectively zero stable tearing. An effort has been made to explain this behavior and to examine the possible effect of loading compliance on the $K_J$ value using rather simple models. This information was originally discussed in a series of three letters[15-17] and is summarized below.

A possible reason for specimen-to-specimen variation was suggested by Landes and Shaffer[18] and is based on the hypothesized existence of low-toughness sites. If a low-toughness site were located on the crack front, as shown in Fig. 4.15, and if the effective toughness ($K_s$) of the site were $\geq K_{Ia}$, then perhaps a CT specimen would fail with $K_I = K_{Ic} \geq K_{Ia}$, and no stable tearing would occur. If, on the other hand, a low-toughness site did not exist on the crack front but one did exist some distance from the crack front, stable tearing would extend the crack tip to the low-toughness site, and this site would trigger fast fracture. Thus, depending on the proximity of the site to the crack front, $K_J \geq K_{Ia}$, the farther away the site the greater $K_J$. Landes argued that the longer the crack front (the bigger the lab specimen) the greater the probability of having a low-toughness site on the crack front, and the greater the probability of lower-bound behavior. The crack fronts for TSE-5 and -5A were 1220 mm long, and 250 mm of crack front was tested in the lab (ten 1T-CT specimens) at each of several temperatures; the lower bound of the lab data agreed reasonably well with the toughness data deduced from the thermal shock experiments.

The suggestion has been made that $K_{Ic}$ based on $J_{Ic}$ might represent the lower bound. However, if low-toughness sites do exist and if $K_s \geq K_{Ia}$, then $K_{Ic} \geq K_{Ia} < J_{Ic}$. This fact implies that stable tearing would

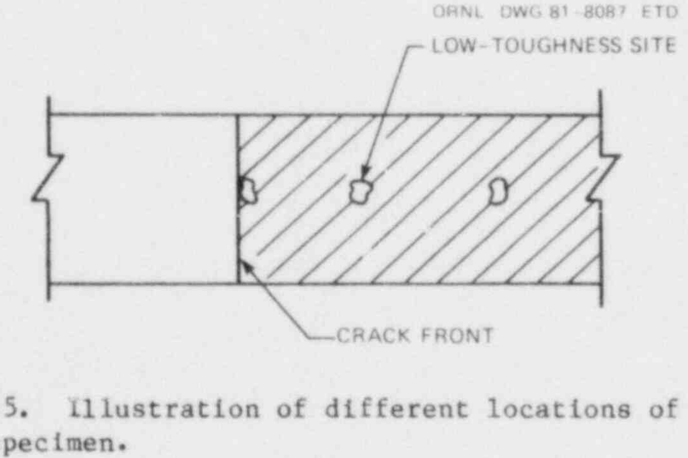

Fig. 4.15. Illustration of different locations of low-toughness sites in CT specimen.

not necessarily precede fast fracture, or that fast fracture would be coincident with the onset of stable tearing (we recognize that the onset of stable tearing is not well-defined). Thus, extrapolation back to zero stable tearing would not necessarily yield the lower-bound toughness associated with long flaws.

The suggestion has also been made recently that lower-bound toughness values, or at least a substantial reduction in scatter, might be consistently obtained with lab specimens by increasing the compliance of the testing machine. Presumably this assumption was based on the hypothesis[19,20] that an appropriate compliance would result in tearing instability and that rate effects associated with tearing instability would result in early fracture-mode conversion (ductile to brittle fracture), thus reducing the J-integral. Another suggestion was made, based on the same reasoning, that the lower-bound behavior in TSE-5 and -5A could be attributed to the large compliance of the test cylinders.

Paris et al.[19] and Ernst et al.[20] concluded that tearing instability could occur if the machine-plus-specimen compliance were great enough, that is, if $T_{applied} \geq T_{material}$, where T is the tearing modulus. This conclusion is easy enough to understand by simply considering a load-displacement diagram such as that in Fig. 4.16, which corresponds to a

ORNL DWG 81 8088 ETD

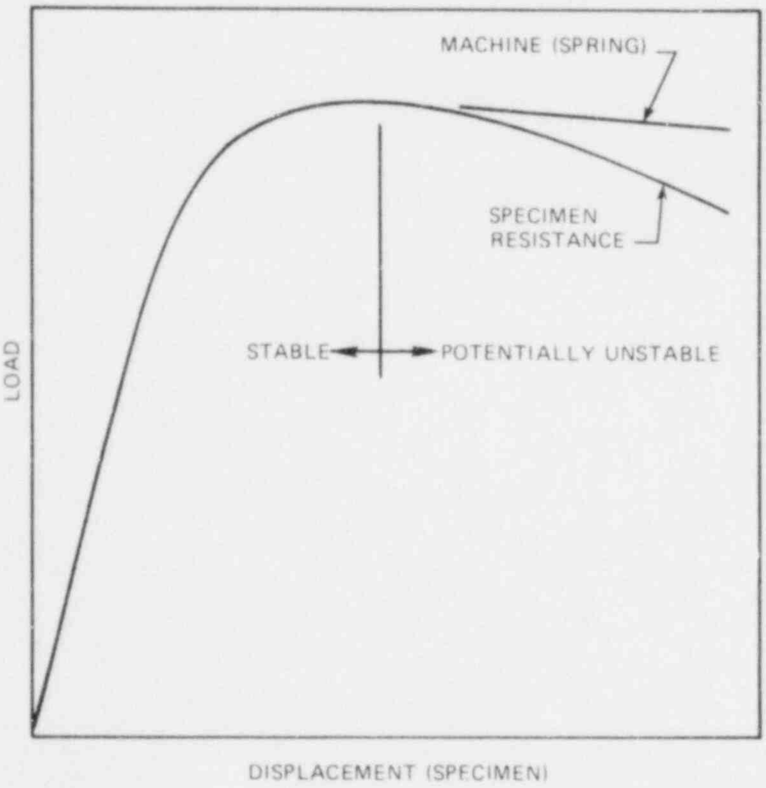

Fig. 4.16. Load-displacement diagram illustrating difference in specimen resistance and machine capability for static loading (displacement control).

displacement-controlled test. The eventual decrease in specimen load shown in the figure is the result of a decrease in the load capacity of the specimen beyond a certain critical displacement. If the spring constant of the machine is such that the applied load cannot decrease as much as the load capacity of the specimen, an instability occurs; that is, the otherwise unbalanced force accelerates the movable components and rips the specimen apart. For this to happen, the spring constant of the machine must be less than the slope of the specimen load-displacement curve. Quite obviously this situation cannot exist to the left of maximum load; an instability cannot occur with the specimen load increasing. Ernst[20] arrived at the same conclusion.

The inability to achieve instability to the left of maximum load is very important, because with few exceptions the 1T- and 2T-CT specimens used to characterize the TSE-5 and -5A test cylinders underwent fast fracture prior to maximum load. Thus, if the increase in load is truly continuous, tearing instability and an early mode conversion associated therewith could not occur.

Tests have been conducted by Paris et al.[21] and Gudas and Joyce[22] that indicate that for the potentially unstable situation (load capacity decreasing with displacement), tearing instability brought about by including a spring in series with the test specimen resulted in early mode conversion very close to maximum load, as would be expected. A more recent experiment conducted by Gudas[23] indicated mode conversion with the spring installed and with the load still increasing. However, one should not hasten to conclude that this occurrence had anything to do with tearing instability, which, based on the simple model just described, should not have occurred. The large scatter encountered in our material-characterization studies would account for such an occurrence without the spring.

A review of the load-displacement plots for the TSE-5A material-characterization studies indicates that all ten 1T-CT specimens tested at 125°F failed at or after maximum load, and the scatter was only ±11%. For a testing temperature of 100°F, three of six specimens failed after maximum load, and the scatter was ±13%. At 75°F only three of ten specimens broke at or after maximum load, and the scatter was ±31%. For testing temperatures of 25 and −25°F no failures occurred after maximum load, and the scatter among ten specimens was ±40 and ±30%, respectively.

The scatter reported for each of the above cases is relative to the average values, but because we are primarily interested in the lower-bound, a more meaningful comparison is that of the average with the lower bound, if we assume that the average is the more probable value measured in the lab. For the above cases the averages are 13, 14, 45, 67, and 43% above the minimum values. If one further assumes that the $K_{Ic}$ values deduced from TSE-5A are the lower-bound toughness values that we might eventually measure in the lab, then the above variations are even greater.

For TSE-5, only 2 out of 33 specimens broke beyond maximum load, and these were at the highest test temperature (180°F). The scatter in the data were ±40, ±52, and ±47% for testing temperatures of 180, 90, and 0°F.

Apparently, then, relatively few of the lab specimens broke beyond maximum load, and they did so only at the higher test temperatures. Thus, introducing tearing instability presumably would not have much effect on the overall results of the material-characterization studies for TSE-5 and -5A.

Along these same lines another point should be made concerning the scatter in the TSE-5 and -5A material-characterization data. All J-integrals were evaluated on the basis of maximum load, even for those few cases where fracture took place after maximum load. Thus, even if the inclusion of a spring resulted in fast fracture at maximum load for these latter cases, the J-integrals would be no different than already calculated, and the scatter would remain the same.

Another point of interest in connection with our lab testing is that load control (load ramp rate) was used. Depending on the acceleration and speed capability of the testing machine, these tests could have been subject to rate effects similar to those provided by a spring. Had displacement control been used, there might have been a greater drop-off in load prior to fracture for those specimens that fractured after maximum load, and perhaps fracture-mode conversion for these same cases would not have taken place. However, if the rate effect did not affect maximum load, the J-integrals would have been essentially the same, because the integrals were based on maximum load.

Based on this simplified approach to understanding the possible effects of conducting lab tests with greater machine compliance, the scatter in our data for TSE-5 and -5A would appear unlikely to be reduced by increasing the machine compliance.

During recent tests$^{24}$ with compact-tension specimens, smaller J-integrals (less stable crack growth) were obtained with a spring in series with the specimen than were obtained without the spring, and some of these fractures occurred below maximum load. The results indicate that the spring may have induced fracture-mode conversion at a lower load than that experienced without the spring. This fact also implies that the spring caused a mechanical instability resulting in accelerated failure and therefore a rate effect that caused the mode conversion. However, if the simple model described here is appropriate, the mechanical instability could not take place with or without the spring, and another explanation must exist for the results obtained.

One explanation, of course, is that scatter in the data accounts for what was observed. Based on our lab data for TSE-5 and -5A, this explanation is quite possible. However, another interesting possibility exists, as described below.

Once again the assumption will be made that the load-deflection curve is as shown in Fig. 4.16. Thus, as before, mechanical instability cannot occur to the left of maximum load, regardless of the compliance of the machine. However, the addition of a spring can be shown to result in a lower <u>observed</u> value of fracture toughness.

In Fig. 4.17 another curve has been added to that in Fig. 4.16. This added curve represents the load ($P_a$) required to produce $K_I = K_{Ia}$. This curve has a slight negative slope to account for extension of the flaw as a result of stable tearing. Now, suppose that a low-toughness site exists close to the crack front with an effective toughness less than $K_{Ia}$. When the load reaches the corresponding value (point <u>a</u> in Fig. 4.17), initiation will occur. A short crack jump will occur that is limited by the size of the low-toughness site. A corresponding decrease in load will also occur, the amount depending on the system compliance and the distance

ORNL-DWG 81-8089 ETD

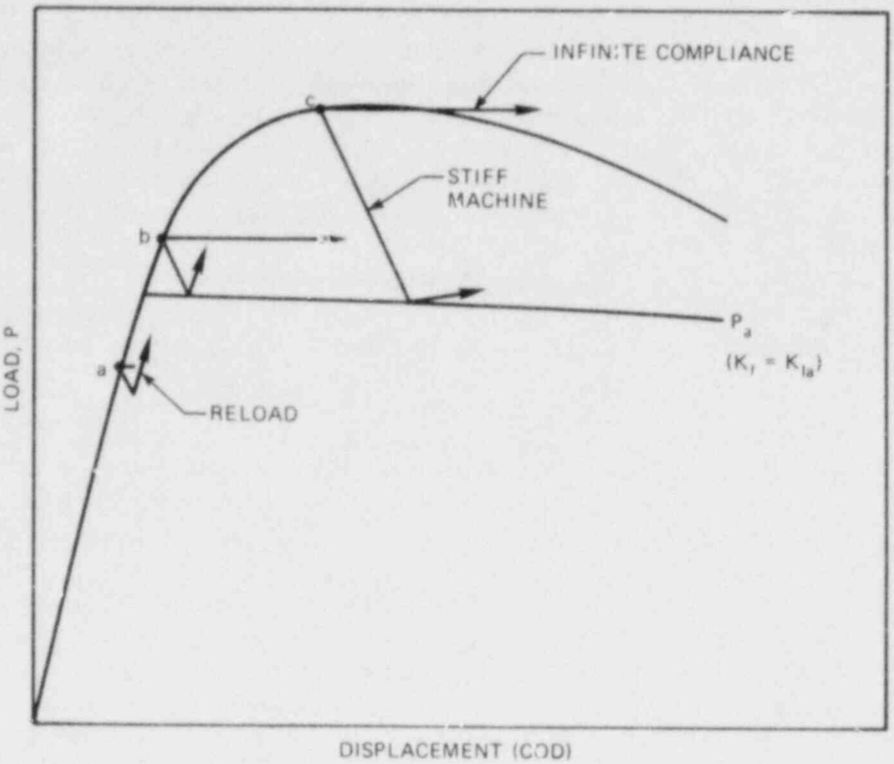

Fig. 4.17. Load-displacement diagram (CT specimen) indicating possible effects of adding a spring in series with the specimen.

that the crack jumps. If the compliance is very large, very little drop in the load will occur, but arrest will still take place after the same crack jump distance because the load is less than that associated with $K_{Ia}$. (If the compliance is very small, arrest might take place within the low-toughness site.) Because the head of the machine is moving continuously, the specimen will reload. Note that stable tearing may have preceded initiation, and that the fast (brittle) fracture took place without an instability and irrespective of what the system compliance may have been. "Pop-ins" such as these have been observed but their cause has not been identified.

Now suppose that the toughness of the low-toughness site is only slightly greater than $K_{Ia}$ or that it is less than this value and the low-toughness site is intercepted as a result of stable tearing as the load just exceeds that corresponding to $K_I = K_{Ia}$ (point b in Fig. 4.17). Once again initiation will occur independent of the system compliance and not as a result of a mechanical instability. The crack-jump distance will be independent of the size of the low-toughness site and will be sufficient to drop the load to correspond with $K_I = K_{Ia}$. The corresponding required crack-jump distance is dependent on the system compliance; the greater the compliance, the greater the crack-jump distance. But note once again that compliance had nothing to do with mode conversion (initiation). The important point is that if the compliance is very small, so is the crack-jump distance and drop in load, and as a result the event might go unnoticed (reloading follows arrest). Thus, in a stiff machine a range of critical loads could exist within which initiation would not be detected as such. However, if the system compliance is large, the crack-jump distance and load drop will be large enough to be detected, and the event will be interpreted as crack initiation (such as point c). Note that if the compliance were very large, the specimen surely would fail completely, and the minimum detectable critical load would correspond to $K_I = K_{Ia}$.

Suppose that all specimens tested in a stiff machine would experience a pop-in at a load corresponding to $K_I = K_{Ia}$ (but crack initiation would not be identified as such until a much higher load was achieved) and that the critical load (and corresponding amount of stable tearing) so defined was a function of the proximity of the low-toughness site to the crack front. If the system compliance were increased to a very high value, all critical loads would be equal to that corresponding to $K_I = K_{Ia}$; that is, $K_{Ic} = K_{Ia}$. Of course this particular equality is not necessary to illustrate the point that an increase in system compliance would in this hypothetical case result in a single and relatively low value of $K_{Ic}$.

Generally speaking, suppose that not all specimens in a stiff machine experience a pop-in at the same load and after the same amount of stable tearing because of variations in the effective toughness of the low-toughness site and/or because of variations in the proximity of the low-toughness site to the crack front. In this case increasing the compliance of the system would reduce some of the critical loads but not all of them.

The suggestion has been made that the actual load-displacement curve may not be a smooth curve as indicated in Fig. 4.17 but rather a series of initiation arrest events; that is, stable tearing may not be a continuous process. Under these circumstances, what are the chances of a mechanical instability on the "rising" portion of the load-displacement curve? The situation appears to be essentially the same as that discussed above, except that in a stiff machine the crack-jump distances are small for all but the final initiation event, even when the load is considerably greater than that corresponding to the nominal $K_{Ia}$. In other words, the effective values of $K_{Ic}$ and $K_{Ia}$ for each of the many initiation-arrest events would have to increase within increasing load (number of events). Consistent with the previous reasoning, an increase in compliance would increase the crack-jump distance for each initiation-arrest event but would not promote mechanical instability or fracture-mode conversion. However, it could promote detectable failure of the specimen at a lower load. Thus, this case is essentially the same as the one above in which the assumption was made that a low-toughness site would always result in a pop-in at a load just above that corresponding to $K_I = K_{Ia}$.

Note that inertia in the spring could prevent critical loads close to $P_a$ from being detected. Suppose that a pop-in occurs at a load just above $P_a$. The inertia in the spring might allow enough unloading for the crack to arrest after only a short jump. The spring load would eventually catch up, but reinitiation would not take place immediately if there were not a low-toughness site of appropriate toughness on the new crack front.

A summary of the discussion thus far follows:

1. In a stiff machine, critical loads close to $P_a$ may not be detected.
2. On the rising portion of the load-displacement curve, the addition of a spring in series with the test specimen will not result in mechanical instability and therefore will not bring about fracture-mode conversion.
3. However, if the machine compliance is increased, lower critical loads will be detected.
4. The possibility exists that the minimum critical load is equal to $P_a$ ($K_{Ic} = K_{Ia}$).

During the TSE-5 posttest material characterization study, $K_{Ic}$ values as low as $K_{Ja}$ were measured with one 1T-CT specimen and one 2T-CT specimen in a stiff machine using load control. That the load-control feature influenced the measurement is unlikely, and according to the previous arguments a critical load close to $P_a$ would not be detectable in a stiff machine. These two low values are probably the result of toughness variations in the material surrounding the low-toughness sites.

In view of all this evidence, why does a long flaw in a thick-walled cylinder subjected to severe thermal shock behave in accordance with lower-bound toughness, where lower-bound refers to the lowest of the lab $K_J$ data obtained in a stiff machine (reference is made to TSE-5 and -5A)? First of all, because the flaw is quite long relative to that in a lab specimen the chances of a low-toughness site existing on the original crack front are greater. The second point is that the cylinder has a high degree of compliance; in fact, a cylinder subjected to thermal loadings has essentially infinite compliance; thus, in the absence of inertial effects it has the capability of resulting in $K_{Ic}$ values as low as $K_{Ia}$.

Based on the simple models shown in Figs. 4.15 through 4.17, an explanation does exist for the low-toughness values deduced from TSE-5 and -5A as well as a means for reducing some but not necessarily all of the $K_J$ values measured with 1T and 2T-CT specimens in the lab.

## 4.5 Thermal Shock Materials Characterization

W. J. Stelzman D. A. Canonico

The results from CA-oriented* CVN specimens have been reported.[25] The specimens had been machined from the thermal shock vessel TSC-2 prolongation (TSP-2) after tempering for 4 h at 679°C and air cooling and were used to determine the $RT_{NDT}$. At that time the maximum test temperature was 79°C. Since then we have obtained additional results from CA-oriented CVN specimens further defining the transition regime and upper-shelf energies up to 288°C. All of the results are presented in

---

*The direction of loading is circumferential; the direction of fracture propagation is axial.

Fig. 4.18. We also tested a limited number of CT-oriented specimens[26] to relate the axial fracture results with through-thickness fracture results. The results from the CT-oriented specimens are presented in Fig. 4.18. All fell within the scatter band of the CA-oriented results.

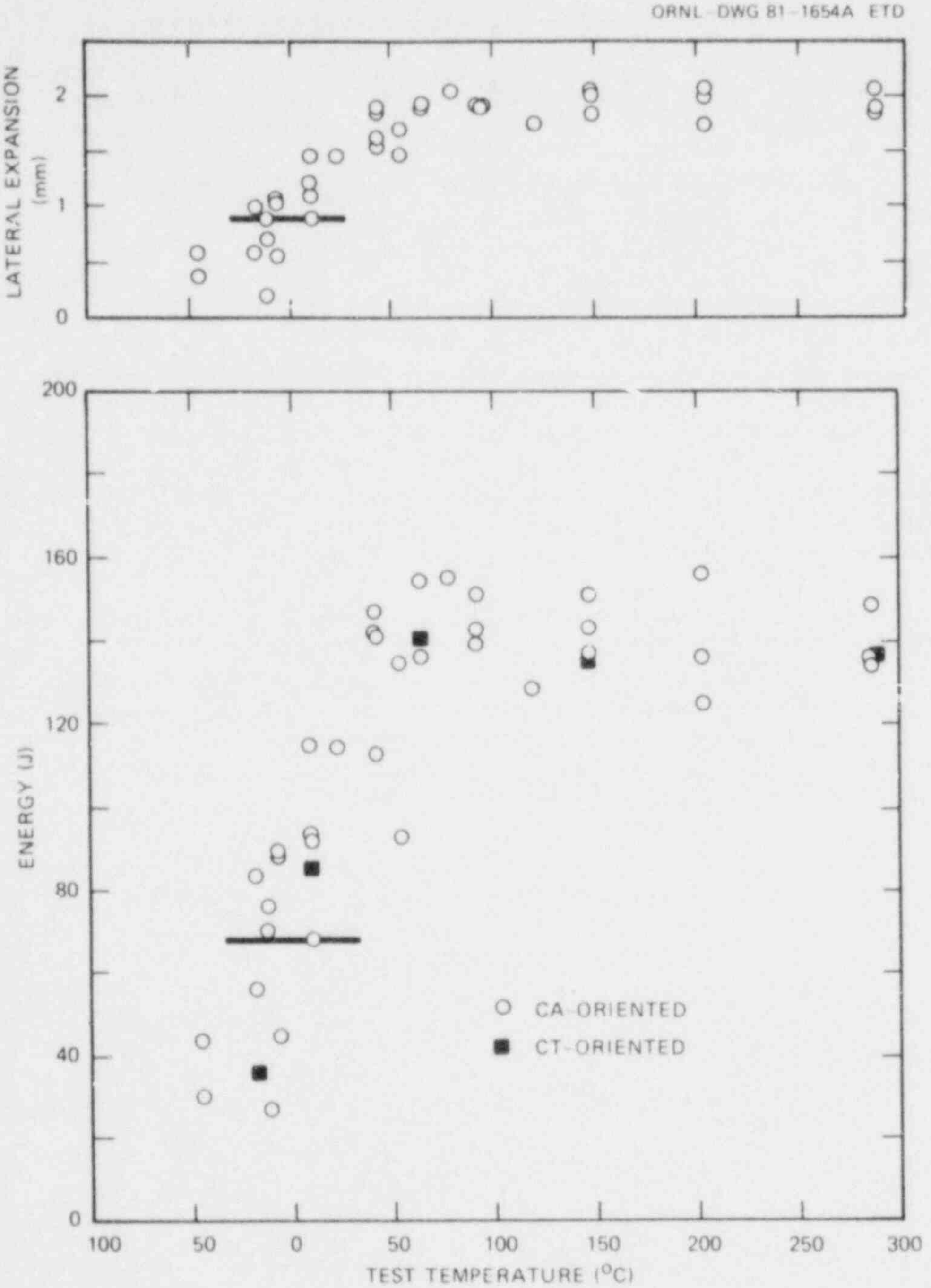

Fig. 4.18. Charpy V-notch impact properties of "as-quenched" prolongation TSP-2 (SA-508) after tempering at 678°C for 4 h and cooling in air.

## References

1. R. D. Cheverton, "Thermal Shock Investigations," *Heavy-Section Steel Technology Program Quart. Prog. Rep. October–December 1980*, NUREG-CR-1941 (ORNL/NUREG/TM-437), pp. 37–54.

2. H. S. Carslaw and J. C. Jaeger, *Conduction of Heat in Solids*, 2d ed., p. 17, Oxford at the Clarendon Press, London, 1959.

3. S. Timoshenko, *Strength of Materials*, Part II, 2d ed., D. Van Nostrand, New York, 1951.

4. *Flaw Evaluation Procedures*; ASME Section XI, EPRI NP-719-SR, August 1978.

5. U.S. Nuclear Regulatory Commission, "Effects of Residual Elements on Predicted Radiation Damage to Reactor Vessel Materials," *Regulatory Guide 1.99*, Rev. 1 (Sept. 16, 1976).

6. H. F. Bueckner, "A Novel Principle for the Computation of Stress Intensity Factors, *Z. Angew. Math. Mech. 50*, 529–546 (1970).

7. S. K. Iskander, *Two Finite-Element Techniques for Computing Model Stress Intensity Factors in Two- and Three-Dimensional Problems*, ORNL/NUREG/CSD/TM-14 (1981).

8. W. D. Turner et al., *HEATING5 — A IBM 360 Heat Conduction Program*, ORNL/CSD/TM-15 (1977).

9. S. K. Iskander, *The Calculation of Stress Intensity Factors in Thick Cylinders Subjected to Transient Temperature Gradients by the Finite-Element Method*, K/CSD/TM-2, Oak Ridge Gaseous Diffusion Plant (April 1976).

10. R. A. Gray, Jr., G. Sica, and F. J. Loss, *Plastic Net Ligament Studies, Structural Integrity of Water Reactor Pressure Boundary Components*, NRL/NUREG-3512, p. 40 (May 1977).

11. R. D. Cheverton, "Thermal Shock Investigations," *Heavy-Section Steel Technology Program Quart. Prog. Rep. July–September 1978*, NUREG/CR-0476 (ORNL/NUREG/TM-275), pp. 82–85.

12. R. D. Cheverton, "Thermal Shock Investigations," *Heavy-Section Steel Technology Program Quart. Prog. Rep. July–September 1980*, NUREG/CR-1806 (ORNL/NUREG/TM-419), p. 46.

13. W. J. Stelzman and D. A. Canonico, "Thermal Shock Material Characterization," *Heavy-Section Steel Technology Program Quart. Prog. Rep. April–June 1980*, NUREG/CR-1627 (ORNL/NUREG/TM-401), pp. 42–44.

14. R. D. Cheverton, "Thermal Shock Investigations," *Heavy-Section Steel Technology Program Quart. Prog. Rep. January–March 1980*, NUREG/CR-1477 (ORNL/NUREG/TM-393), pp. 19–20.

15. R. D. Cheverton, ORNL, personal communication to D. A. Canonico, Jan. 15, 1980.

16. Letter from R. D. Cheverton to distribution, Nov. 19, 1980; Subject: Tearing Instability and Mode Conversion As Related to Lower-Bound Toughness.

17. Letter from R. D. Cheverton to Milton Vagins, Feb. 17, 1981; Subject: Tearing Instability and Fracture-Mode Conversion as Related to Lower-Bound Toughness.

18. J. D. Landes and D. H. Shaffer, *Statistical Characterization of Fracture in the Transition Region*, Westinghouse Scientific Paper 79-ID3-JINTF-P4 (June 8, 1979).

19. P. C. Paris et al., *Instability of the Tearing Mode of Elastic-Plastic Crack Growth*, ASTM STP 668, pp. 5–36 (March 1979).

20. H. A. Ernst et al., *Estimations of J-Integral and Tearing Modulus T from a Single-Specimen Test Record*, Westinghouse Scientific Paper 80-ID3-JINTF-P3 (May 2, 1980).

21. P. C. Paris et al., *An Initial Experimental Investigation of the Tearing Instability Theory*, ASTM STP 668, pp. 251–265 (March 1980).

22. J. P. Gudas and J. A. Joyce, "Validation of Tearing Instability on Degraded LWR Piping," Nuclear Regulatory Commission Eighth Water Reactor Safety Research Information Meeting, Gaithersburg, Maryland, Oct. 30, 1980.

23. G. D. Whitman, University of Maryland, personal communication to R. D. Cheverton, ORNL, Nov. 3, 1980.

24. G. R. Irwin et al., University of Maryland, personal communication to R. D. Cheverton, ORNL, Feb. 2, 1981.

25. W. J. Stelzman and D. A. Canonico, "Thermal Shock Materials Characterization," *Heavy-Section Steel Technology Program Quart. Prog. Rep. October–December 1980*, NUREG/CR-1941 (ORNL/NUREG/TM-437), pp. 50–54.

26. W. J. Stelzman and D. A. Canonico, "Thermal Shock — Temper Study," *Heavy-Section Steel Technology Program Quart. Prog. Rep. January–March 1979*, NUREG/CR-0818 (ORNL/NUREG/TM-324), p. 107.

# 5. PRESSURE VESSEL INVESTIGATIONS

## 5.1 Intermediate Test Vessel V-8A

P. P. Holz R. H. Bryan

Intermediate test vessel V-8 is being repaired and prepared for a test (V-8A) in which flaw behavior in low-upper-shelf material will be investigated at upper-shelf temperature. The test program is expected to reveal the modes of flaw growth and to test the capabilities of elastic-plastic fracture mechanics in predicting flaw behavior.

In Phase I of a subcontract with The Babcock and Wilcox Company (B&W), welding procedures for placing a special seam weld in the vessel were developed. In Phase II, B&W is repairing the vessel and making several welds of the special material, including the vessel seam. In Phase III, B&W will perform mechanical property and fracture toughness tests, including J-integral tests on material from the welds, and will document all phases of the work.

During the quarter, B&W completed all work under the subcontract for Phase I, and UCC—ND granted approval for B&W to start work under a new subcontract for Phases II and III. In the next section, the final data developed by B&W in Phase I are discussed.

### 5.1.1 Trial weld results

In previous reports[1,2] the selection of a weld wire, flux, and heat treatment combination was described, and preliminary results of the final trial of the selected combination were reported. During this quarter, tests by B&W in Phase I were completed, and all data were reported.

Results of this development agreed well with expectations, as indicated by the following comparison of specified and measured properties of the trial weld (B&W weld V8-42):[3]

| Property | Specified acceptable value | Measured value |
|---|---|---|
| Impact energy on upper shelf, J | | |
| Range | 47—75 | 50.8—63.7 |
| Average | | 56.9 |
| Yield strength at RT, MPa | | |
| Range | 448—621 | 456—466 |
| Average | | 460 |

Charpy V-notch impact tests were conducted to define the onset of the upper shelf. The Charpy results for the trial weld are presented in

Fig. 5.1. On the basis of 100% shear fracture appearance, the upper shelf begins at ~100°C.

The J-integral tests were performed at ~120°C, which is approximately the expected vessel test temperature. Three 20% side-grooved IT compact specimens were tested satisfactorily by the unloading compliance method. An irregular fatigue crack in the fourth specimen led to anomalous results near initial tearing. The data in terms of J vs Δa (crack extension) for the three good tests are shown in Fig. 5.2. The values presented have been corrected for Δa and rotation effects. The $J_{Ic}$ values determined are

| Specimen | Test temperature (°C) | $J_{Ic}$ (kJ/m$^2$) |
|---|---|---|
| V842J1 | 121 | 65.6 |
| V842J2 | 121 | 65.1 |
| V842J3 | 116 | 70.5 |

Power law parameters C and n in the expression for J,

$$J = C(\Delta a)^n \ , \tag{5.1}$$

were determined from the B&W data by least-squares fit to the linear logarithmic form of Eq. (5.1),

$$\ln J = n \ln(\Delta a) + \ln C \ , \tag{5.2}$$

for various ranges of crack extension Δa. Results are summarized in Table 5.1. Note that the power law expression fitting the full range of

Table 5.1. Power-law parameters n and C from least-squares fit of J-Δa data from B&W weld V8-42 with J considered as a random variable

| Specimen | Δa range (mm) | n | C [kJ·m$^{-2}$/(mm)$^n$] |
|---|---|---|---|
| J1 | 0.282–1.509[a] | 0.3687 | 114.10 |
| J2 | 0.278–1.713[a] | 0.3692 | 109.83 |
| J3 | 0.246–1.642[a] | 0.3606 | 120.26 |
| J1 | 0.282–13.193 | 0.2687 | 111.06 |
| J2 | 0.278–12.380 | 0.2948 | 108.73 |
| J3 | 0.246– 8.753 | 0.2824 | 115.95 |

[a] Exclusion range for $J_{Ic}$ determination.

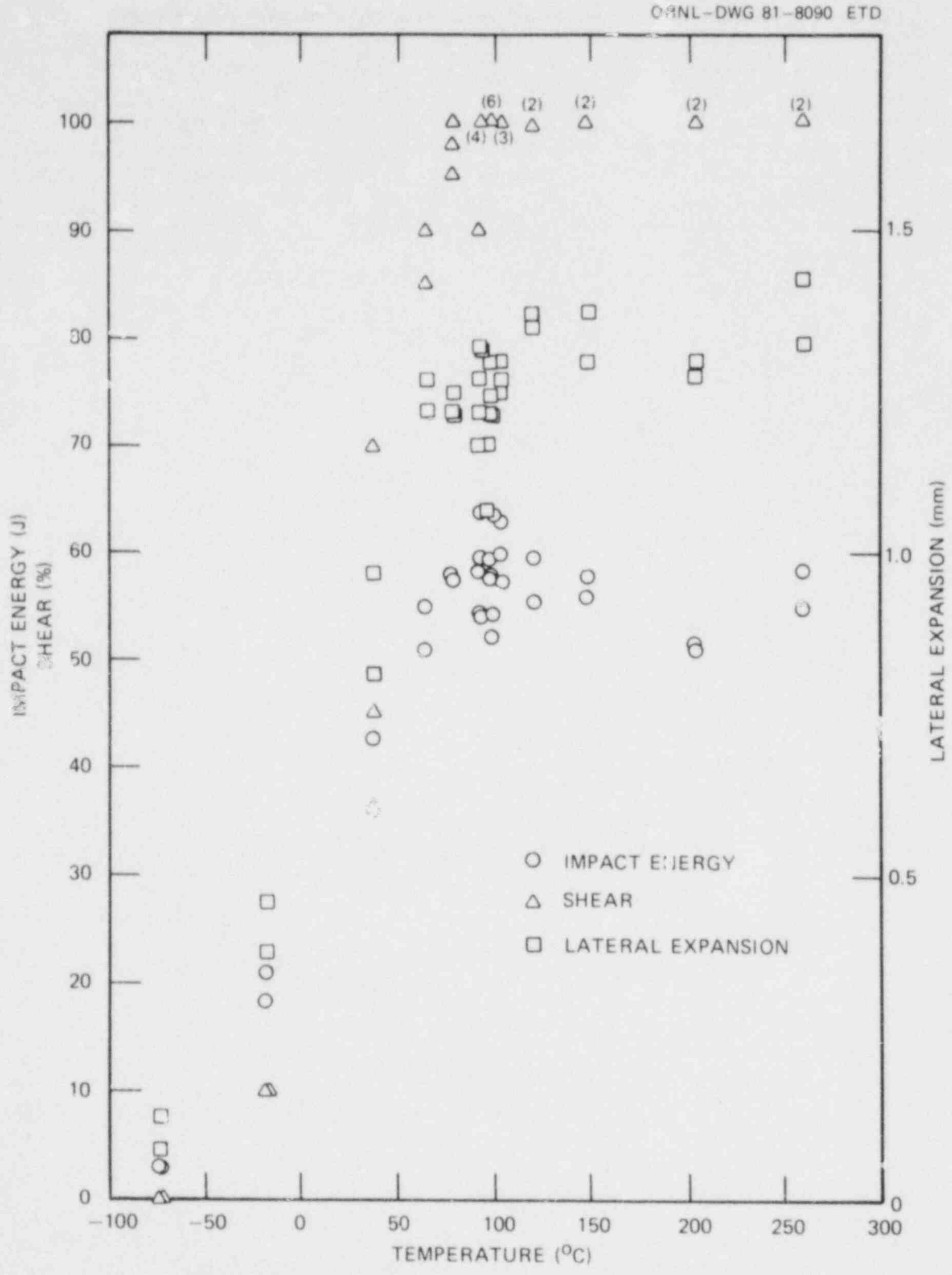

Fig. 5.1. Charpy V-notch impact test data for B&W trial weld V8-42.

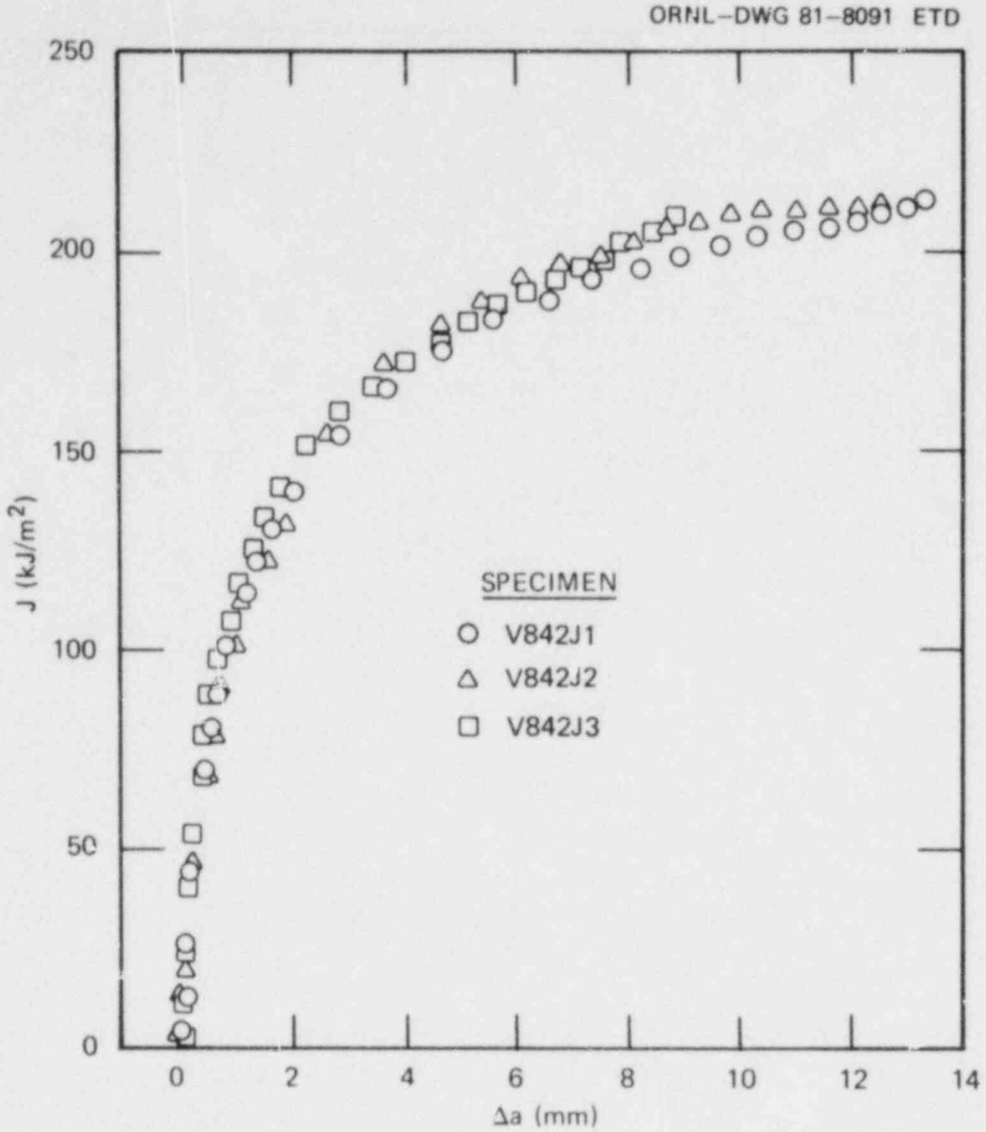

Fig. 5.2. J-integral resistance curve data from three unloading compliance tests of IT compact specimens of B&W trial weld V8-42.

data is flatter than the expression based on exclusion range data alone, as indicated by the smaller values of n. This illustrates the substantial error that could result from using J data from a limited range for estimating behavior at larger values of Δa.

Upper-shelf toughness of the trial weld is similar to that of irradiated high-copper submerged-arc welds, which the special weld in vessel V-8A is supposed to simulate. A typical J-Δa curve from the trial weld data is shown in Fig. 5.3, superimposed on data for the irradiated welds from F. J. Loss of the Naval Research Laboratory.[4]

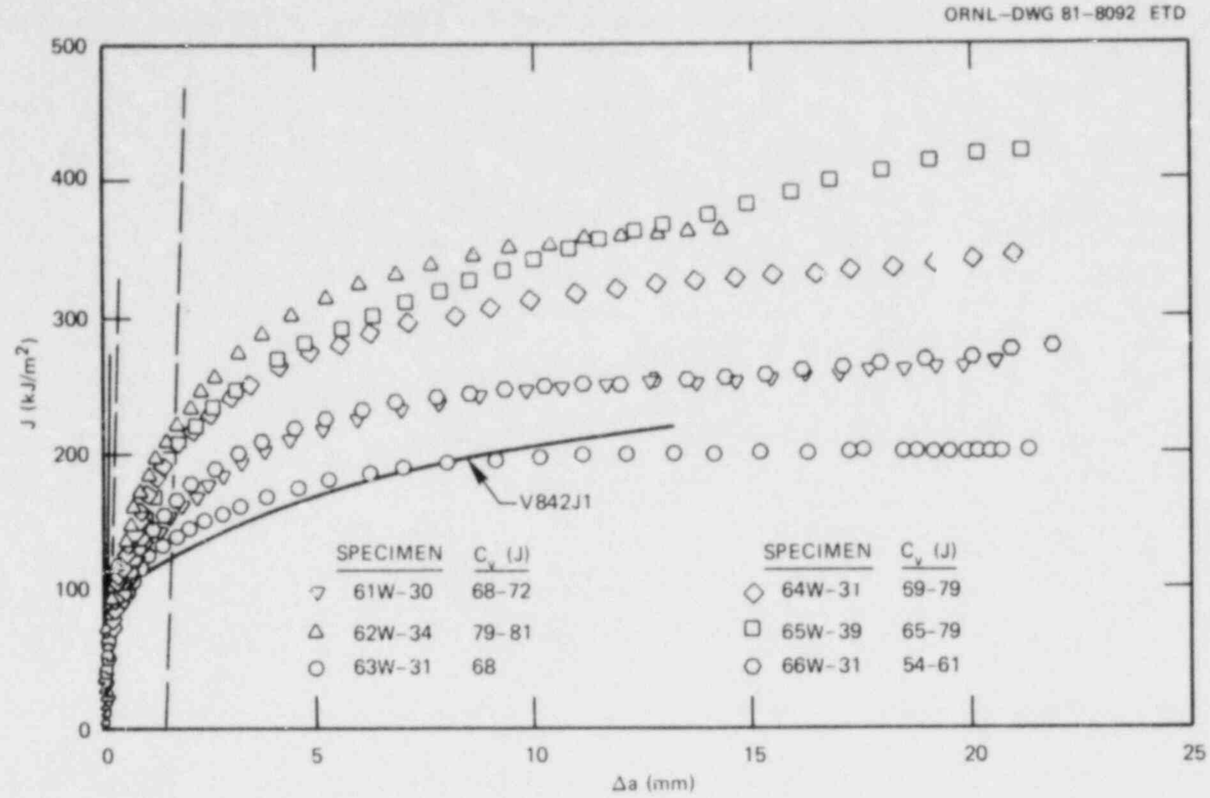

Fig. 5.3. Comparison of power low curve fit to J-R data from B&W trial weld V8-42 with results of tests of 1.6T compact specimens of irradiated welds. Data from Loss.

### 5.1.2 Vessel repair and weld preparation

Phase II work by B&W includes:

1. making a flawing practice weld to use in establishing cyclic pump flawing procedures and to check out flawing techniques in the special type weldment,
2. placing four special automatic-submerged arc (ASA) seam welds in vessel prolongation V-10 for specimen stock for mechanical property and other tests and reporting initial test results,
3. welding vessel V-8 which involves

    a. a manual metal-arc plug weld to close the cavity in the vessel left by the removal of the vessel's first test zone,
    b. an ASA special seam weld,
    c. closure fit and leak tests.

Phase III work by B&W includes making specimens for numerous additional mechanical property and other tests, including J-integral tests to fully characterize the special ASA seam weldment. Phase III work also includes a full documentary report on all phases of the work.

### 5.1.3 Vessel test preparations

Graphite has been selected as ballast for reducing the volume of the pressurizing fluid for the V-8A test, a measure designed to limit the stored energy of the fluid at test temperatures above 100°C. Studies of instrumentation and ballast installation procedures are under way. Work has started on a one-fifth plexiglass model of an intermediate pressure vessel graphite ballast arrangement. The model will serve to develop means of securing the graphite, loading and unloading schemes, proper clearance requirements, and routing for all internal vessel instrumentation.

## 5.2 Pressurized Thermal Shock Studies

R. H. Bryan G. C. Robinson

### 5.2.1 Background

One of the original objectives of vessel testing in the HSST program was to demonstrate a capability to predict failure of a full-size reactor pressure vessel having crack-like flaws. In many respects, this objective has been fulfilled by the series of intermediate vessel tests already performed with pressure loading alone or a combination of pressure loading and residual stress. Indeed, for pressure alone the tests generally demonstrated a remarkable vessel capacity to sustain overloads in the presence of large flaws. Furthermore, modes of fracture, their dependence on the toughness transition, and applicability of methods of fracture analysis were determined or illuminated by these tests on a realistic scale.

To resolve the more important questions on pressure vessel integrity initially and to pursue other objectives logically, the simplest tests were performed first. To obtain the maximum experimental information, each test was usually taken to the point of vessel failure. Test conditions were chosen to be as realistic as practical. However, intermediate vessel tests were generally fracture tests on a realistic scale rather than simulations of specific reactor vessel conditions.

This testing policy has produced useful results. Intermediate vessel tests have shown that, for pressure loading alone, vessels with large cracks did not fail until pressures were well in excess of that allowable for faulted conditions under American Society of Mechanical Engineers (ASME) Boiler and Pressure Vessel Code rules. One test (V-8) demonstrated clearly the effects of combined loading under linear-elastic conditions, inasmuch as a crack under the influence of pressure and weld-induced residual stresses propagated at pressures below design pressure.[5] Thus, except for the V-8 test, observations of crack behavior in the intermediate vessel test series were always under loading or stress conditions that could be viewed as excessive relative to realistic nuclear reactor vessel conditions. In test V-8, the temperature was low enough that the toughness of the test vessel was probably atypically lower than the worst that could be expected in a reactor vessel during this mode of loading. Thus, tests performed to date have not explored crack growth or fracture in completely realistic conditions of stress state and toughness.

The impending test of intermediate vessel V-8A will be an important step toward simultaneous attainment of realistic upper-shelf toughness levels, fracture modes, and stress levels with pressure loading. Evidently, from accident studies and the HSST thermal shock experiments, consideration must also be given to tests with combined pressure and thermal shock loads.

With pressurized thermal shock loading of an intermediate test vessel, stress states as well as toughnesses can be made to conform to the essential features of conditions that would exist in hypothetical thermal shock accidents. Small-break LOCAs, steam-line breaks, and other overcooling episodes in nuclear power plants produce conditions conducive to crack initiation. Even small cracks can be made to initiate by thermal shock. Superposition of pressure can lead to a variety of responses: at one extreme, a short surface crack would elongate and arrest; at the other, the crack would extend without arrest. Variations in behavior theoretically attainable include (1) multiple crack initiation and arrest steps, (2) initiation in the transition with arrest on the upper shelf, and (3) initiation by tearing followed either by stable or unstable tearing or by conversion to cleavage.

Types of pressurized thermal shock experiments relevant to problems of operating reactors include both transition and upper-shelf behavior. Both linear-elastic fracture mechanics and elastic-plastic fracture mechanics methods are needed to evaluate this range of behavior. Both need additional verification for some conditions, particularly for short flaws under thermal loading and combined loading when both cleavage and tearing may be involved.

Evaluations are currently in progress for identifying modes of crack behavior under combined loads and for defining test facility requirements. Preliminary design concepts have been formulated and analyses are being made to determine the effects of parametric and dimensional changes on performance. Computations being made are discussed in Sects. 5.2.2 and 5.2.3.

### 5.2.2 Test facility design studies

The testing facility concept under consideration is the existing intermediate vessel test facility[6,7] augmented by a coolant loop of the type used in the first four thermal shock experiments.[8] The existing pressurizing system and its supporting systems will be used. Coolant for producing the thermal shock will be supplied by a circulating system currently under study. In this concept, chilled liquid contained in a storage tank is admitted suddenly to the test section of a flawed test vessel, flows along the test section, and returns to the storage tank. For reasons discussed previously,[9] only the outside surface of the vessel is cooled. Consequently, the coolant loop operates at low pressure.

Factors being considered first are coolant properties and the effect on performance of pipe size, storage capacity, mass flow, and test section hydraulic diameter. Parametric heat transfer and fluid flow calculations have been made based upon a preliminary layout of the facility. Water and methanol-water mixtures were evaluated at bulk temperatures of 4°C and −23 to −12°C, respectively. A maximum vessel wall temperature of 290°C was assumed. These calculations and the fracture analyses described in the next section define ranges of design parameters for satisfactory thermal shock performance. With components of practical size and capacity, the test facility should be capable of producing fractures in a variety of modes or permit reasonable latitudes in selection of test conditions.

The intermediate test vessels were designed for pressure loads only, with special criteria to ensure that the access head and nozzle subassembly would not fail in the course of pressure tests (Ref. 7, pp. 4 to 10). Most of the intermediate vessel tests involved pressures over 180 MPa (almost 3 times the design), and no problems with sealing the head have been experienced. However, test temperatures were all below 100°C, in contrast to the 290°C temperatures expected in pressurized thermal shock tests. Different elastomeric O-ring materials must be used, and it is not clear whether thermal stresses will tend to open the seal surfaces. To evaluate the seal and secondary stresses in the vessel closure, a 2-D analysis of this assembly is being made with the ADINA finite-element code.

### 5.2.3 Determination of stress intensity factors for surface flaws in cylinders under combined pressure-thermal loading

(J. W. Bryson, B. R. Bass, R. H. Bryan)

A series of calculations is in progress to ascertain the dependence of flaw behavior on the parameters of a combined pressure-thermal loading, flaw size and shape, and initiation and arrest toughnesses. The results of this study will be used to predict the various sequences of events that can be anticipated in pressurized thermal shock experiments.

Calculation of stress-intensity factor ($K_I$) distributions is the major problem in this study, and it depends primarily on finite-element computer codes. Currently the OR-FLAW[10] and ADINAT[11] codes are being used for a preliminary evaluation of $K_I$ as a function of loading and flaw geometry. Outside surface flaws of several lengths and depths will be analyzed.

Several trial calculations with the OR-FLAW code were made to determine its suitability for this study. The $K_I$ distributions were calculated for part-circular and semielliptical flaws, and variations in mesh details were investigated. The $K_I$ distributions of the semielliptical flaws exhibited a kink, that is, a relative minimum and maximum near the ends of the flaw; whereas the distributions for a modified part-circular flaw shape were smooth. Whether the kink is real or artificial, that kind of behavior would make perceiving the effects of primary concern more difficult at this time. Consequently, the modified part-circular shape was chosen for the current study. A comparison of

$K_I$ distributions calculated with OR-FLAW and ADINA indicated that the two methods gave comparable results for internal pressure loading.[12]

The model used in the $K_I$ calculations for pressurized thermal shock is shown in Fig. 5.4. The intermediate test vessel is modeled as an open cylinder with pressure applied to the inside surface and tractions on the ends equivalent to the axial stress in an infinitely long closed cylinder. The thermal boundary conditions represent insulated ends and a thermal shock imposed on the outside surface at time $t = 0$.

Of the quadrant shown in Fig. 5.4, only the part within ~690 mm of the $x = 0$ plane represents the actual test vessel cylinder. The part of the model beyond 690 mm is included to simulate the thermal and restraint effects of the two ends of the vessel. The ends will not be cooled during the thermal shock and will, therefore, lead to axial variations in thermal stress. This effect is being studied separately and will be discussed in future reports.

The cases completely analyzed this quarter are defined by the parameters in Table 5.2. The cylinder and the liquid inside and outside are initially at a uniform temperature $T_o$. In this condition and with pressure $p = 0$, the cylinder is stress free. At $t = 0$, the liquid on the outside undergoes a step change in temperature $\Delta T_o = -290$ K.

Table 5.2. Intermediate test vessel outer surface flaws considered[a]

| Flaw No. | Part-circular flaw parameters[a] (mm) | | Thermal shock | | |
|---|---|---|---|---|---|
| | Depth, a | Length, b | $\Delta T_o$ (K) | $h_{inside}$ ($W \cdot m^{-2} \cdot K^{-1}$) | $h_{outside}$ ($W \cdot m^{-2} \cdot K^{-1}$) |
| 1 | 64 | 110 | −290 | 100 | 5000 |
| 2 | 64 | 220 | −290 | 100 | 5000 |

[a] See Fig. 5.4 for definition of parameters.

Temperature distributions for several time steps in the thermal transient were calculated with ADINAT (Fig. 5.5), and these were input to OR-FLAW for the $K_I$ calculations. The ADINAT solution represents an axisymmetric analysis of an uncracked cylinder, that is, the flaw surfaces are not cooled.

The OR-FLAW finite-element discretization in the plane of the flaw is shown in Figs. 5.6 and 5.7 for each configuration. Figures 5.8 and 5.9 give the $K_I$ distributions for several time steps into the transient. The $K_I$ distributions for thermal loading only may be obtained by subtracting the pressure-loading $K_I$ distributions shown from the given combined loading distributions.

ORNL-DWG 81-6871

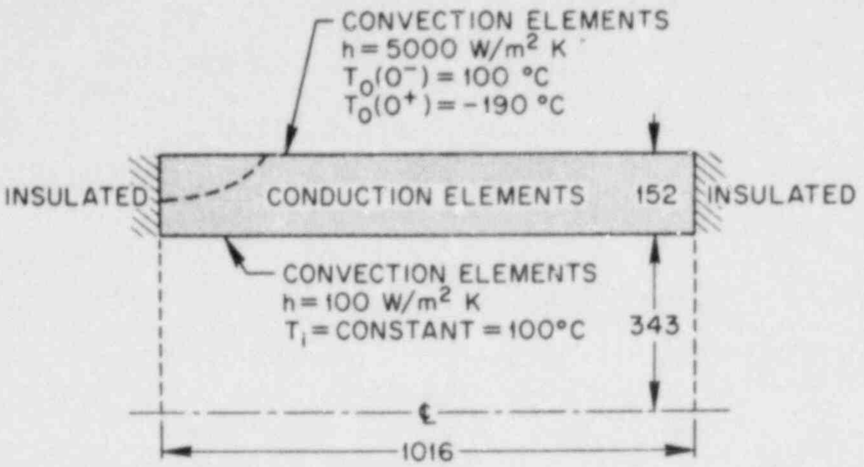

(*a*) ADINAT BOUNDARY CONDITIONS

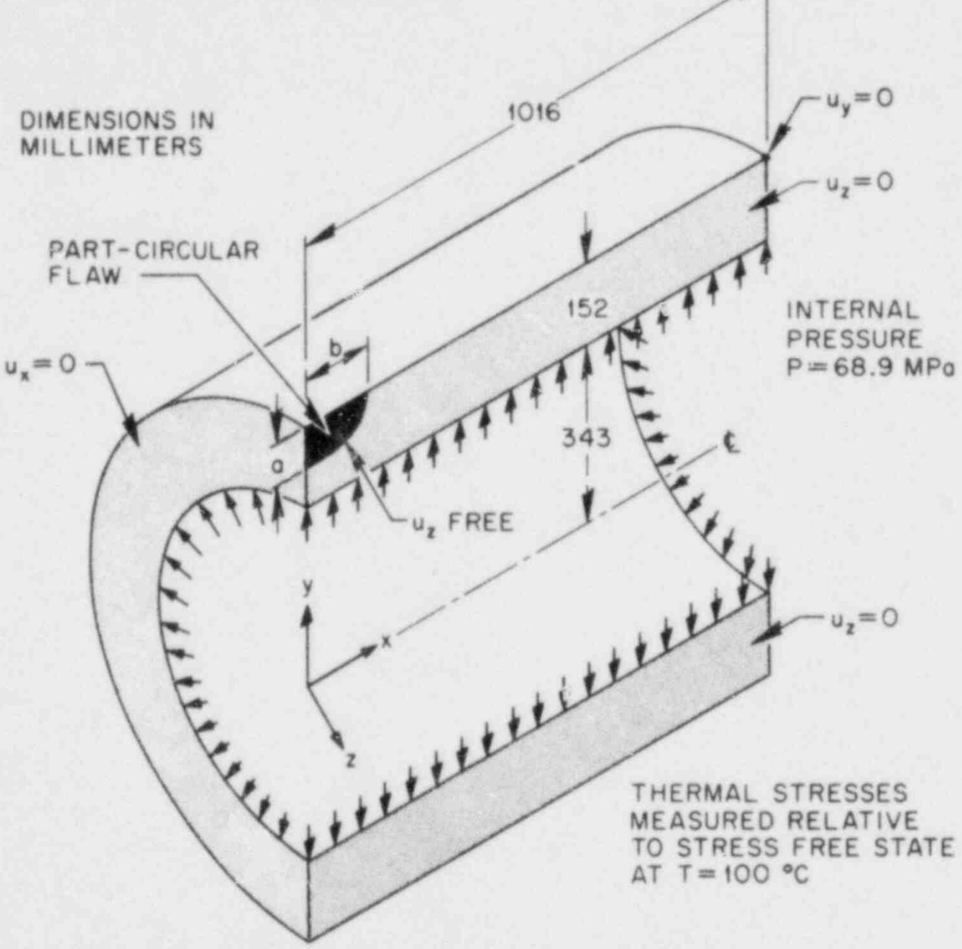

(*b*) OR-FLAW BOUNDARY CONDITIONS

Fig. 5.4. Problem definition and dimensions for pressurized thermal shock flaw analysis of intermediate test vessel.

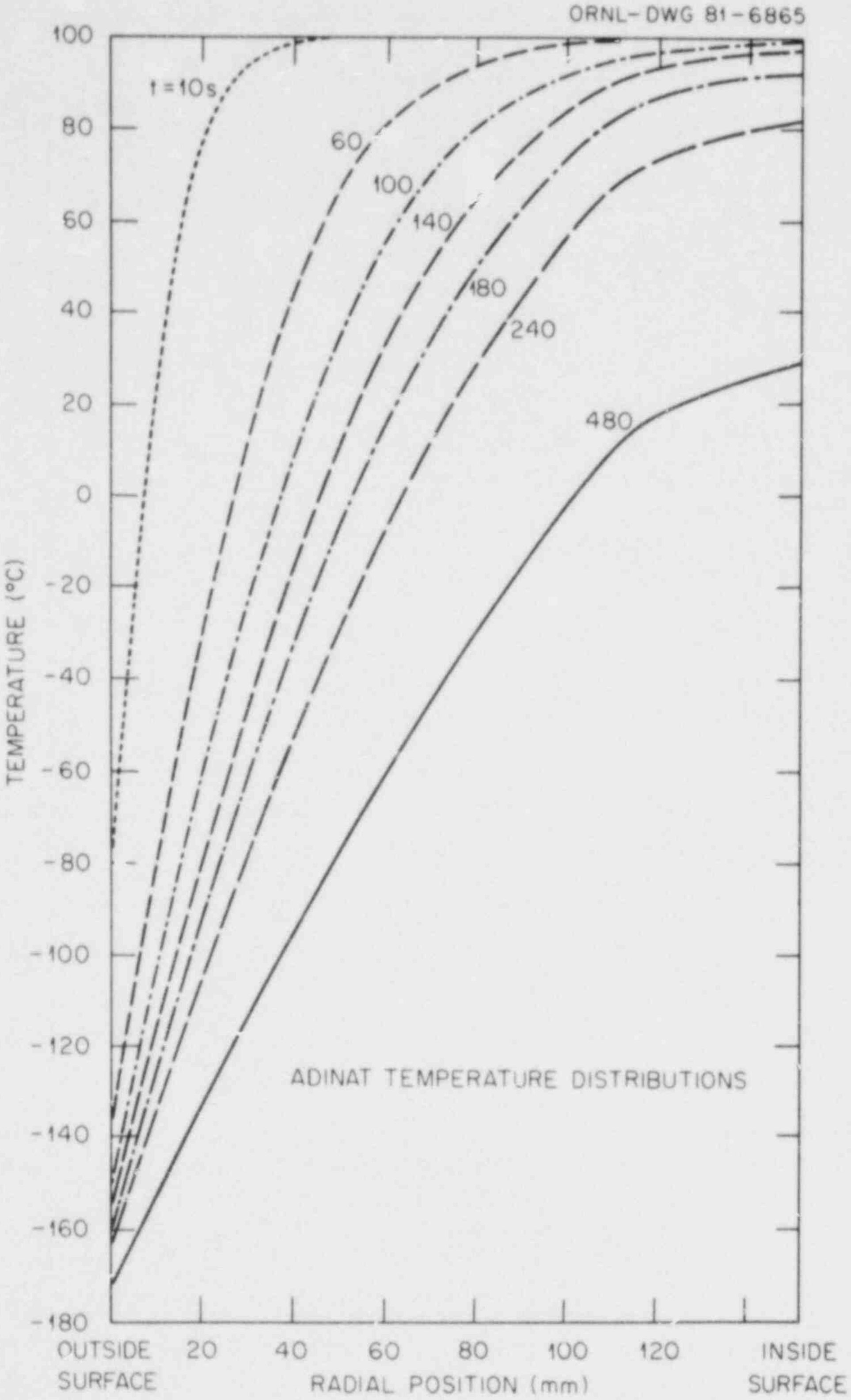

Fig. 5.5. Transient temperature distribution in cylinder from ADINAT solution for $T_o = 100°C$ and $\Delta T_o = -290$ K.

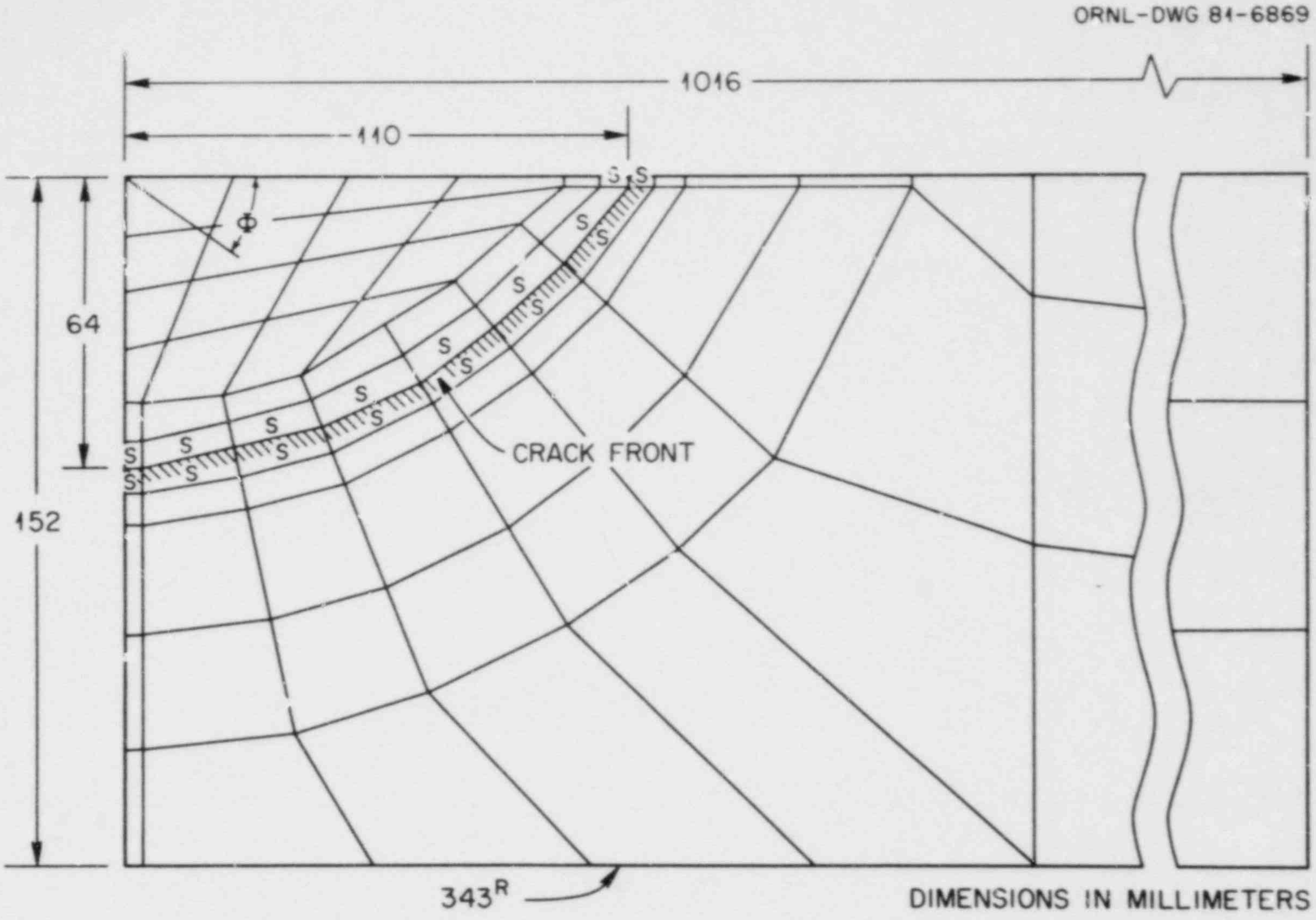

Fig. 5.6. OR-FLAW finite-element discretization in plane of flaw for flaw No. 1 (a = 64 mm, b = 110 mm). Special crack-tip elements are marked S along flaw front.

ORNL-DWG 81-6870

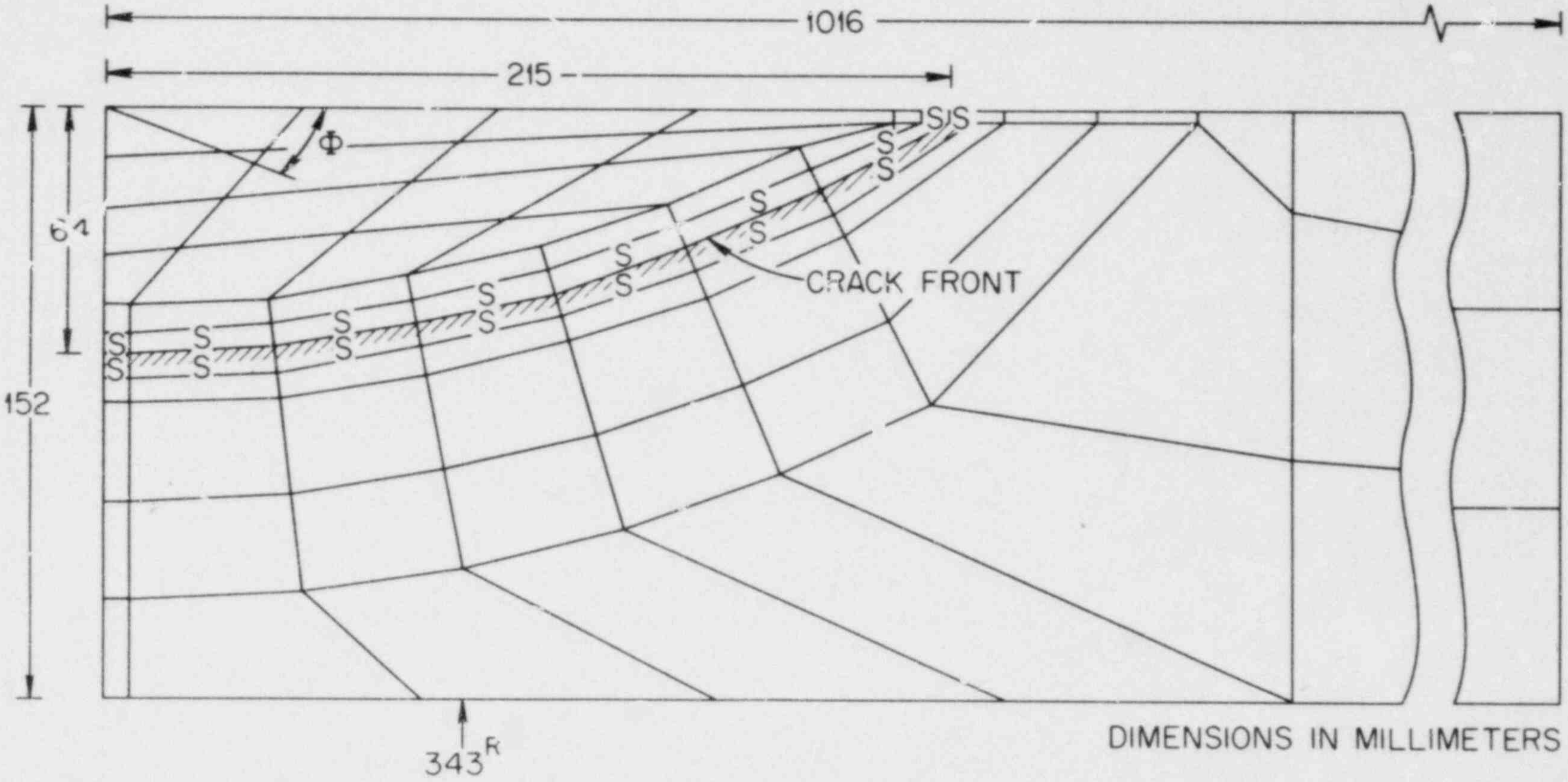

Fig. 5.7. OR-FLAW finite-element discretization in plane of flaw for flaw No. 2 (a = 64 mm, b = 220 mm). Special crack-tip elements are marked S along flaw front.

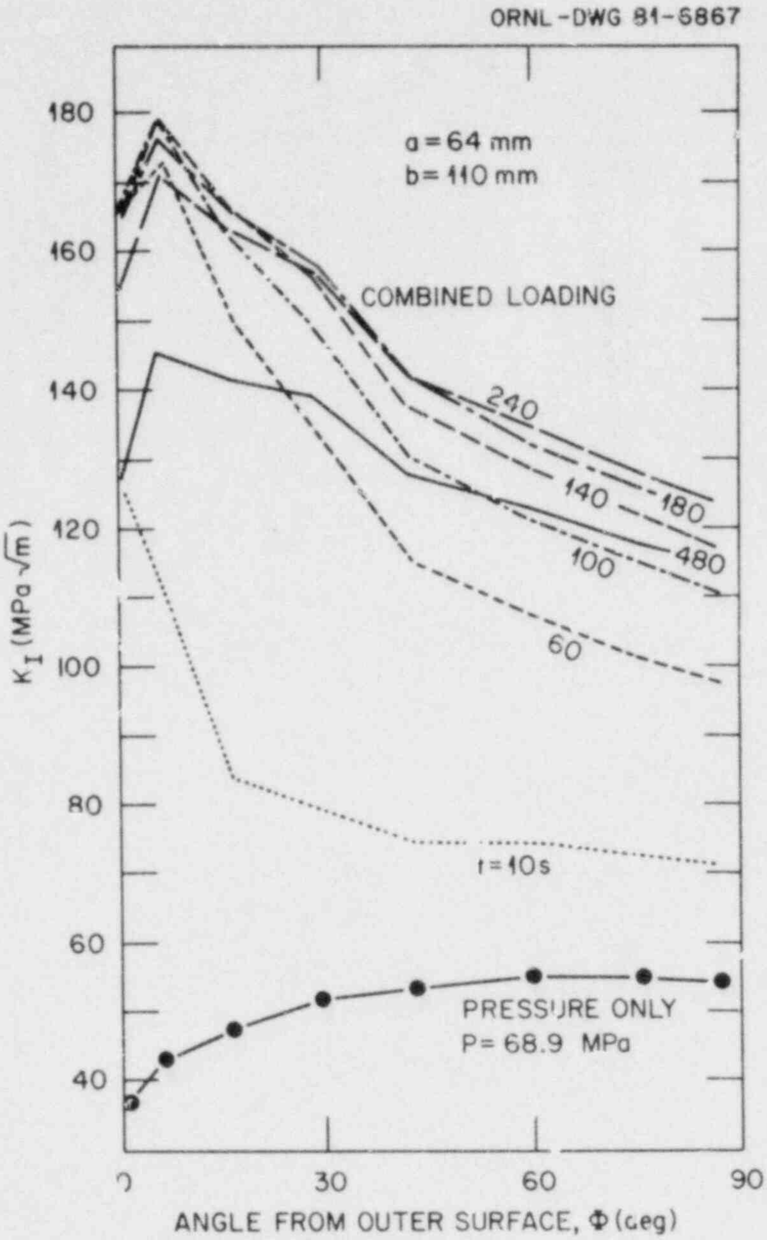

Fig. 5.8. $K_I$ distributions for intermediate test vessel outer surface flaw No. 1 (a = 64 mm, b = 110 mm) for pressurized thermal shock.

The results presented are for a severe thermal shock relative to the ultimate capability of the test facility. The pressure is approximately the test vessel design pressure. The results imply that crack initiation under combined loading can be induced for flaws of reasonable size and realistic fracture toughnesses. Note that conditions of initiation are attainable while general primary membrane stress intensities are in the range of ASME code allowable values.

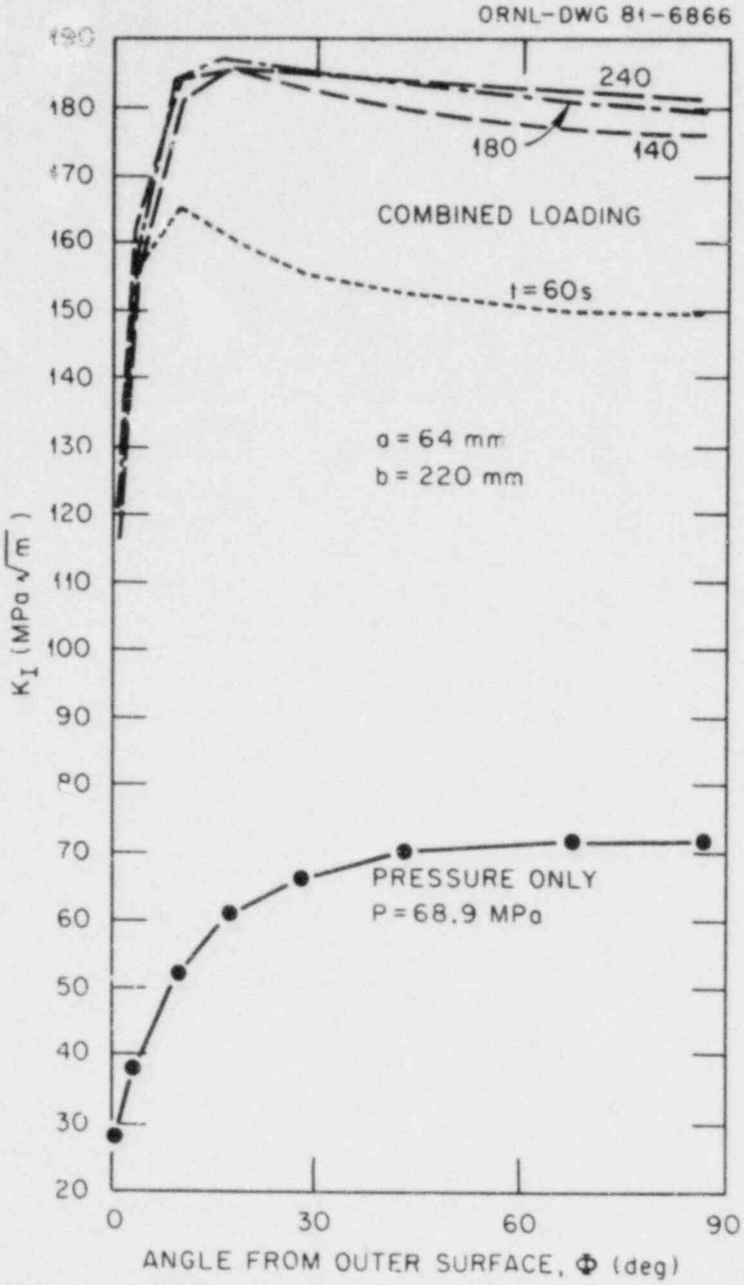

Fig. 5.9. $K_I$ distributions for intermediate test vessel outer surface flaw No. 2 ($a = 64$ mm, $b = 220$ mm) for pressurized thermal shock.

## 5.3 Nozzle-Corner Flaw and Fracture Surface Investigations

P. P. Holz

Because intermediate test vessel V-5 may be rebuilt to perform another nozzle-corner flaw test, the original V-5 flaw was removed. Requirements for the removal were (1) to investigate and properly preserve the fracture surfaces and (2) to minimize material removed from the cylindrical vessel portion adjacent to the peripheral nozzle weld.

Vessel V-5 was tested in February 1974 at a test temperature of 88°C (Ref. 13) with the vessel loaded in 13.8-MPa pressure increments to 82.7 MPa and then in 6.89-MPa increments to 179 MPa. The pressure at maximum load was 183 MPa. Stable crack growth was observed up to this maximum loading, at which a leak without break (i.e., no fast running crack) was observed. The failure or leak was innocuous and was indicated only by a slight loss of pressure under continued pumping. Remote camera TV observations also noted the emergence of a fine spray from the upper-right-side corner of the ultrasonic base block (Fig. 5.10).

Wedge removal operations were generally handled with the vessel placed on a dolly-carrier (Fig. 5.11) and included oxygen-jet flame cutting and "hot-rod" gouging. Scrap sheet steel liners and compressed air were used within the vessel for kerf and slag protection during flame- and arc-cutting operations. Unavailability of a welding-positioner table sufficiently large and massive enough to handle the 8000-kg vessel necessitated machine-drill and -mill assists for deep-section torch operations and suggested a sequenced wedge removal approach:

1. Flame-cut (sever) the upper nozzle in the dome's 101-mm wall section (Fig. 5.12).
2. Mount the vessel horizontally on a 6-in. Giddings and Lewis vertical boring mill; machine along the block perimeter (Fig. 5.13). Depths for the required machine cutting ranged from 152 mm to nearly 305 mm. A 25.4-mm milled starter slot was used for the upper portion of the deeper cuts, followed by drilling perimeter holes on close centers.
3. Remount the vessel to the dolly; arc-air sever the remaining ligaments between the drilled holes using 6.4-mm copper-clad electrodes and dc power.

The as-removed block is shown in Fig. 5.14. The marker lines in the figure indicate the saw-cut layout for edge material removal. Excess edge material must be removed from the specimen to minimize end-restraining effects (beyond the fracture surfaces) prior to placing the block, prechilled in liquid nitrogen, onto a press-brake for a wedge die to enter the deeply gouged starter flaw in the interior nozzle-corner (Fig. 5.15). The figure is a post V-5 test view taken from within the vessel, also showing thermocouples, strain gages, support bracket posts for the interior displacement gage, and coating.

Figure 5.16(a,b) shows two views of the as-split left-hand (L) and right-hand (R) block pieces and an end slice W cut from the L piece. This slice was taken to show the cross section of the vessel fabrication nozzle-to-cylinder weld. Figures 5.17 and 5.18 are sectional elevation views of the fracture plane, and Fig. 5.19 is a direct comparison view of weld slice W taken in a parallel plane immediately beyond the fracture. Note lack of flaw propagation symmetry from the influence of this weld that resisted and deflected the crack growth front. [A symmetrical pattern is represented by the superimposed dotted line.]

The right-hand portion of the fracture surface, block R, is shown in Figs. 5.20 and 5.21. The latter figure clearly shows a change in the

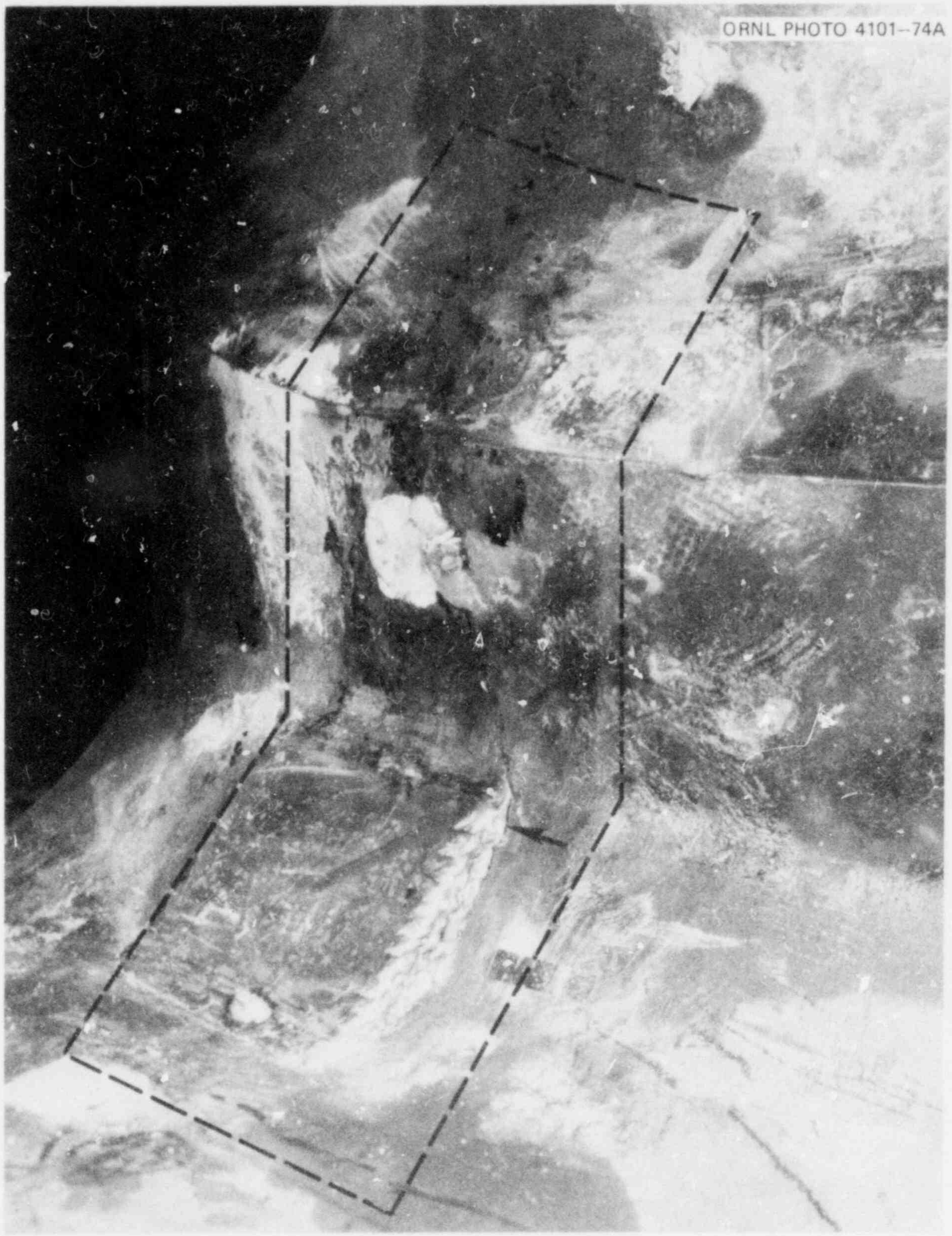

Fig. 5.10. Close-up view of leakpoint adjacent to ultrasonic base block on nozzle corner of vessel V-5. Arrow shows flaw penetration to surface; dotted line indicates cut planes for the removal of the block specimen containing the flawed region.

ORNL PHOTO 7305-80

Fig. 5.11. Intermediate test vessel 5 on transport dolly-carrier.

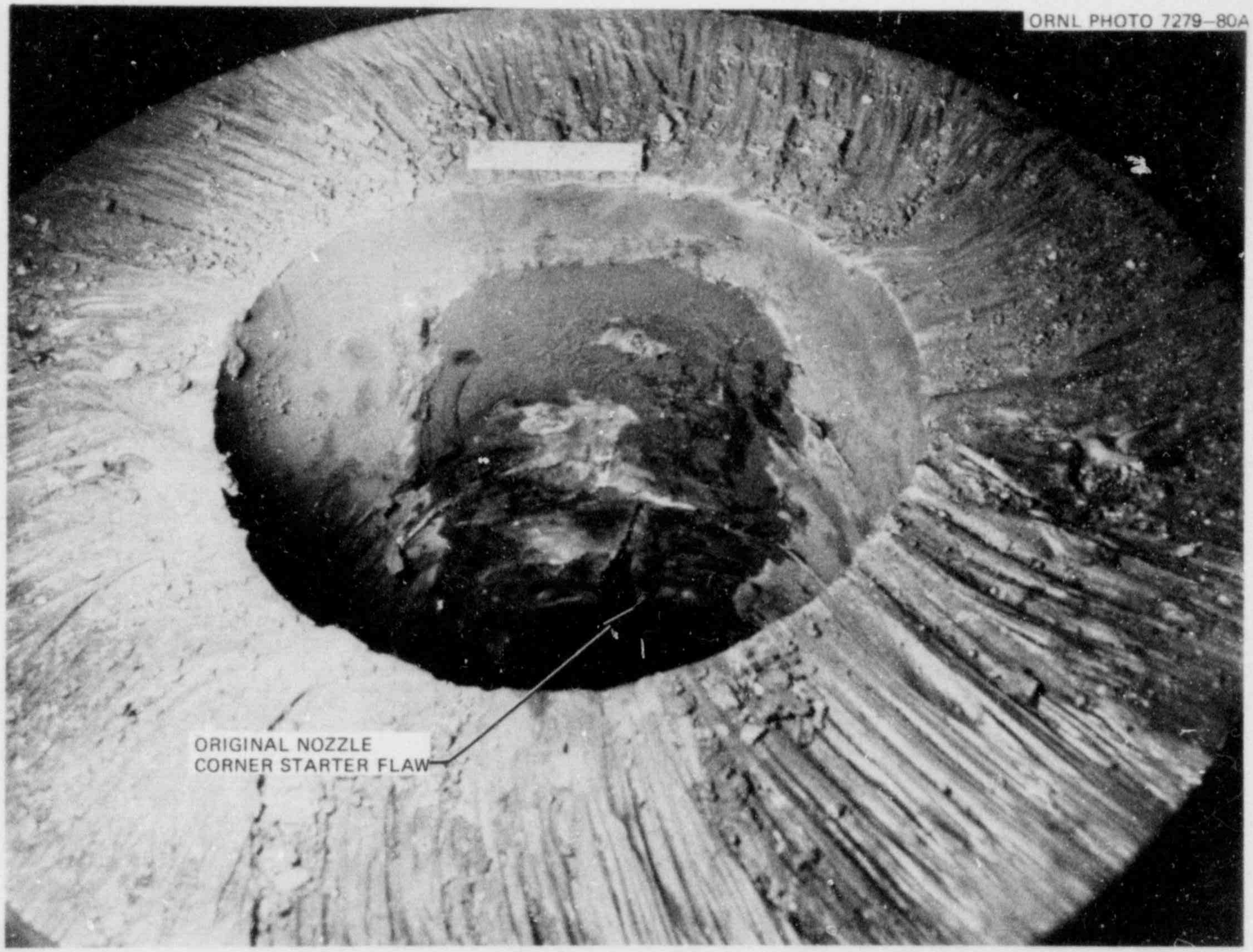

Fig. 5.12. View of vessel V-5 nozzle corner after flame-cut nozzle dome removal.

ORNL PHOTO 7306-80

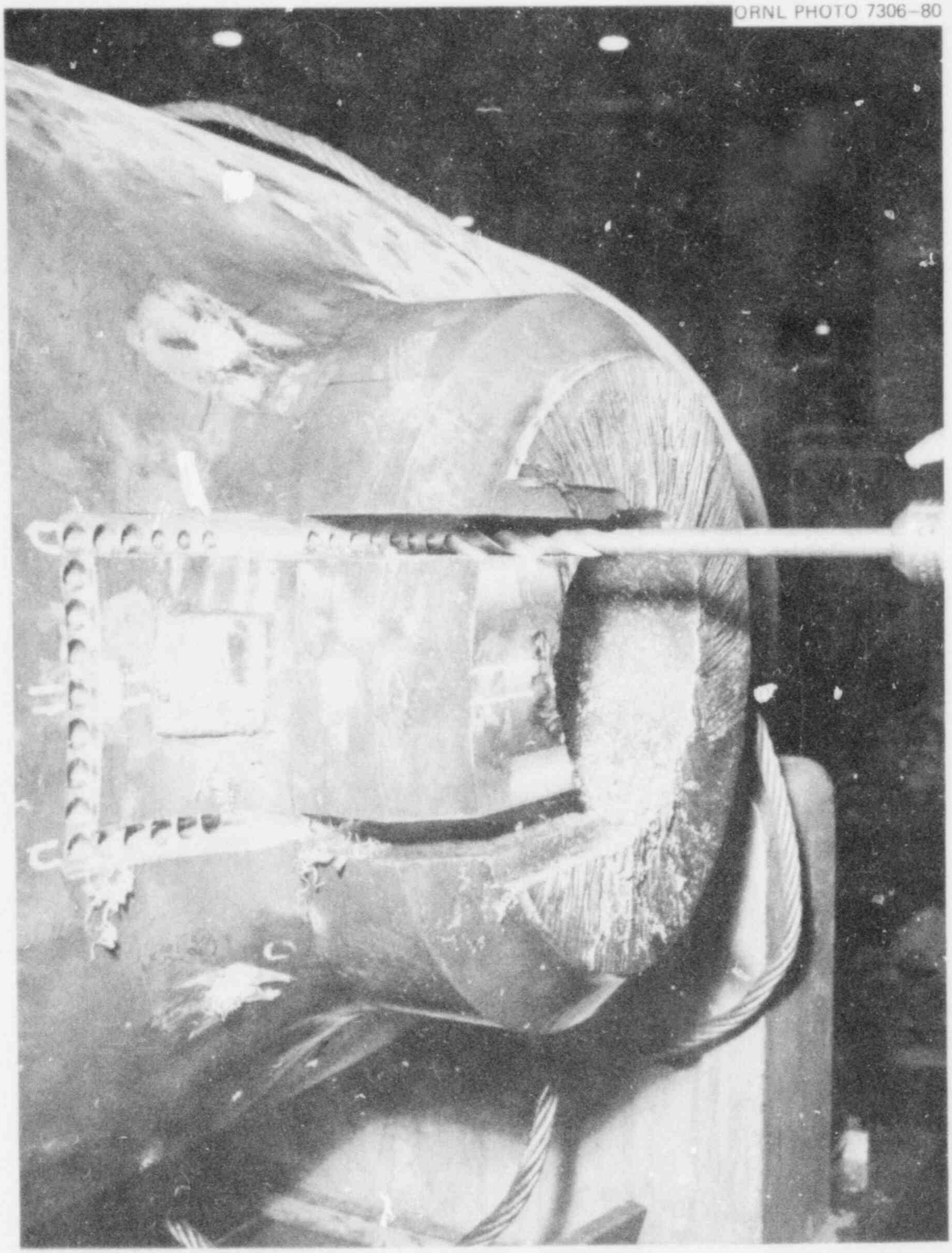

Fig. 5.13. Drill and mill machining to remove the vessel V-5 specimen containing the flawed region. Vessel is located on a vertical boring mill.

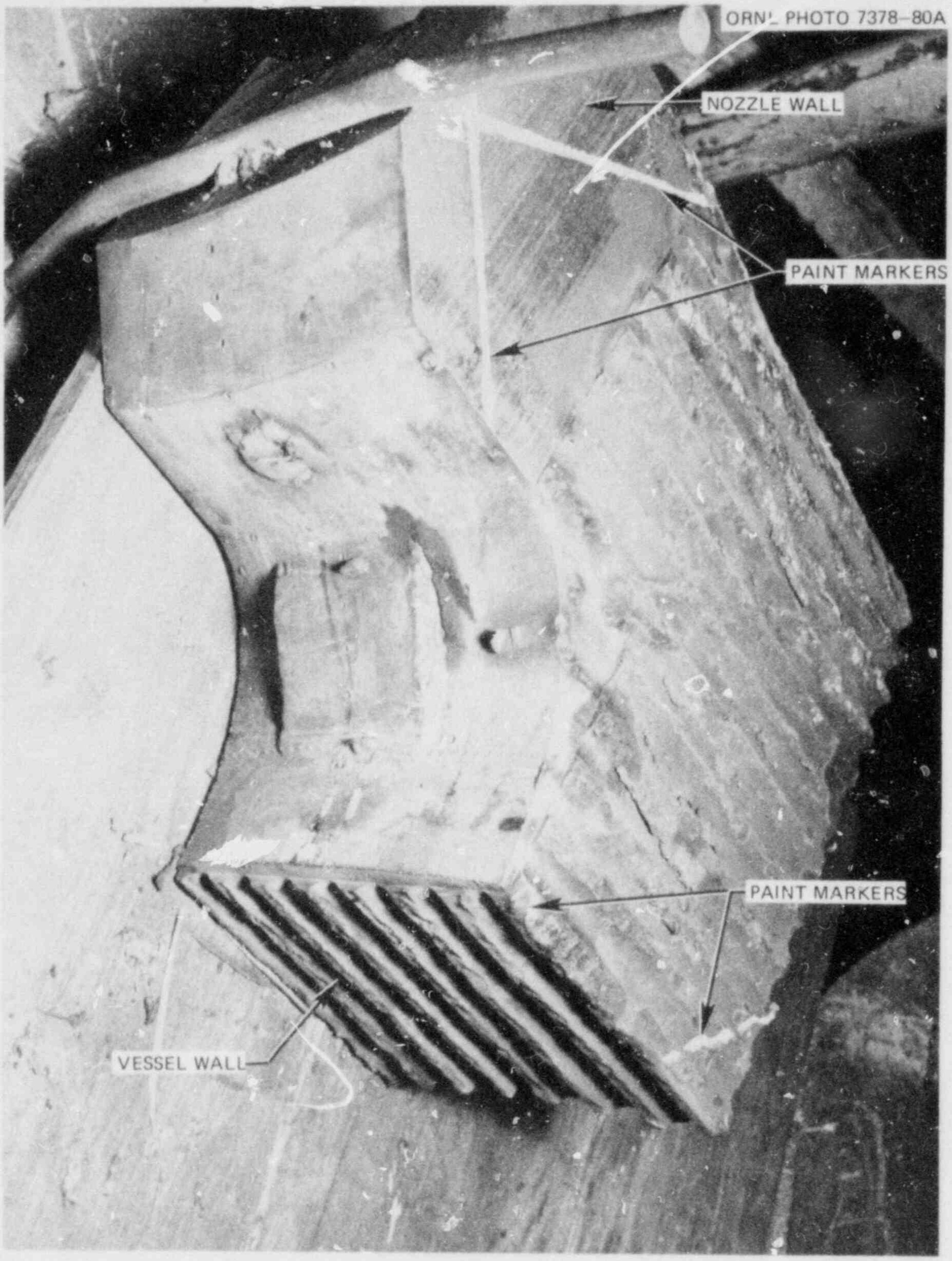

Fig. 5.14. As-removed block containing the vessel V-5 nozzle-corner flawed region. (Paint marker lines indicate sawlines for subsequent saw cuts.)

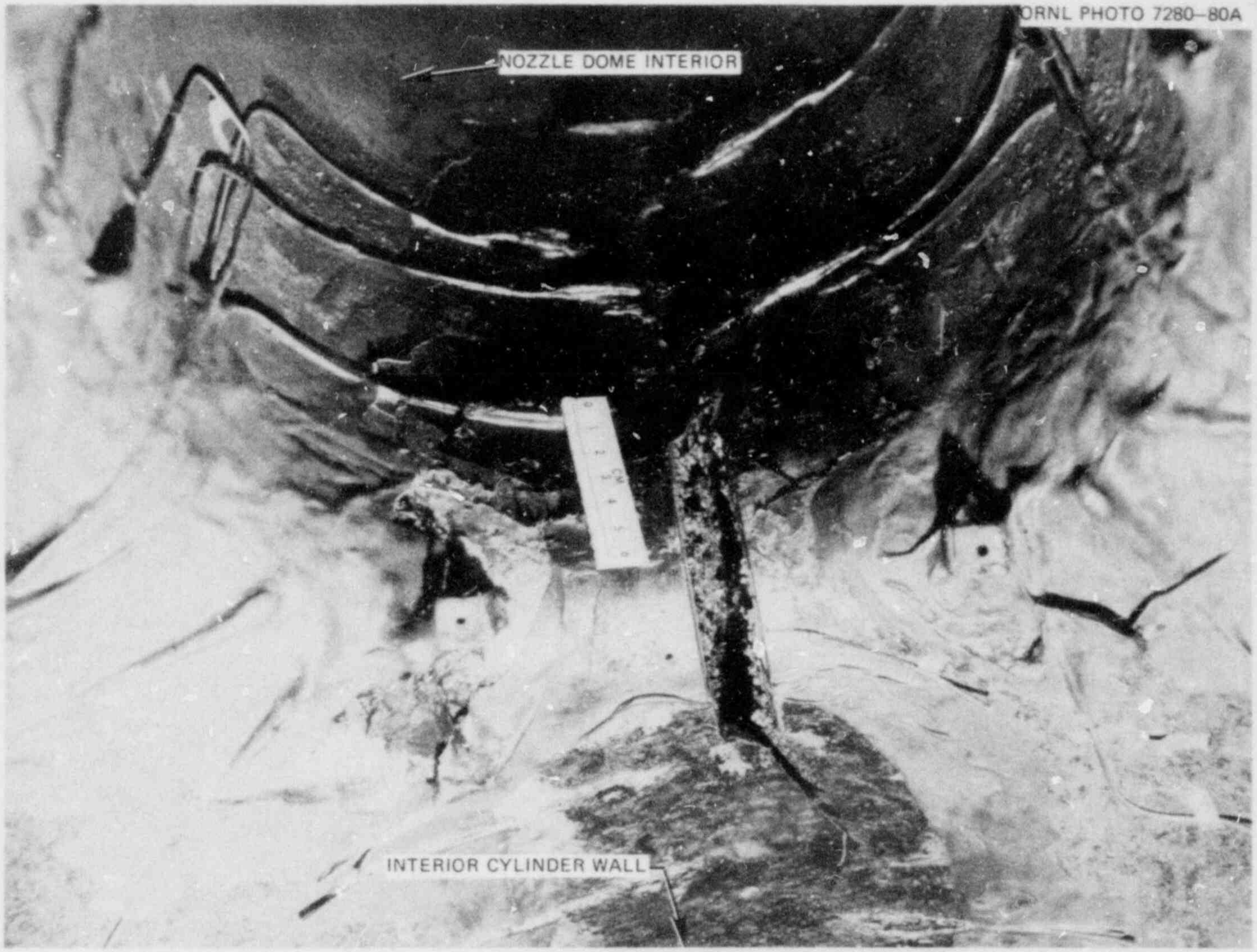

Fig. 5.15. ITV-5, inside vessel view of flaw and flaw fracture surfaces prior to removal from vessel.

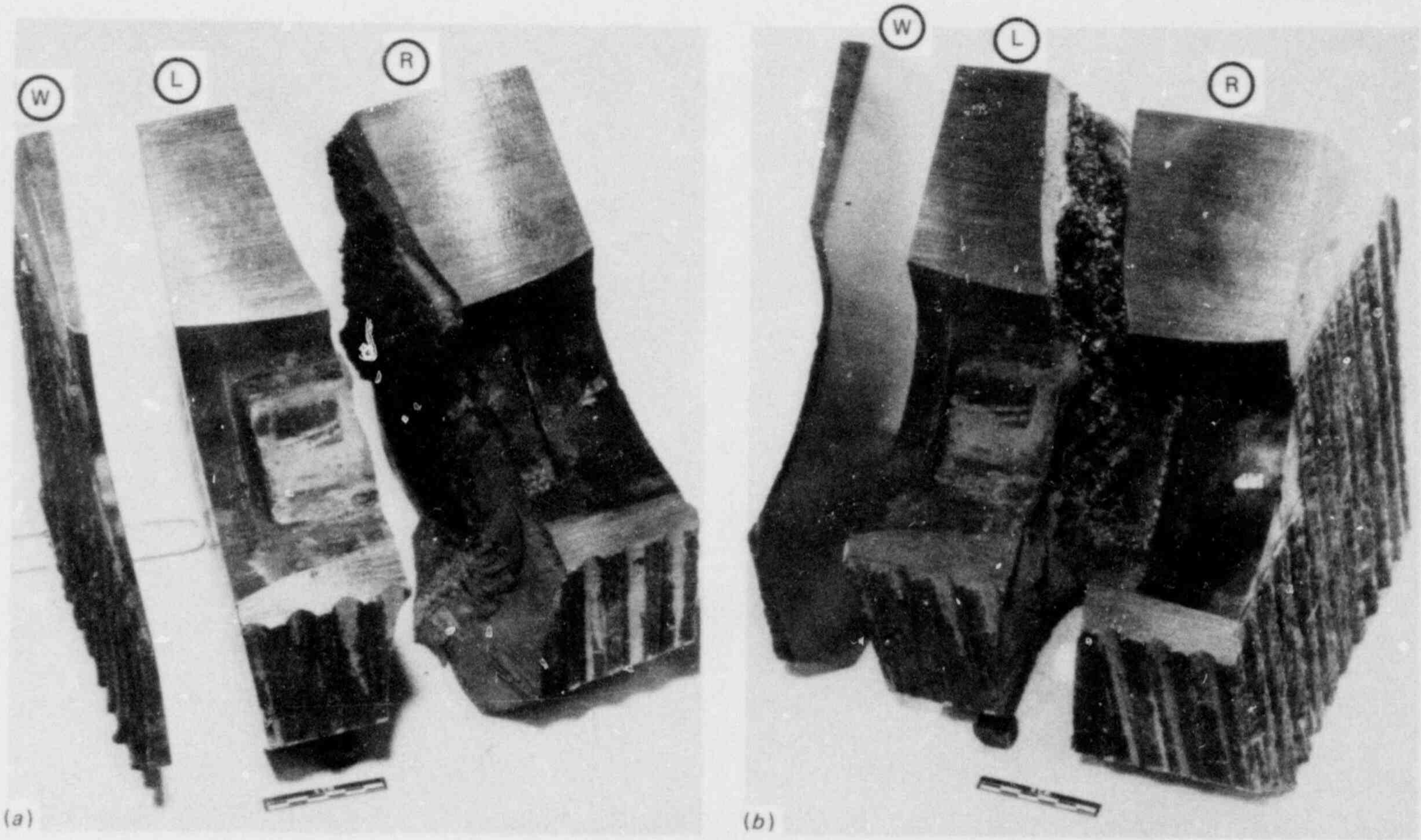

Fig. 5.16. Reference Index: As-split block containing the flawed regions and slice W. The surface of slice W is etched to indicate the nozzle-corner fabrication weld.

ORNL PHOTO 7349–80A

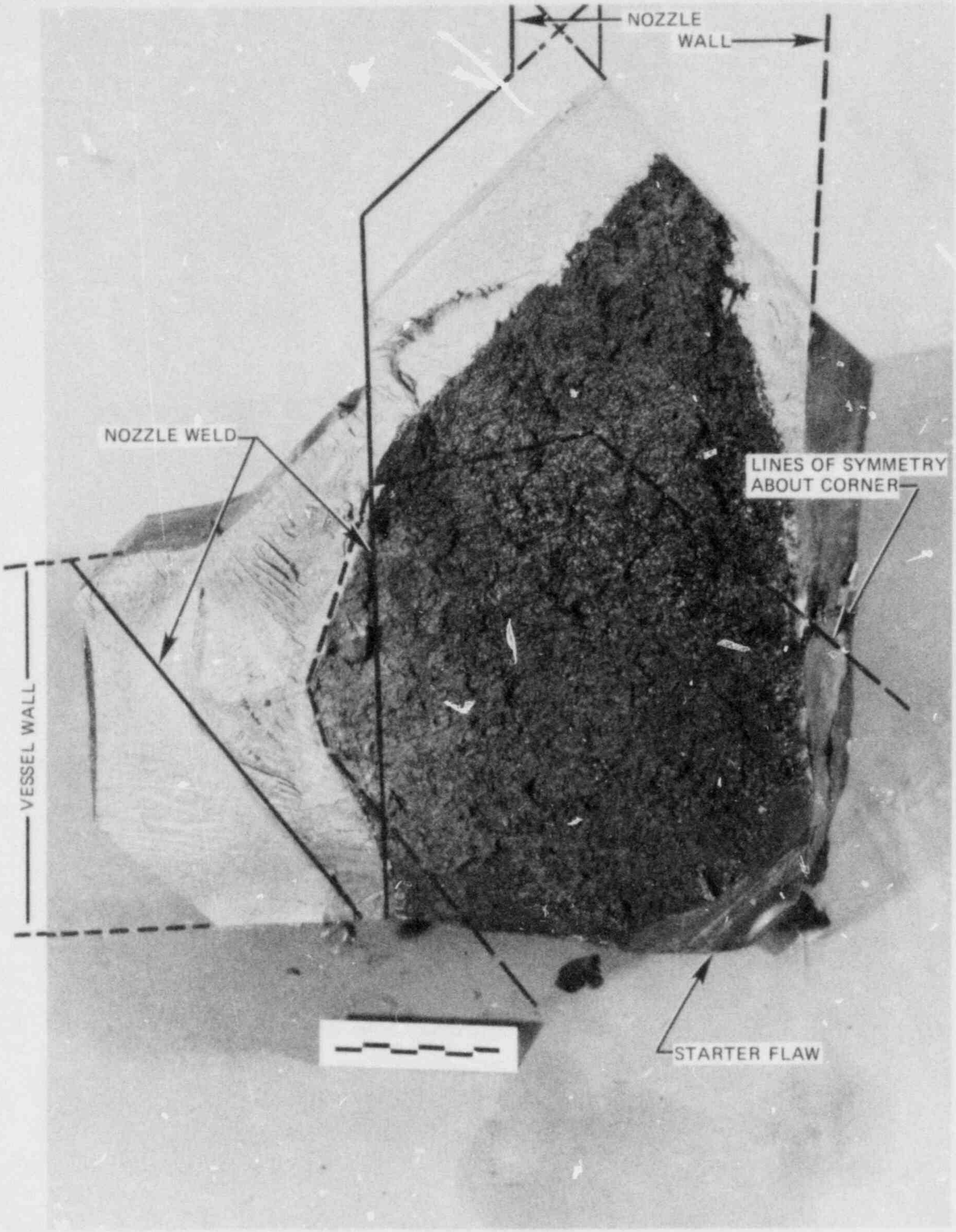

Fig. 5.17. Vessel V-5, left-side flawed region.

ORNL PHOTO 7351–80

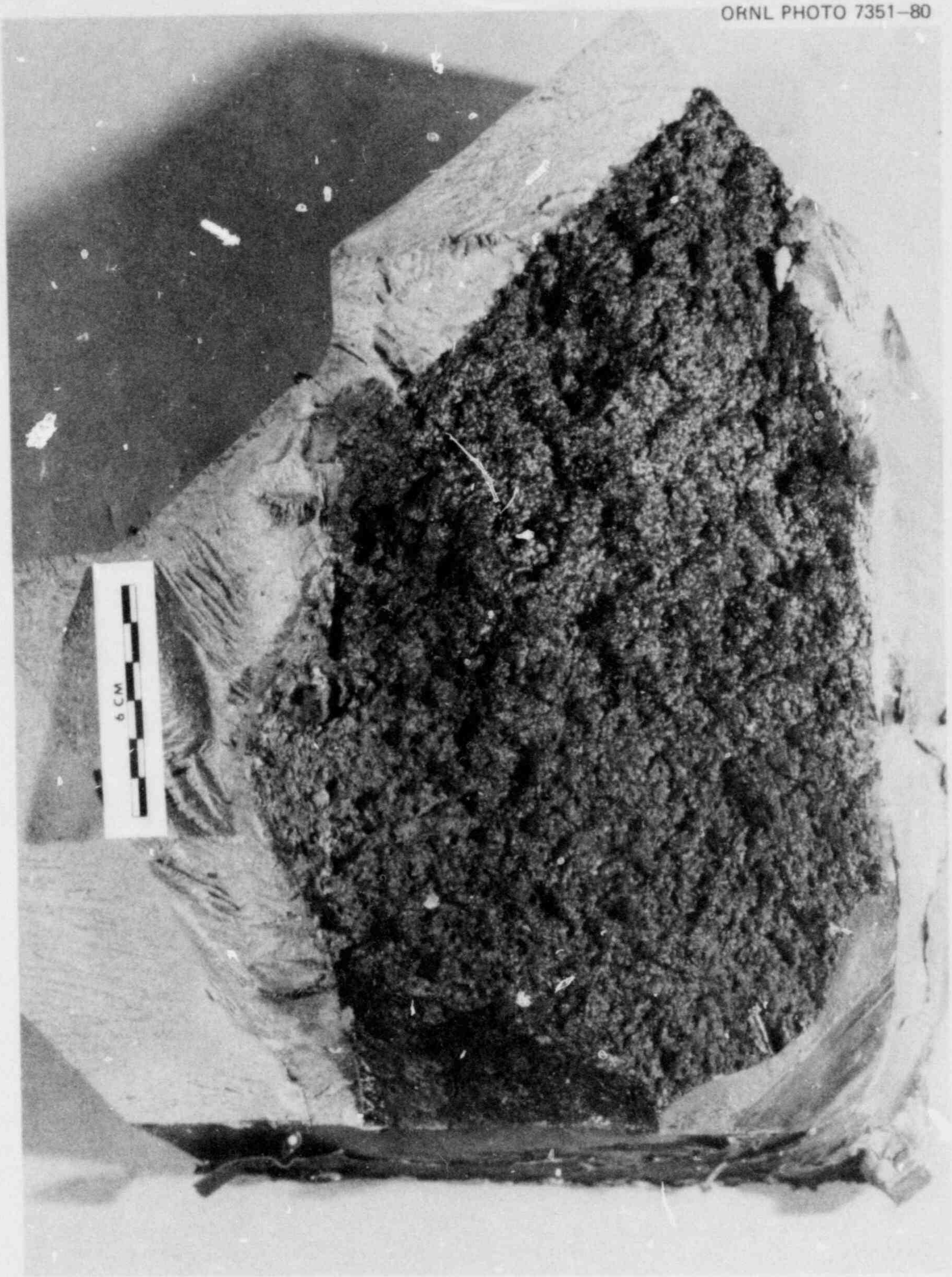

Fig. 5.18. Vessel V-5, left-side flawed region.

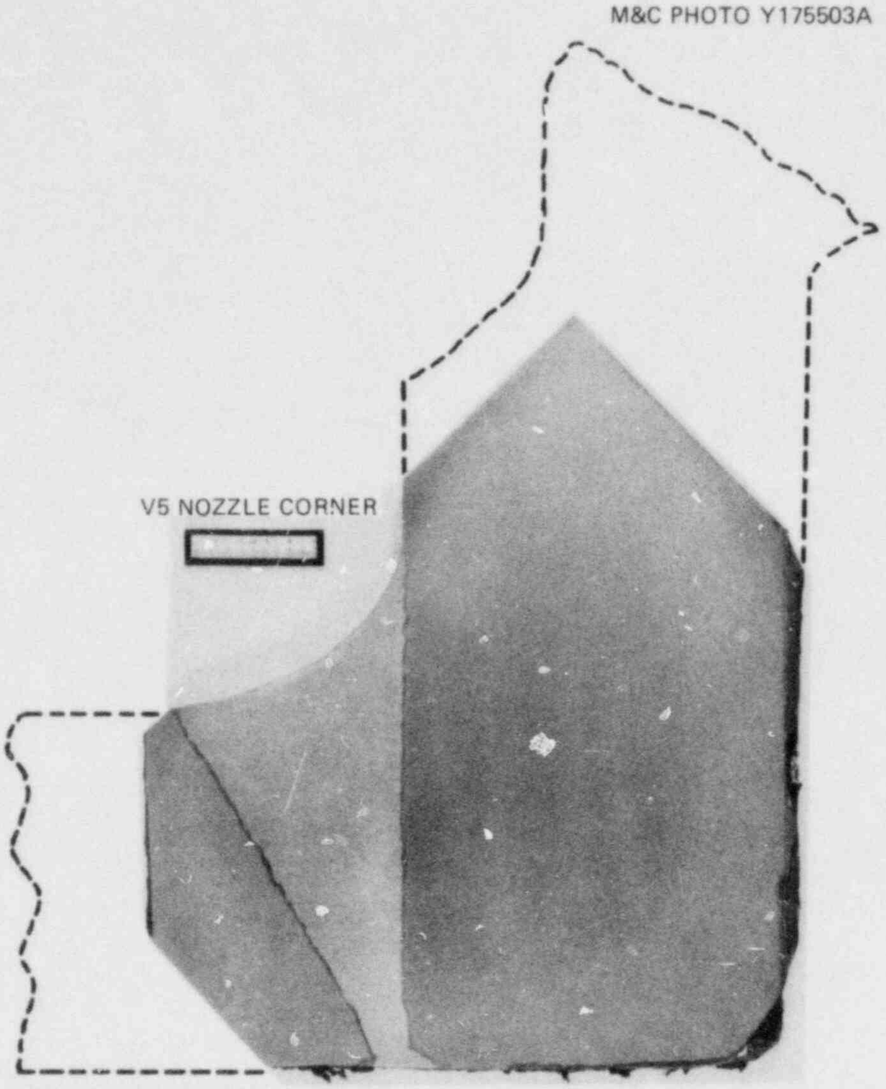

Fig. 5.19. Vessel V-5, cross section of nozzle-to-cylinder vessel fabrication weld.

flaw growth plane near the upper-right-hand edge of the weld-on base support for the ultrasonic crystal. Note the tunneling to the vicinity of the base block corner where we observed the leak that terminated the vessel V-5 test.

The schematic in Fig. 5.22 indicates the actual nonsymmetrical flawed regions vs anticipated (symmetrical) outlines and notes an estimate for crack front extension within the nozzle. The upper-corner cut was too shallow; thus, it missed a small portion of the flawed region. The dotted line representing an anticipated final flaw border was based on experimentation with plastic models by Smith at Virginia Polytechnic Institute and State University.[14,15]

ORNL PHOTO 7348–80

Fig. 5.20. Vessel V-5, right-side flawed region.

ORNL PHOTO 7350–80

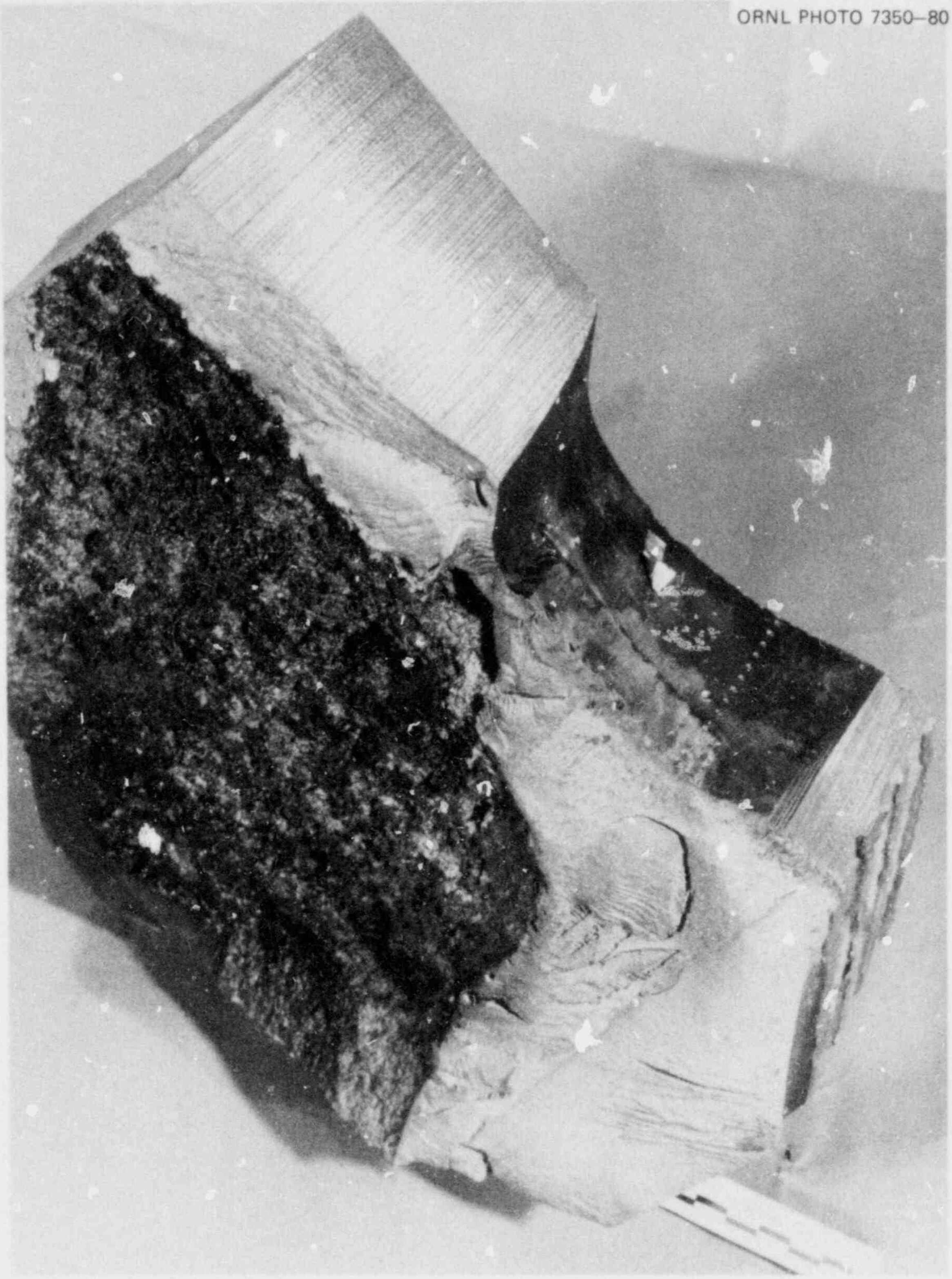

Fig. 5.21. Vessel V-5, right-side flawed region.

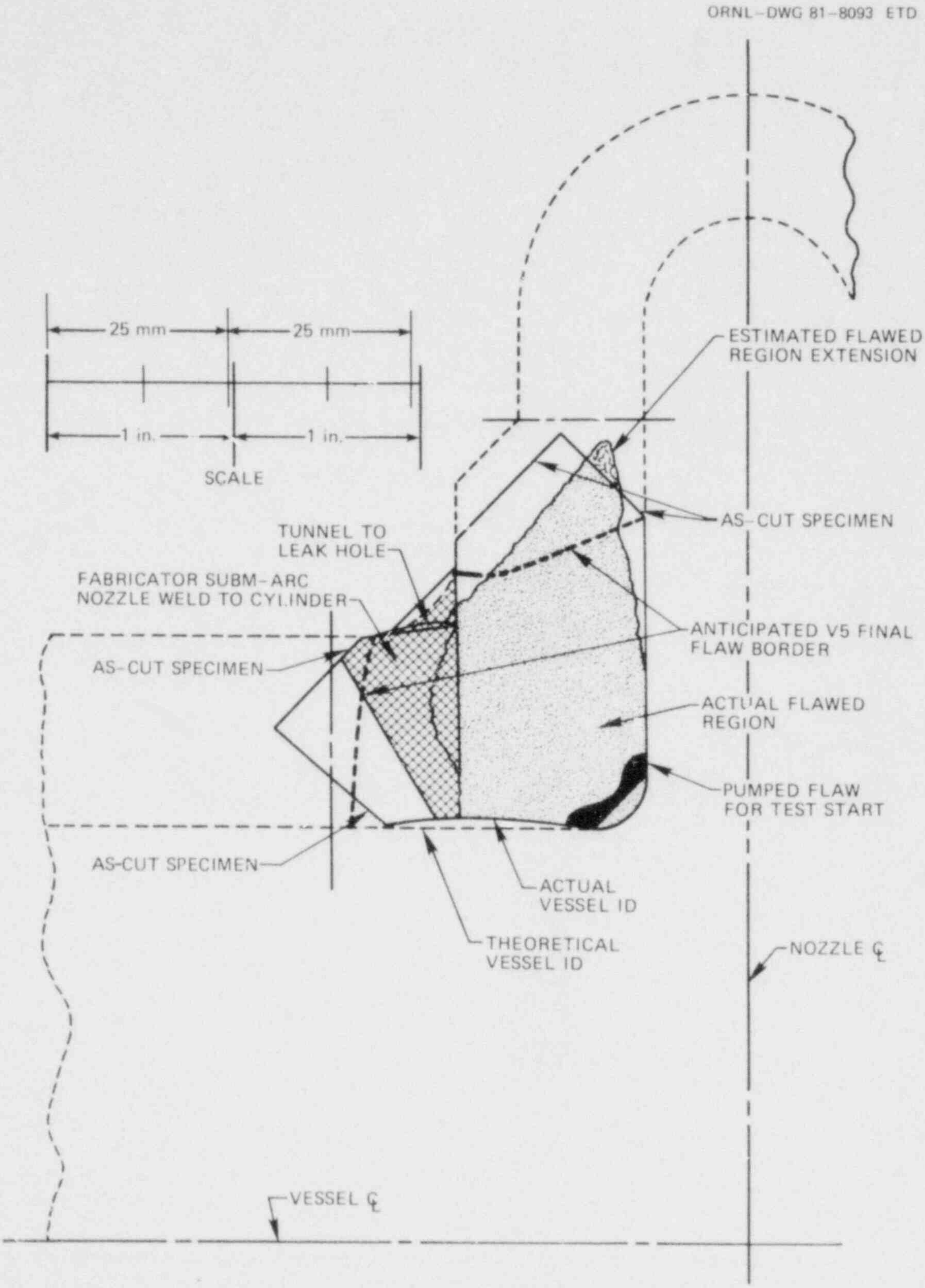

Fig. 5.22. Schematic of intermediate test vessel 5 nozzle-corner flaw.

## References

1. R. H. Bryan and P. P. Holz, "Intermediate Test Vessel V-8A," *Heavy-Section Steel Technology Program Quart. Prog. Rep. July–September 1980*, NUREG/CR-1806 (ORNL/NUREG/TM-419), p. 53.

2. P. P. Holz and R. H. Bryan, "Intermediate Test Vessel V-8A," *Heavy-Section Steel Technology Program Quart. Prog. Rep. October–December 1980*, NUREG/CR-1941 (ORNL/NUREG/TM-437), pp. 55–57.

3. H. A. Domian, *Vessel V-8 Repair and Preparation of Low Upper-Shelf Weldment. Report of Test Results of Tasks 1.4–1.5 Trial Weld 1.7–Base Metal*, The Babcock and Wilcox Company, Alliance, Ohio (Jan. 5, 1981; revised Feb. 17, 1981).

4. F. J. Loss, "Toughness and Ductile Shelf Properties of Irradiated Low-Shelf Weld Metals," Nuclear Regulatory Commission 8th Water Reactor Safety Research Information Meeting, Gaithersburg, MD, Oct. 27–31, 1980.

5. R. H. Bryan et al., *Test of 6-in.-Thick Pressure Vessels. Series 3: Intermediate Test Vessel V-8*, ORNL/NUREG-58 (December 1979).

6. C. L. Segaser, *System Design Description of the Intermediate Vessel Tests for the Heavy-Section Steel Technology Program*, ORNL/TM-2849 (June 1970, revised July 1973).

7. R. W. Derby et al., *Test of 6-inch-thick Pressure Vessels. Series 1: Intermediate Test Vessels V-1 and V-2*, ORNL-4895 (February 1974).

8. R. D. Cheverton, *Presssure Vessel Fracture Studies Pertaining to a PWR LOCA-ECC Thermal Shock: Experiments TSE-1 and TSE-2*, ORNL/NUREG/TM-31 (September 1976).

9. R. H. Bryan and G. C. Robinson, "Pressurized Thermal Shock Studies," *Heavy-Section Steel Technology Program Quart. Prog. Rep. October–December 1980*, NUREG/CR-1941 (ORNL/NUREG/TM-437), pp. 57–60.

10. S. N. Atluri et al., *OR-FLAW: A Finite Element Program for Direct Evaluation of K-Factors for User Defined Flaws in Plates, Cylinders, and Pressure-Vessel Nozzle Corners* (to be published).

11. K. J. Bathe, *ADINAT — A Finite Element Program for Automatic Dynamic Incremental Nonlinear Analysis of Temperatures*, Report 82448-5, Mechanical Engineering Department, Massachusetts Institute of Technology (May 1977).

12. J. W. Bryson, B. R. Bass, and R. H. Bryan, "Determination of K-Factors for Surface Flaws in Cylinders Under Combined Pressure-Thermal Loading," *Heavy-Section Steel Technology Program Quart. Prog. Rep. October–December 1980*, NUREG/CR-1941 (ORNL/NUREG/TM-437), pp. 3–8.

13. J. G. Merkle et al., *Test of 6-in.-Thick Pressure Vessels. Series 4: Intermediate Test Vessels V-5 and V-9 with Inside Nozzle Corner Cracks*, ORNL/NUREG-7 (August 1977).

14. C. W. Smith, M. Jolles, and W. H. Peters, "Stress-Intensity Factors for Nozzle Cracks in Reactor Vessels," *Heavy-Section Steel Technology Prog. Quart. Prog. Rep. April–June 1976*, ORNL/NUREG/TM-49, pp. 10–18.

15. C. W. Smith and W. H. Peters, "Stress Intensities for Nozzle Cracks in Reactor Vessels," *Heavy-Section Steel Technology Program Quart. Prog. Rep. October–December 1976*, ORNL/NUREG/TM-94, p. 4.

## CONVERSION FACTORS[a]

| SI unit | English unit | Factor |
|---|---|---|
| mm | in. | 0.0393701 |
| cm | in. | 0.393701 |
| m | ft | 3.28084 |
| m/s | ft/s | 3.28084 |
| kN | $lb_f$ | 224.809 |
| kPa | psi | 0.145038 |
| MPa | ksi | 0.145038 |
| $MPa\cdot\sqrt{m}$ | ksi $\sqrt{in.}$ | 0.910048 |
| J | ft-lb | 0.737562 |
| K | °F or °R | 1.8 |
| $kJ/m^2$ | $in.-lb/in.^2$ | 5.71015 |
| $W\cdot m^{-2}\cdot K^{-1}$ | $Btu/hr-ft^2-°F$ | 0.176110 |
| kg | lb | 2.20462 |
| $kg/m^3$ | $lb/in.^3$ | $3.61273 \times 10^{-5}$ |
| mm/N | $in./lb_f$ | 0.175127 |
| T(°F) = 1.8 T(°C) + 32 | | |

[a] Multiply SI quantity by given factor to obtain English quantity.

NUREG/CR-2141/V1
ORNL/TM-7822
Dist. Category RF

## Internal Distribution

1. B. R. Bass
2. R. J. Berggren
3. S. E. Bolt
4-8. R. H. Bryan
9. J. W. Bryson
10. R. D. Cheverton
11. J. M. Corum
12. W. R. Corwin
13. J. R. Dougan
14. W. L. Greenstreet
15. R. C. Gwaltney
16. P. P. Holz
17. S. K. Iskander
18. K. K. Klindt
19. A. L. Lotts
20. J. G. Merkle
21. R. K. Nanstad
22. D. J. Naus
23. F. H. Neill
24. G. C. Robinson
25-26. T. W. Robinson, Jr.
27. G. M. Slaughter
28. W. J. Stelzman
29. H. E. Trammell
30-34. G. D. Whitman
35. Patent Office
36. Central Research Library
37. Document Reference Section
38-39. Laboratory Records Department
40. Laboratory Records (RC)

## External Distribution

41. C. Z. Serpan, Reactor Safety Research, Nuclear Regulatory Commission, Washington, DC 20555
42. M. Vagins, Reactor Safety Research, Nuclear Regulatory Commission, Washington, DC 20555
43. Office of Assistant Manager for Energy Research and Development, DOE, ORO, Oak Ridge, TN 37830
44-45. Technical Information Center, DOE, Oak Ridge, TN 37830
46-475. Given distribution as shown in category RF (NTIS — 10)

☆U.S. GOVERNMENT PRINTING OFFICE: 1981-740-062/109